UNIVERSITY OF CALIFORNIA SAN DIEGO

High-Throughput Computational Design of Interfacial Perpendicular Magnetic Anisotropy at Heusler/MgO Heterostructures

A dissertation submitted in partial satisfaction of the
requirements for the degree
Doctor of Philosophy

in

Materials Science and Engineering

by

Sicong Jiang

Committee in charge:

Professor Kesong Yang, Chair
Professor Prabhakar Bandaru
Professor Eric Fullerton
Professor Vitaliy Lomakin
Professor Jian Luo

2022

The dissertation of Sicong Jiang is approved, and it is acceptable in quality and form for publication on microfilm and electronically.

University of California San Diego

2022

DEDICATION

To my beloved parents and friends.

TABLE OF CONTENTS

LIST OF FIGURES

LIST OF TABLES

ACKNOWLEDGEMENTS

Firstly, I would like to express my gratitude to my advisor Dr. Kesong Yang, for his support during my research. Dr. Kesong Yang is full of knowledge and always willing to help his students. I greatly appreciate his patience to guide me how to do scientific research, including reading papers, designing calculations, and writing manuscripts. I enjoyed the discussion with him and learned a lot during the regular weekly 1:1 meeting. It is Dr. Kesong Yang that makes my project come true.

Secondly, I would like to thank my committee members, Professor Prabhakar Bandaru, Professor Eric Fullerton, Professor Vitaliy Lomakin, and Professor Jian Luo for their suggestions and support to my research.

Thirdly, I would like to express my sincere gratitude to Dr. Safdar Nazir who taught me hands-on theoretical calculations from scratch. I would like to thank Dr. Chongze Hu for his patience when I have technical issues of VASP software. I am also grateful to members in the Yang group, Dr. Jianli Cheng, Dr. Maziar Behtash, Dr. Paul H. Joo, Dr. Yuheng Li, Dr. Liyuan Wu, Joseph Wong, Jingning Zhang, Siyi Gao, Bowei Tang, and other people who helped me during my research.

Finally, I would like to express my gratitude to my parents Guiping Chen and Jianjun Jiang, without their understanding and support I could not be able to complete my PhD journey.

Chapter 1, in part, is a reprint of the material "Review of high-throughput computational design of Heusler alloys" as it appears in Journal of Alloys and Compounds, Sicong Jiang, Kesong Yang, 867, 158854, 2021. The dissertation author was the primary investigator and author of this paper.

Chapter 2, in full, is a reprint of the material "High-throughput design of interfacial perpendicular magnetic anisotropy at Heusler/MgO heterostructures" as it appears in ACS Applied Materials & Interfaces, Sicong Jiang, Safdar Nazir, Kesong Yang, 14, 9734-9743, 2022. The dissertation author was the primary investigator and author of this paper.

Chapter 3, in full, is a reprint of the material "Origin of the large interfacial perpendicular magnetic anisotropy in MgO/Co_2FeAl" as it appears in Physical Review B, Sicong Jiang, Safdar Nazir, Kesong Yang, 101, 134405, 2020. The dissertation author was the primary investigator and author of this paper.

Chapter 4, in full, is submitted for publication of the material "Accelerate the Discovery of Quaternary Heusler Materials for Perpendicular Magnetic Tunnel Junctions via High-throughput first-principle Calculations", Sicong Jiang, Kesong Yang. The dissertation author was the primary investigator and author of this paper.

Chapter 5, in part, is being prepared for submission for publication of the material "Evaluate disorder effects of the quaternary heusler compound via high-throughput *ab-initio* calculation", Sicong Jiang, Kesong Yang. The dissertation author was the primary investigator and author of this paper.

Chapter 6, in part, is a reprint of the material "Review of high-throughput computational design of Heusler alloys" as it appears in Journal of Alloys and Compounds, Sicong Jiang, Kesong Yang, 867, 158854, 2021. The dissertation author was the primary investigator and author of this paper.

VITA

2015	B. E. in Materials Science and Engineering, Zhengzhou University
2017	M. S. in Materials Science and Engineering, University of California San Diego
2022	Ph. D. in Materials Science and Engineering, University of California San Diego

PUBLICATIONS

Sicong Jiang, Safdar Nazir, Kesong Yang "Origin of the large interfacial perpendicular magnetic anisotropy in MgO/Co_2FeAl", *Physical Review B*, 101, 134405, 2020.

Sicong Jiang, Kesong Yang, "Review of high-throughput computational design of Heusler alloys", *Journal of Alloys and Compounds*, 867, 158854, 2021.

Sicong Jiang, Safdar Nazir, Kesong Yang, "High-throughput design of interfacial perpendicular magnetic anisotropy at Heusler/MgO heterostructures", *ACS Applied Materials & Interfaces*, 14, 9734-9743, 2022.

Sicong Jiang, Kesong Yang, "Accelerate the Discovery of Quaternary Heusler Materials for Perpendicular Magnetic Tunnel Junctions via High-throughput first-principle Calculations", submitted.

Sicong Jiang, Kesong Yang, "Evaluate disorder effects of the quaternary heusler compound via high-throughput *ab-initio* calculation", in preparation.

Safdar Nazir, **Sicong Jiang**, Jianli Cheng, Kesong Yang, "Enhanced interfacial perpendicular magnetic anisotropy in Fe/MgO heterostructure via interfacial engineering", *Applied Physics Letters*, 114, 072407, 2019.

Maziar Behtash, Joseph Wong, **Sicong Jiang**, Jian Luo, Kesong Yang, "First-principles study of impurity segregation in zirconia, hafnia, and yttria-stabilized-zirconia grain boundaries", *Journal of the European Ceramic Society*, 39, 3812-3820, 2019.

ABSTRACT OF THE DISSERTATION

High-Throughput Computational Design of Interfacial Perpendicular Magnetic Anisotropy at Heusler/MgO Heterostructures

by

Sicong Jiang

Doctor of Philosophy in Materials Science and Engineering

University of California San Diego, 2022

Professor Kesong Yang, Chair

The Heusler/MgO-based magnetic tunnel junctions (MTJs) with perpendicular magnetic anisotropy (PMA) have attracted extensive interest because of their potential utilization in spin-transfer-torque magnetic random-access memory (STT-MRAM) with long retention time and low switching current. As a large family of intermetallic compounds, Heusler alloys offer fascinating magnetic properties due to their wide variety of element compositions. Nevertheless, the selection of promising Heusler compounds candidates for the application of p-MTJs with high stability and low energy consumption becomes a grand challenge. In this dissertation, we provided a systematic high-throughput computational design of Heusler/MgO heterostructures to

search for promising structures with robust materials stability and large perpendicular magnetic anisotropy by employing a series of descriptors such as formation energy, convex hull distance, magnetic ordering, lattice misfit, magnetic anisotropy constant, interfacial cleavage energy, spin polarization, and tunnel magnetoresistance.

In the first project, we focused on the full Heusler (X_2YZ) and half Heusler (XYZ) compounds. By using a comprehensive screening over 40, 000 ternary Heusler compounds, 363 full Heusler compounds, and 134 half Heusler compounds were confirmed thermodynamically stable, where five full Heusler compounds and two half-Heusler compounds were found promising for designing p-MTJs.

In the second project, we studied the origin of the large interfacial PMA in the Co_2FeAl/MgO structure, by analyzing the layer-resolved and atomic-orbital-resolved K_i distributions. Later, the influences of the 26 capping layers on the Co_2FeAl/MgO structure were further investigated. Our calculations indicated that adding Fe- and W-capping layers can significantly increase the K_i of the system.

In the third project, we performed a systematic high-throughput screening in selecting the quaternary Heusler/MgO heterostructures. 7 out of 3094 stable quaternary Heusler compounds were found feasible for future applications in the p-MTJs. Their phase stability was further confirmed by using the swapping method.

In the fourth project, we proposed a swapping method to predict the disordering effects in the quaternary Heusler ($XX'YZ$) compounds. By using the swapping method, we successfully verified the ordered structure of CoFeCrGe, the $L2_1$ disordering in the CoMnCrAl, and the DO_3 disordering in the CoFeMnGe, demonstrating the efficiency of our method.

Chapter 1

Introduction

1.1 Background

To date, magnetic tunnel junctions (MTJs) with two ferromagnetic (FM) layers separated by a thin insulating barrier have attracted great interest because of their wide applications in the magnetic random-access memories (MRAMs) and other memory recording devices[1, 2, 3, 4, 5]. Compared to the traditional in-plane MTJs, perpendicular magnetic tunnel junctions (p-MTJs) tend to have higher thermal stability, lower switching current, and faster reversal speed[6, 7]. In general, the strength of the anisotropy in MTJs can be characterized by the magnetic anisotropy per unit area (K_i). For the p-MTJs, the large positive K_i is desired to overcome the demagnetization and maintain a sufficiently high thermal stability when the size of the building blocks decrease to the nanoscale[1, 8].

Many prior experimental and computational efforts have been made to explore material structures that can have perpendicular magnetic anisotropy (PMA). In 2010, Ikeda et al. successfully synthesized p-MTJ Ta/CoFeB/MgO/CoFeB/Ta with a large K_i of 1.3 mJ/m^2, high TMR ratio of 120 %, and a low switching current of about 49 μA at the same time[9]. Later, in the structure of Fe/MgO, both experimental and theoretical work have confirmed the $K_i > 1$ mJ/m^2

and, the PMA mainly attributes from the orbital hybridization between the interfacial Fe and O atoms[10, 11, 12, 13]. In addition, PMA were also reported in the Co_2FeAl/MgO structure with a K_i between $1.14-1.31$ mJ/m^2, where the value of K_i can be tuned by different transition metal capping layers[14, 15, 16]. Among all the materials structures that have been investigated, heterostructures with Heusler alloys as the FM layers have attracted great interest due to the potentially high spin polarization, low damping constant, and a curie temperature above room temperature[17, 18, 19, 20, 21, 22, 23].

Heusler compounds have been widely studied in the spintronic community since the first prediction of the half-metallic property in the half-Heusler alloy, NiMnSb, by de Groot *et al.* in 1983 [24]. The term is derived from the name of a German mining engineer and chemist Friedrich Heusler, who discovered the first Heusler compound, Cu_2MnAl [25, 26]. Heusler compounds exhibit extraordinary magnetic properties such as half-metallicity [27, 28, 29], ferromagnetism [30], antiferromagnetism [31], ferrimagnetism [32], giant anomalous hall effect [33], and superconductivity [34, 35] for potential spintronic applications. For example, Cu_2MnAl is formed by nonmagnetic metal elements but shows room-temperature ferromagnetism [25, 26].

As one of the largest families of ternary intermetallic compounds, Heusler alloys have a composition of X_2YZ (full Heusler) or XYZ (half Heusler), where X and Y are transition metals (TMs) and Z is the p-block main group element, forming a vast collection of more than 1500 compounds [36, 37]. Accordingly, Heusler compounds have a wide range of properties beyond above mentioned magnetic properties and have continuously attracted great attention for various technological applications such as energy conversion [38, 39, 40, 41, 42] and quantum computing as topological insulators [43, 44]. Moreover, by chemical substitutions and structural modifications [45]. Heusler compounds are being extended to binary (X_3Z) [46, 47, 48] and quaternary compounds ($XX'YZ$) [45, 49, 50, 51, 52, 53, 54, 55] towards enhanced properties and device functionalities. Therefore, Heusler compounds provide a large material space for a high-throughput design of target functional materials with desired properties because of the large

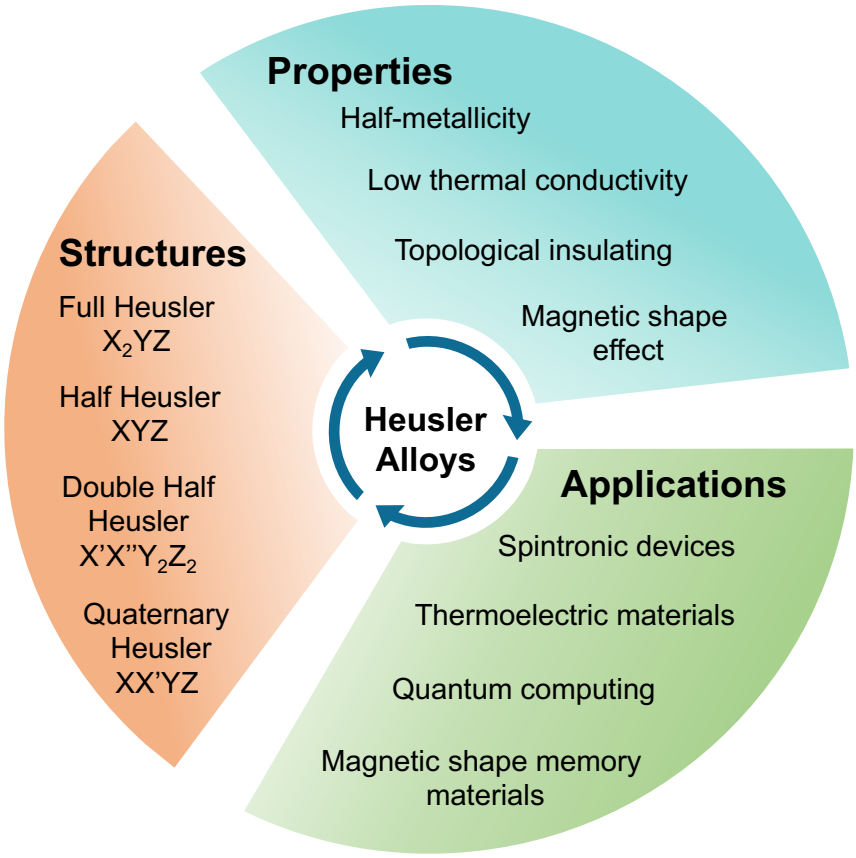

Figure 1.1: Overview of structures, properties, and applications of Heusler alloys.

materials space and tunable properties. An overview of the structures, properties, and applications of Heusler alloys is summarized in Figure 1.1.

1.2 Structure, Stability, and Slater-Pauling Rule

1.2.1 Crystal Structure

The full Heusler compounds X_2YZ can be classified into four types of structures, including the regular cubic, the regular tetragonal, the inverse cubic, and the inverse tetragonal, based on the relative positions of X and Y atoms and the type of crystal systems. Fig. 1.2 shows the conventional cells of the four types of structures. The regular cubic structure has a space group of

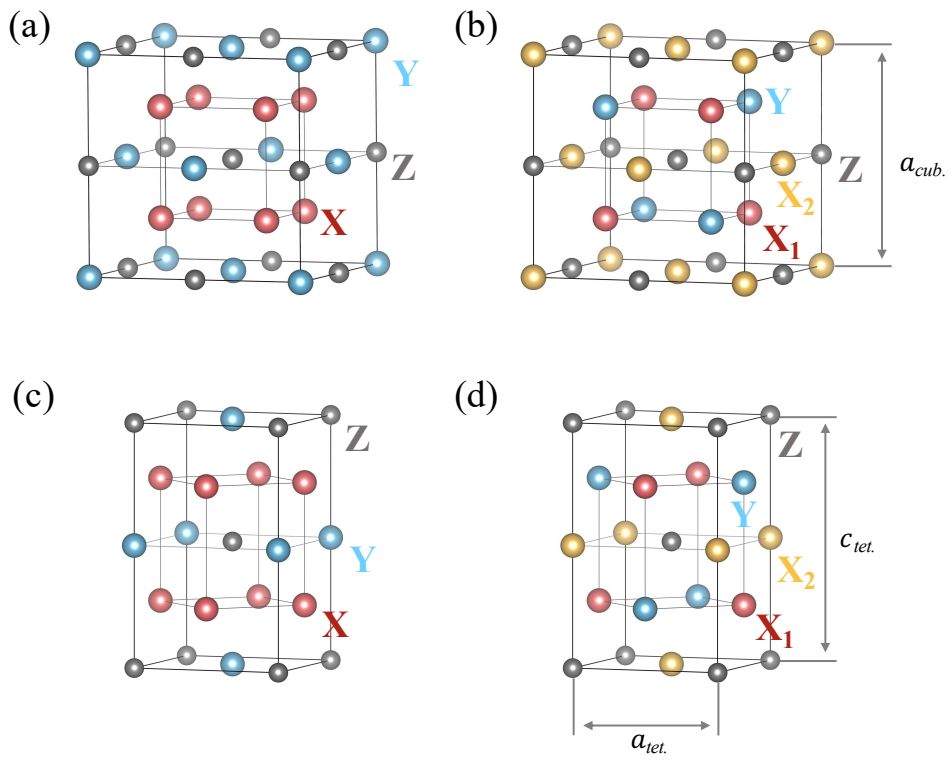

Figure 1.2: Schematic structure of (a) regular cubic, (b) inverse cubic, (c) regular tetragonal, and (d) inverse tetragonal full Heusler (X_2YZ) compounds.

$Fm\bar{3}m$ (no. 225), in which X atoms are at the Wyckoff position 8c (1/4, 1/4, 1/4) and Y and Z atoms occupy 4a (0, 0, 0) and 4b (1/2, 1/2, 1/2) positions, respectively, see Fig. 1.2a. The inverse cubic structure can be obtained by exchanging the positions between four X atoms and four Y atoms, leading to a space group of $F\bar{4}3m$ (no. 216), see Fig. 1.2b. In this structure, X atoms have two non-equivalent atomic environments and occupy the Wyckoff positions 4c (1/4, 1/4, 1/4) and 4a (0, 0, 0), respectively, and Y and Z atoms are at 4d (3/4, 3/4, 3/4) and 4b (1/2, 1/2, 1/2), respectively.

Regular and inverse tetragonal Heusler structures can be derived from the regular and the inverse cubic structures, respectively, by stretching or compressing the cubic structures along the z-axis [56], thus lowering the crystal symmetry. The regular tetragonal structure has a space group of $I4/mmm$ (no. 139), in which X atoms occupy the Wyckoff positions 4d (0, 1/2, 1/4),

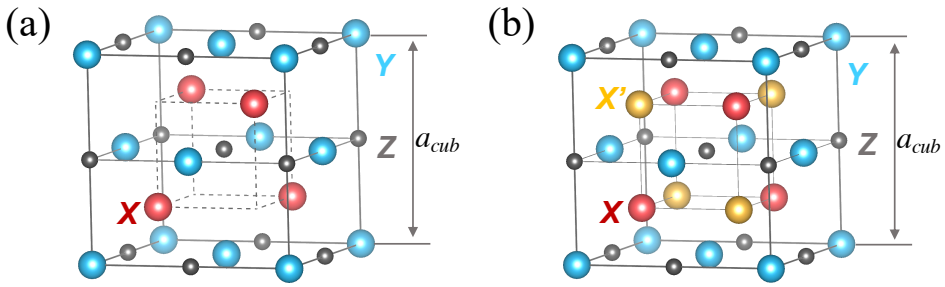

Figure 1.3: Schematic structure of (a) half Heusler (XYZ), (b) quaternary Heusler ($XX'YZ$) compounds.

and Y and Z atoms occupy 2b (0, 0, 1/2) and 2a (0, 0, 0) positions, respectively, as shown in Fig. 1.2c. The inverse tetragonal structure has a space group of $I\bar{4}m2$ (no. 119), in which the two non-equivalent X atoms occupy the Wyckoff positions 2b (0, 0, 1/2) and 2c (0, 1/2, 1/4), respectively, and Y and Z atoms occupy 2d (0, 1/2, 3/4) and 2a (0, 0, 0) positions, respectively, see Fig. 1.2d. Note that the tetragonal unit cell can also be viewed as one inner half unit cell of the modified cubic structure upon a rotation by 45°along the z axis plus the stretch (or compression) along the z axis to make $c : a \neq \sqrt{2}$:1, see Fig. 1.2. Consequently, the number of the atoms in the tetragonal unit cells is half of that in the cubic unit cells.

Half Heusler (XYZ) can be viewed as the full Heusler (X_2YZ) upon removing half the number of X atoms, see Fig. 1.3a. Half Heusler structure has a space group of $F\bar{4}3m$ (no. 216), where an X atom occupies the Wyckoff position 4c (1/4, 1/4, 1/4), and Y and Z atoms occupy 4a (0, 0, 0) and 4b (1/2, 1/2, 1/2) positions, respectively. Similarly, the quaternary Heusler ($XX'YZ$) can be viewed as the full Heusler (X_2YZ) in which half number of X atoms are substituted by X' atoms, as shown in Fig. 1.3b. Quaternary Heusler has a space group of $F\bar{4}3m$ (no. 216), in which X and X' atoms occupy the Wyckoff positions 4c (1/4, 1/4, 1/4) and 4d (3/4, 3/4, 3/4), respectively, and Y and Z atoms are at 4a (0, 0, 0) and 4b (1/2, 1/2, 1/2), respectively.

1.2.2 Stability

One critical step in the high-throughput materials design is the evaluation of material stability, particularly for the virtual compounds. Several common methods used to evaluate the material stability are discussed below:

Formation Energy

By taking full Heusler (X_2YZ) as an example, its formation energy is defined as: ΔE_f = E_{X_2YZ} - ($2E_X$ + E_Y + H_Z), where E_{X_2YZ} is the total energy of the compound X_2YZ, and E_X (E_Y and E_Z) is the ground state energy of the bulk X (Y and Z) in its elemental phase. Note that the item ΔE_f is also called solid-state formation enthalpy. A negative value of ΔE_f indicates that the compound is stable against its constituent elements at 0 K. This is a necessary but not sufficient condition for the thermodynamic stability of X_2YZ compound because it does not guarantee the stability of the compound against other competing phase or mixture of phases. Since the calculations of ΔE_f is relatively cheap and fast, search for Heusler compounds with a negative ΔE_f from a large number of compounds is usually the first step in the high-throughput materials design.

Convex Hull Calculation

A convex hull construction of formation energies can be used to identify thermodynamically stable compounds with respect to decomposition into other phases when without considering kinetic effects [57]. The convex hull is a set of lines (or surfaces for $\geq$ 3 degrees of freedoms) of formation energies versus compositions that connect all the lowest energy phases. In principle, all the competing phases should be considered to include the lowest energy phases. Therefore, the formation energy (enthalpy) calculation mentioned above only reflects one possible decomposition path (into elementary phases) in the convex hull calculations, and thus convex hull calculations are better in evaluating the thermodynamic stability of materials.

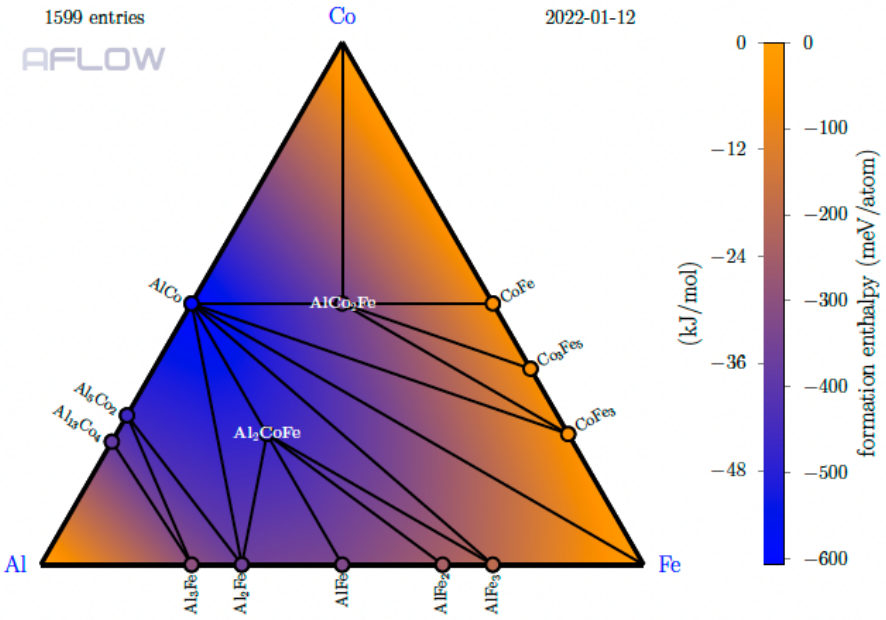

Figure 1.4: A ternary convex hull diagram of Al-Co-Fe. $AlCo_2Fe$ and Al_2CoFe are the most stable ternary compounds.

The convex hull distance (ΔE_H) for a phase can be calculated as: $\Delta E_H = E_f$ - H_{hull}, where E_f is the formation energy of the phase and H_{hull} is the convex hull energy at the composition of the phase [58]. Accordingly, every phase on the convex hull ($\Delta E_H = 0$) is thermodynamically stable because it has a formation energy lower than any other phases or the linear combination of phases at its composition [59]; while the phase with a large ΔE_H is more likely to decompose into other competing phases and thus is thermodynamically unstable. In other words, ΔE_H measures the phase stability of a certain phase. Phases with $\Delta E_H = 0$ are a part of the convex hall and are the most stable against decomposition, while phases with $\Delta E_H > 0$ but less than some threshold value are potentially stable (metastable) [60]. To identify potentially stable phases, the threshold of ΔE_H can be set as high as 100 meV/atom [53], depending on the accuracy and tolerance of the high-throughput *ab-initio* calculations. However, a more strict criterion around 30-50 meV/atom was also commonly used [61, 62]. It is worth mentioning that one can conveniently calculate the convex hull distance and plot the convex hull diagram against the competing phases for the

inorganic binary and ternary compounds using the AFLOW-CHULL tool[58]. Figure 1.4 shows a sample convex hull diagram of Al-Co-Fe, where Al_2CoFe and $AlCo_2Fe$ are the most stable ternary compounds.

Phonon Calculations

First-principles phonon calculations can be used to determine the dynamic (mechanical) stability of crystalline materials [63]. A crystalline material is dynamically (mechanically) stable at an equilibrium state if its potential energy always increases against any combinations of atomic displacements. This means that all the phonons have real and positive frequencies. On the contrary, the crystal is dynamically unstable if the phonons have an imaginary (or negative) frequency, which means that appropriate atomic displacements will reduce the potential energy of the system. Hence, phonon calculations often serve as one effective approach to evaluate the dynamical (mechanical) stability of materials including Heusler alloys [64, 65, 66].

1.2.3 Slater–Pauling Rule

The Slater-Pauling rule connects the magnetic moment (M_t) and the number of valence electrons (N_v) per unit formula for half-metallic Heusler alloys [36, 67, 68]. It was reported by Slater [69] and Pauling [70] that the magnetic moments (m) of $3d$ elements and their binary compounds are related to the mean number of valence electrons (n) per atom. The spin moment per atom is given by $m = n\uparrow - n\downarrow$, and the total valence electrons (d electrons) is $n = n\uparrow + n\downarrow$. In the case of a half-metallic system with localized moments, in which the Fermi level is pinned in the energy gap of the minority density of states, $n\downarrow$ is approximately 3, as indicated by the Slater-Pauling rule. Therefore, this leads to $m = n - 6$ for one atom. In the case of half-metallic half Heusler (XYZ), there are three atoms per unit formula and thus the Slater-Pauling rule gives $M_t = N_v$ - 18.[36, 67] In the case of half-metallic full Heusler (X_2YZ) and quaternary Heusler, there are four atoms per unit formula, and the Slater-Pauling rule leads to $M_t = N_v$ - 24.[36, 67] In

short, the Slater-Pauling rule serves as one powerful tool for searching for half-metallic Heusler compounds.

1.3 High-throughput Design of Heusler alloys

As an emerging field in materials science, high-throughput computational materials design has attracted great attention due to its high efficiency in the accelerated discovery of target materials with desired properties [71, 72, 73, 61]. Although there is no strict definition of the "high-throughput calculations", generally speaking, hundreds, thousands, or tens of thousands of compounds (structures) need to be calculated for achieving a high-throughput materials design [74]. In doing so, these calculations can generate a materials repository, and then the target materials with the desired properties can be screened across the materials repository.

1.3.1 Full Heusler

In 2017, Sanvito *et al.* reported a high-throughput computational discovery of novel ferromagnetic Heusler alloys [62]. In this study, the authors first built an extensive electronic structure library that contains 236,115 compounds using high-throughput first-principles electronic structure calculations, and then by employing a group of combinatorial materials descriptors, including formation enthalpy, thermodynamic stability, and magnetic moment, and finally discovered 20 novel ferromagnetic materials belonging to Co_2YZ, Mn_2YZ, and X_2MnZ classes. In 2017, Balluff *et al.* reported a prediction of 21 antiferromagnetic Heusler compounds with Néel temperature above room temperature by screening materials database AFLOWLIB using a combinatorial high-throughput approach based on density functional theory calculations [60]. In 2012, the possibility of Mn_{3-x}-based tetragonal Heusler compounds was realized by Winterlik *et al.* in both experiments and theoretical calculations [75]. These tetragonal compounds offer more opportunities to tune the STT parameters, such as switching current and thermal stability. Later, the

origin of the tetragonal ground state of Heusler compounds X_2YZ was explored via first-principles density functional theory (DFT) calculations in 2017 by Faleev *et al.* [56]. They explained the tetragonal distortion from the peak-and-valley character of the density of states (DOS) of Heusler compounds in their cubic phases along with the smooth shift of peaky DOS structure relative to the Fermi energy when valence electrons are added to the system. Soon after, by continuing their previous computational studies of the 286 Heusler compounds [56], Faleev *et al.* demonstrated a recipe for searching for tetragonal Heusler compounds for high-density memory applications via studying the perpendicular magnetic anisotropy (PMA) and the tunnel magnetoresistance (TMR) [76]. 19 out of 116 compounds were identified as the potential candidates for spin-transfer torque magnetic random-access memory (STT-MRAM) magnetic tunnel junction (MTJ) devices by employing screening conditions: $K_v > 0.9$ MJ/m^3, $|E_z| > 0.15$ eV, and $|P_f| > 0.7$. As one important subfamily of Heusler compounds, inverse Heusler compounds have attracted attentions recently because of their half-metallic properties. In 2018, Ma *et al.* conducted a large-scale first-principles computational study for 405 inverse Heusler compounds X_2YZ (X = Sc, Ti, V, Cr, Mn, Fe, Co, Ni, and Cu; Y =Ti, V, Cr, Mn, Fe, Co, Ni, Cu, and Zn; and Z =Al, Ga, In, Si, Ge, Sn, P, As, and Sb) to identify promising materials for spintronics [77]. By using negative formation energy as the screening criterion along with the electronic structure analysis, the authors identified 14 semiconductors, 51 half-metals, and 50 near half-metals from all the 405 compounds. In addition to the spintronic applications, full Heusler compounds are also one class of promising thermoelectric materials [78, 79, 80]. In 2016, He *et al.* reported a computational discovery of a new class of stable semiconducting full Heusler compounds with ten valence electrons via a high-throughput *ab-initio* screening, from which 15 full Heusler X_2YZ compounds (X = Ca, Sr, and Ba; Y = Au and Hg; Z = Sn, Pb, As, Sb, and Bi) with high power factors and extremely low lattice thermal conductivity were identified [81]. In 2016, Oliynyk *et al.* demonstrated a high-throughput discovery of full-Heusler compounds based on the machine learning approach [82]. By employing the machine learning model, over 780 out of 400,000 candidates were

predicted to be Heusler alloys with a probability larger than 0.9. In particular, 12 novel gallides MRu_2Ga and RuM_2Ga (M = Ti-Co) were predicted as Heusler compounds and were further experimentally confirmed from X-ray diffraction.

1.3.2 Half Heusler

As one large family of materials with diverse physical properties, half Heusler compounds have also received increasing attention in the aspect of high-throughput materials design because of their potential technological applications. In 2014, Carrete *et al.* pioneered the high-throughput computational design of low-thermal-conductivity half-Heusler semiconductors as thermoelectric materials [42]. Later, on the basis of the previously identified 75 thermodynamically stable compounds [42], Guo *et al.* reported 9 *p*-type and 6 *n*-type promising candidate thermoelectric materials by analyzing their electrical properties and found that the electrical properties play a major role in the thermoelectric performance in the half-Heusler compounds [83]. It was thus proposed that the band engineering and defect engineering could be used for the further optimization of the power factors and the reduction of the thermal conductivity. In 2017, Ma *et al.* presented a comprehensive computational study on the structural stability, electronic, and magnetic properties of 378 *XYZ* half Heusler compounds (X = Cr, Mn, Fe, Co, Ni, Ru, and Rh; Y = Ti, V, Cr, Mn, Fe, and Ni; Z = Al, Ga, In, Si, Ge, Sn, P, As, and Sb) using large-scale first-principles DFT calculations [59]. Several trends were found in their investigations: i) ΔE_f decreases with the atomic number of the Y element decreases; ii) the transition metal with larger atomic number prefers to occupy X site; iii) the presence of a gap at the Fermi level in one or both spin channels enhances the stability. In 2019, Sahni *et al.* screened a total number of 192 I-III-IV class of half Heusler alloys with 8 valence electrons using large-scale *ab initio* computational study for potential functional applications [64]. Among the 21 semiconducting compounds the authors identified, 6 were found to have excellent thermoelectric properties and 17 show robust topological insulating properties from the computational characterization of the

bulk band inversion and surface conducting states.

1.3.3 Quaternary Heusler

In 2018, He *et al.* reported a new family of stable semiconducting quaternary Heusler compounds based on the 18-electron rule via high-throughput *ab initio* calculations [84]. The discovered quaternary Heusler semiconductors have band gaps in the range of 0.3-2.5 eV and exhibit unusual properties for potential photovoltaic and thermoelectric applications. In 2019, Gao *et al.* performed a high-throughput screening for spin-gapless semiconductors (SGSs) based on quaternary Heusler alloys *XX'YZ* (*X*, *X'*, and *Y* are transition metal elements, and *Z* is one main group element) based on DFT calculations [53]. The SGSs refers to one class of half metals whose majority spin channel is semi-metallic while whose minority spin channel is insulating. After systematically studied thermodynamic, mechanical, and dynamical stabilities of this sub-list of compounds, the authors identified 70 hitherto unreported SGSs, among which 17 candidates have a convex hull distance within 100 meV/atom, which are likely to be synthesized experimentally. The machine learning approach was also used for the screening of quaternary Heusler compounds. For example, in 2018, Kim *et al.* reported 55 previously unknown quaternary Heusler compounds ($XX'YZ$) that were discovered from a machine-learning-assisted high-throughput materials screening approach [54]. Their work shows that a large and diverse training set yields the most accurate predictions in machine learning, and a combination of machine learning and DFT calculations can remarkably increase the speed to find new stable materials beyond the quaternary Heusler compounds.

1.4 Summary

In this thesis, we presented a systematical high-throughput screening of Heusler compounds to search for feasible materials interfaces with MgO as substrate for the application of

p-MTJs with desired properties and understanding the origin of the PMA. In chapter 2, we demonstrated the efficiency of the high-throughput approach to screen for the stable ternary Heusler compounds, where five full Heusler compounds, including Co_2CrAl, Co_2FeAl, Co_2HfSn, Fe_2IrGa, Mn_2IrGe, and two half-Heusler compounds PtCrSb and PtMnAs were found promising for designing p-MTJs. In chapter 3, we mainly investigated the origin of PMA in the Co_2FeAl/MgO heterostructure and the influences of the 26 capping layers. In chapter 4, we further extended our high-throughput screening to the quaternary Heusler compounds, where 7 quaternary Heusler compounds, including AlTiOsMn, IrCrAlTi, IrCrGaTi, IrMnZnTi, OsCrAlTa, OsCrAlTa, OsCrAlV, and TaGaOsCr, were found feasible for future applications in the p-MTJs. In chapter 5, we proposed a swapping method that can predict the disordering in the quaternary Heusler compounds. Finally, in chapter 6, we provided an outlook on the possible future directions.

1.5 Acknowledgement

Chapter 1, in part, is a reprint of the material "Review of high-throughput computational design of Heusler alloys" as it appears in Journal of Alloys and Compounds, Sicong Jiang, Kesong Yang, 867, 158854, 2021. The dissertation author was the primary investigator and author of this paper.

Chapter 2

High-Throughput Design of Interfacial Perpendicular Magnetic Anisotropy at Heusler/MgO Heterostructures

In chapter 1, we provided an overview of the Heusler compounds and the high-throughput computational design. As a large family of intermetallic compounds, Heusler compounds have fascinating materials properties. However, it is challenging to select appropriate combinations of Heusler ferromagnets and insulators with the desired interfacial properties. In this chapter, we report a systematic high-throughput screening approach to search for candidate Heusler/MgO material interfaces with strong PMA and other desired material properties for spintronic technologies. Based on the open quantum material repositories, we have developed a series of material descriptors, including formation energy, convex hull distance, magnetic ordering, lattice misfit, magnetic anisotropy constant, and tunnel magnetoresistance, to filter candidate Heusler/MgO interfaces among the possible 40,000 ternary Heusler compounds. This work demonstrates a new way for the high-throughput design of functional material interfaces for spintronic applications via exploiting the open quantum material repositories and developing effective material descriptors,

along with the large-scale *ab-initio* calculations for material interfaces.

2.1 Introduction

Magnetic tunnel junctions (MTJs) that consist of two ferromagnets separated by an insulating barrier are the most important building blocks in the spintronic technologies. They are not only widely used in the memory recording devices such as magnetoresistive random-access memory (MRAM)[4, 1, 5] but also show promising applications in next-generation advanced spintronic computing technologies such as ultra-fast in-memory computing and quantum computing.[85, 86] Despite their wide usage, the in-plane magnetization based MTJs still face grand challenges in the high-density and low-power consumption devices. In contrast, MTJs with interfacial perpendicular magnetic anisotropy (PMA) offer solutions to these challenges because perpendicular MTJs (p-MTJs) require smaller switching currents and have faster reversal speed for magnetization switching than in-plane MTJs.[87, 88] The strength of the interfacial magnetic anisotropy is generally characterized by the anisotropy energy density, *i.e.*, magnetic anisotropy constant (K_i) in the units of energy per unit area. A large K_i is often needed to overcome the shape anisotropy to achieve high thermal stability in memory cells for ensuring long data retention time of nonvolatile magnetic memories, particularly for nanoscale devices.[89, 90, 91] For example, a recent theoretical calculation suggests that a K_i of 4.7 mJ/m^2 is required for a data retention time of ten years as device sizes scale down to 10 nm.[8]

Magnetic anisotropy has been discovered for more than 60 years and usually occurs in materials that have strong spin-orbit coupling (SOC) interactions,[92, 1] such as Co/Pt, Co/Pd, and Co/Au interfaces, their K_i is typically less than 1 mJ/m^2.[93, 94] It has also been found in ferromagnetic films with weak SOC such as Co.[95] Interestingly, PMA has been recently observed at magnetic metal/oxide interfaces without strong SOC interactions, such as Co(Fe)/MO_x (M =Al, Mg, Ta, Hf, etc.),[96, 97, 98, 99] which offer great opportunities for developing new-generation p-

MTJs. One large breakthrough is the fabrication of p-MTJs based on the CoFeB/MgO interface,[9] in which a large K_i of 1.3 mJ/m^2 was discovered. In addition, other materials properties such as high spin polarization, large Tunnel magnetoresistance (TMR), and robust thermodynamic stability of material interfaces are also desired for high-performance spintronic applications. Therefore, to obtain desired interfacial properties, in addition to further optimizing the interfacial magnetic properties of the prototype CoFeB/MgO system, another avenue is to search for new ferromagnetic/insulator material interfaces.[100, 101] For example, research efforts have been made to explore the interfacial magnetic anisotropy properties at several new ferromagnetic/insulator materials interfaces, such as Co_2FeAl/MgO,[14, 102] Mn_3Ga/MgO, [91] MgO/Co(111),[103, 104] Fe/$MgAl_2O_4$,[105] Co_2FeAl/$NiFe_2O_4$,[106] and Fe/$CuInSe_2$.[107]

Heusler alloys serve as one promising ferromagnetic layer in the MgO-based p-MTJs because of their extraordinary magnetic properties.[17, 18, 19, 20, 21, 22, 23, 16] Moreover, Heusler alloys represent a large family of ternary compounds with formula X_2YZ, in which X and Y are often transition metals and Z is a main-group element.[108, 109] Therefore, Heusler compounds exhibit a wide range of properties and extensive tunability through composition modifications, and thus provide great opportunities for searching for new ferromagnetic/insulator material interfaces with target material properties. In particular, it is noted that, in addition to the traditional bulk compounds, two-dimensional materials are emerging as one class of promising materials for spintronic applications due to their fascinating properties.[110, 111, 112]

In this work, we presented a systematic high-throughput screening approach to select candidate Heusler/MgO material interfaces with desired properties on the basis of the open quantum materials repositories and large-scale *ab-initio* electronic structure calculations. By employing a series of effective material descriptors, five full Heusler compounds and two half-Heusler compounds, were found promising for high-performance p-MTJs. In particular, the prototype Co_2FeAl[101, 14, 102] was found after the comprehensive screening, thus showing the rationality of our approach. This work demonstrates a new approach to search for target functional materials

interfaces for spintronic applications via exploiting the open quantum materials repositories in a high-throughput fashion and this approach can be extended to other types of material interfaces beyond the ternary Heusler compounds.

2.2 Computational and Structural Details

The high-throughput density functional theory (DFT) calculations were carried out for bulk Heusler alloys using the Vienna *Ab-initio* Simulation Package (VASP) based the automatic material discovery framework AFLOW.[113] The projector augmented wave (PAW) pseudopotentials were used for treating electron-ion interactions,[114] and the generalized gradient approximation (GGA) parameterized by Perdew-Burke-Ernzerhof (PBE) was employed for exchange-correction functional.[115] All the bulk structures were fully relaxed with a convergence tolerance of 10^{-5} eV/atom and the k-points grid of a separation of 0.05 Å^{-1}. A much denser k-points grid with separation of 0.04 Å^{-1} was automatically set for all static calculations. Cutoff energy and other related computational settings were generated by AFLOW code automatically for both structural relaxations and static calculations.[113] In the heterostructure calculations, Γ-centered k-points grids were set to $8 \times 8 \times 1$ for ionic relaxation and $13 \times 13 \times 1$ for static calculation. All the atomic positions and lattice parameters were fully relaxed until the residual forces were smaller than 0.005 eV/Å. A convergence threshold of 10^{-6} eV was used for the electronic self-consistency loop including spin-orbit coupling (SOC) calculations.

To study the interfacial magnetic anisotropy, Heusler/MgO heterostructure models were employed. The in-plane lattice constant of the Heusler/MgO compound heterostructure model was fixed to the lattice constant of MgO. The calculated lattice constant of bulk MgO is 4.215 Å, close to the experimental value, 4.211 Å.[116] A 45° rotation along the [001] direction of conventional cubic bulk Heusler compound was made to match the lattice parameter of MgO substrate. Two types of symmetric interfaces, MgO/X_2 and MgO/YZ, were built. To resemble

the experimental setup of the MgO-based MTJs in which the MgO film thickness is around 1 nm[9], MgO substrate was set as seven layers ($\sim$ 1.2 nm) in our model. This is comparable with the previous computational studies in which five layers of MgO substrate was shown enough to calculate the magnetic anisotropy.[16] The magnetic anisotropy constant K_i was calculated by $(E_{[100]} - E_{[001]})/(2A)$, where $E_{[100]}$ and $E_{[001]}$ represent total energy with magnetization along [100] and [001] direction in a fully self-consistent-field manner, respectively, the factor of 2 in the denominator represents two symmetrical interfaces in the heterostructure model and A is the in-plane area.

2.3 Results and Discussion

2.3.1 Bulk Calculations

As the first step, we carried out high-throughput *ab-initio* electronic structure calculations for the selected bulk Heusler compounds based on the open quantum material repository[117] and previous studies.[62, 56] using the AFLOW code. All the four types of full Heusler X_2YZ compounds,[109] including regular cubic (reg. cub.), inverse cubic (inv. cub.), regular tetragonal (reg. tet.), and inverse tetragonal (inv. tet.) structures, shown in Figure 2.1, and half Heusler structures were considered.

First, we extracted the elemental combinations for the 248 novel full Heusler compounds that were identified as thermodynamically stable in the previous high-throughput screening of magnets based on the online materials repository Aflowlib.org that collect around 40,000 ternary Heusler compounds.[62, 117] These 248 compounds all belong to cubic full Heusler structures but their relatively stability against tetragonal structures were not systematically examined. As discussed later, some of these compounds have a ground-state tetragonal structure. Accordingly, all the four types of full Heusler structures for the 248 elemental combinations were considered in our calculations.

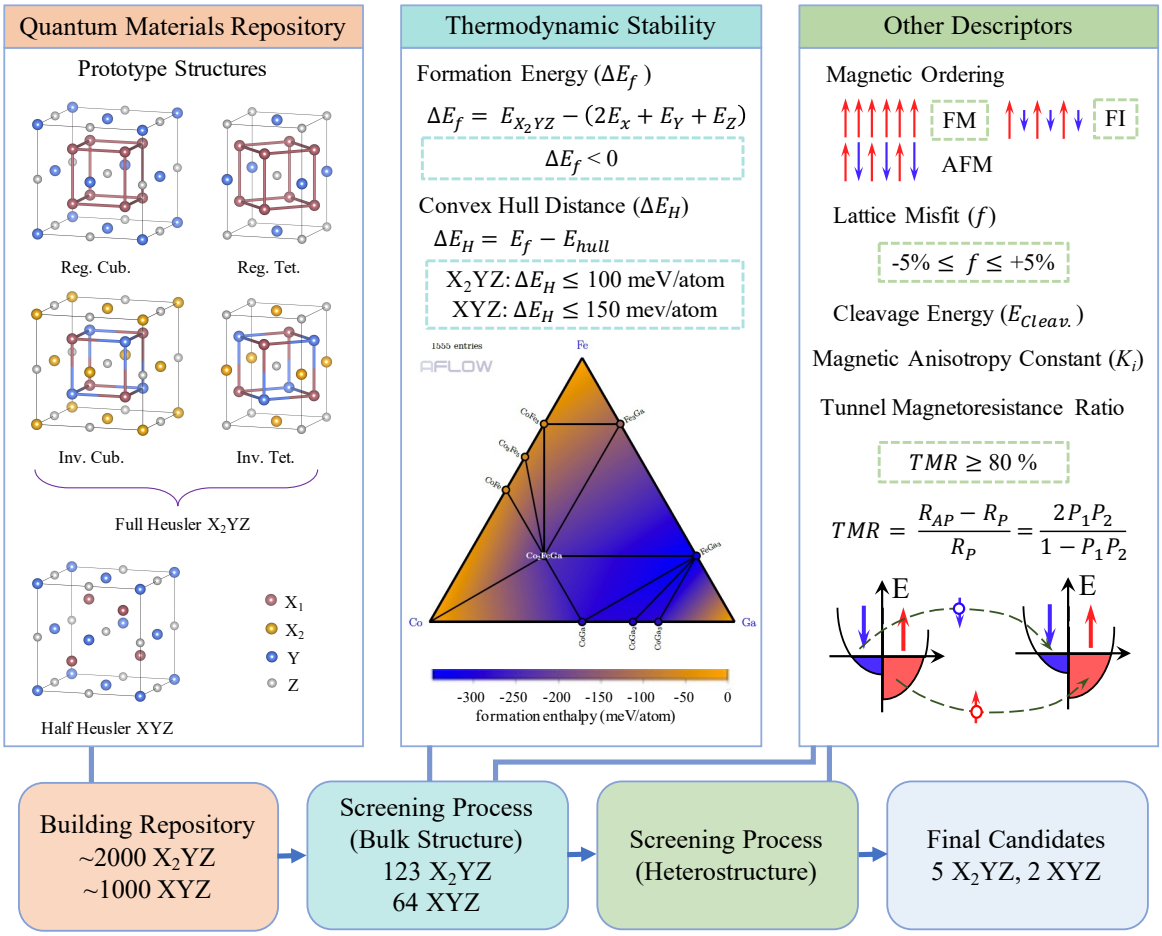

Figure 2.1: Schematic workflow of high-throughput screening of Heusler compounds with target interfacial properties for p-MTJs. The developed material descriptors include formation energy (ΔE_f), convex hull distance (ΔE_H), lattice mismatch (f) with MgO, interfacial cleavage energy ($E_{cleav.}$), magnetic anisotropy constant (K_i), and tunnel magnetoresistance ratio (TMR).

Second, we noted that, in another computational study, the relative stability of the four types of full Heusler structures for a total number of rare-earth-free 286 elemental compositions that are most likely to form high-temperature magnets were studied,[56] which include some new compounds that were not reported in Ref.[62] However, the thermodynamic stability of these compounds has not been fully evaluated from convex hull calculations.

Third, we identified the elemental combinations from the experimental Heusler compounds based on the data provided in Ref.[62] In short, we constructed our input full Heusler structures by considering all the above mentioned elemental combinations, which yields 561 unique elemental combinations and the resulting 2244 structures (561 $\times$ 4) for large-scale *ab-initio* calculations.

Last, we collected all the possible magnetic half-Heusler compounds by querying the AFLOWLIB database via a RESTful API[118, 119] with the following filters: space group (216), number of atoms (n_{atoms} = 3), number of species ($n_{species}$ = 3), formation energy ($\Delta E_f < 0$), and spin moment ($m > 0.2$ μB/f.u.). The compounds that contain nonmetal elements such as F, Cl, Br, I, Be, and P were excluded to narrow down the candidate compounds. This leads to a total number of 1235 half Heusler compounds.

2.3.2 Screening Bulk Materials

The second step is to screen promising bulk candidates from the 3,479 Heusler compounds. First, we selected a short list of thermodynamically stable compounds using two descriptors including formation energy and convex hull distance. Second, we employed another two descriptors including the ferromagnetic ordering and lattice misfit with MgO substrate to further narrow down the candidate list. These two descriptors were developed based on the requirements of p-MTJs for spintronic applications such as STT-MRAM devices. The workflow of the high-throughput screening procedure is shown in Figure 2.1, and the four screening descriptors are detailed as below:

(i) **Formation energy** (ΔE_f): A negative ΔE_f is a necessary condition for the thermodynamic stability of compounds. By taking the full Heusler X_2YZ as one example, it can be defined as $\Delta E_f = E_{X_2YZ}$ - ($2E_X + E_Y + E_Z$), where E_{X_2YZ}, E_X, E_Y and E_Z are the total energy for the compound X_2YZ and for the bulk X, Y, and Z single element ground-state phase, respectively. By using the criterion $\Delta E_f < 0$, we generated a short list of 1,682 candidate compounds, including 447 full Heusler and 1235 half Heusler.

(ii) **Convex hull distance** (ΔE_H): ΔE_H can be defined as $\Delta E_H = \Delta E_f$ - E_{hull}, where ΔE_f and E_{hull} are the formation energy of the compound and convex hull energy.[58] It represents the stability of the compound against the decomposition into all other competing phases, including the binary and ternary phases with the same element combinations. Hence, ΔE_H serves as one important supplementary tool in the evaluation of the thermodynamic stability. $\Delta E_H = 0$ means that the compound is thermodynamically stable and a small ΔE_H indicates the compound is potentially stable because of the entropy effects.

We calculated ΔE_H for all the 1,682 candidate compounds using the AFLOW-CHULL tool.[58] A summary of the bulk energetic properties was shown in Figure 2.2. Figure 2.2a and 2.2c show the distribution of ΔE_f versus ΔE_H for the full Heusler and half Heusler compounds, respectively. The pink square and blue circle represent experimentally verified and hypothetical compounds, respectively, where these data are collected from AFLOWLIB.[117] It shows that most of the experimentally synthesized full Heusler compounds have a $\Delta E_H < 100$ meV/atom while that of the half Heusler compounds have a $\Delta E_H < 150$ meV/atom. This implies a larger entropy in the half Heusler compounds than that in the full Heusler compounds. A comparable value of ΔE_H was also used to select thermodynamically stable Heusler alloys in previous computational studies.[59, 53] Hence, in our screening process, we set the thresholds of ΔE_H as 100 meV/atom for full Heusler X_2YZ and 150 meV/atom for half Heusler XYZ, where the compounds with a ΔE_H below the thresholds are considered thermodynamically stable. It is worth mentioning that the ΔE_H of the experimentally synthesized compound,[120, 121] PtMnGa

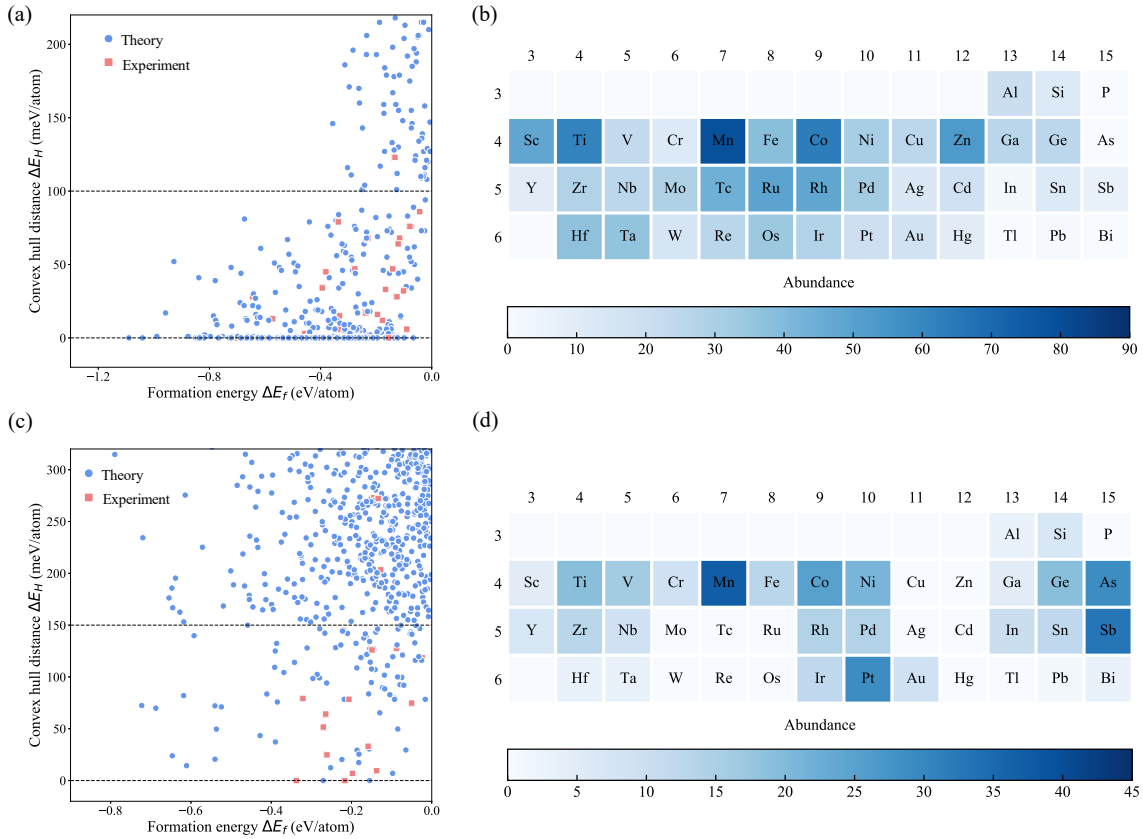

Figure 2.2: Illustration of energetic properties of (a-b) full Heusler and (c-d) half Heusler compounds. The left panel shows the distribution of formation energy (ΔE_f) versus convex hull distance (ΔE_H), in which the pink squares and blue circles represent the experimentally synthesized and theoretical compounds, respectively. The horizontal dash lines indicate the thresholds of ΔE_H at 100 and 150 meV/atom for full Heusler and half Heusler compounds, respectively. The right panel shows the heat map of element frequency of thermodynamically stable (b) full Heusler and (d) half Heusler compounds.

(labeled as GaMnPt based on the formula definition in this work), is as large as 270 meV, see Figure 2.2c. A close examination of the literature reveals that the synthesized compound PtMnGa has a hexagonal lattice with a space group of $P6_3/mmc$ (no. 194) rather than a cubic lattice.[121] This explains why its cubic half-Heusler structure has a large ΔE_H, implying that its cubic lattice is less likely to be synthesized.

In this step, we significantly narrowed down the number of the candidate full Heusler compounds to 363 and that of the half Heusler compounds to 134. This indicates that many compounds with $\Delta E_f < 0$ but large ΔE_H cannot be experimentally synthesized, showing that

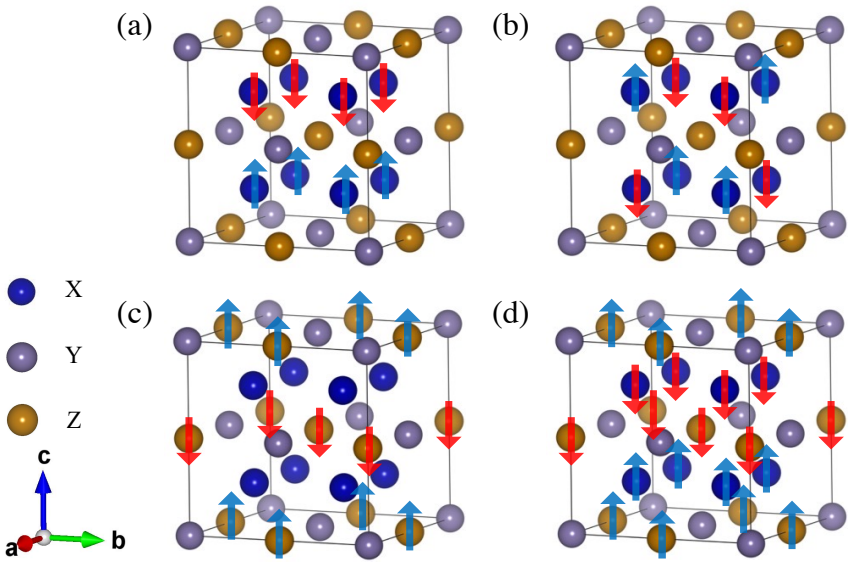

Figure 2.3: Schematic antiferromagnetic configurations of reg. cub. Heusler compounds for the case (a,b) if X atom is magnetic, (c) if Z atom is magnetic, and (d) if both X and Z atoms are magnetic.

$\Delta E_f < 0$ is not a sufficient condition for the thermodynamic stability. All the thermodynamically stable full Heusler and half Heusler compounds are listed in Table A.1 and A.2 of the appendix, respectively. The heat maps of element frequency for the 363 full Heusler and 134 half Heusler compounds were plotted in Figure 2.2b and 2.2d, respectively. Interestingly, Mn element shows the highest frequency in both stable half Heusler and stable full Heusler compounds. This can be attributed to the d^5 electron configuration of Mn ions that leads to high stability because d^5 configuration has more symmetry and exchange energy.

(iii) **Magnetic structure**: To screen ferromagnetic (FM) Heusler compounds, we next studied the magnetic structure of all the screened stable Heusler compounds by considering their FM configuration, possible antiferromagnetic (AFM) configurations, as shown in Figure 2.3. It is noted that Heusler compounds may also exhibit ferrimagnetic states and even PMA, and therefore possible ferrimagnetic configurations were also considered in our calculations. It is worth noting that different AFM configurations may be possible depending on where the magnetic atoms are located. For example, in a reg. cub. structure, if X atom is magnetic, then there could exist two

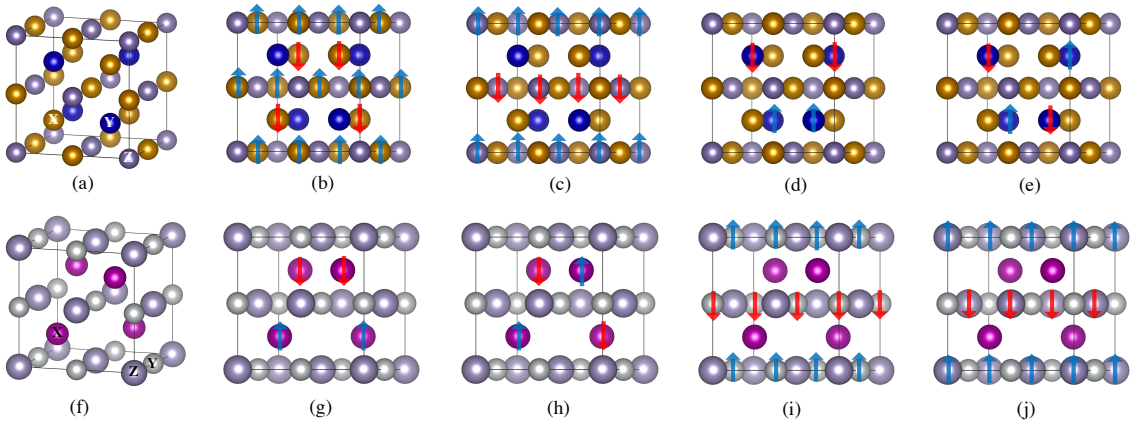

Figure 2.4: Schematic crystal structure and possible antiferromagnetic configurations for (a-e) inverse cubic full Heusler and (f-j) half Heusler. The red (blue) arrows represent the spin moment on the atoms.

AFM configurations, see Figure 2.3a and 2.3b; [60] if Y (or Z) atom is magnetic, then there is one AFM configuration, see Figure 2.3c; if more than one atom is magnetic, then a superposition of AFM configurations should be applied, see Figure 2.3d.

Similarly, we investigated magnetic ground states for the inv. cub., reg. tet., and inv. tet. full Heusler and for half Heusler compounds. The detailed AFM configurations of the inv. cub. and half Heusler compounds are shown in Figure 2.4. As for the reg. tet. and inv. tet. structures, a 45° rotation along the z-axis was made when considering the AFM configurations, and their AFM configurations can be resembled from the reg. cub. structure. After this step, 123 out of 363 full Heusler compounds and 64 out of 134 half Heusler compounds were confirmed with FM or FI ground states, see details in the Table A.1 and A.2 of the appendix and on GitHub.

(iv) **Lattice misfit** (f): The lattice misfit between the bulk full (half) Heusler X_2YZ (XYZ) and MgO substrate can be defined as $f = (\mathrm{a}_f - \mathrm{a}_s)/\mathrm{a}_s$, where a_f and a_s are the lattice constants of film and substrate, respectively. The negative (positive) sign of f indicates that the Heusler film undergoes a tensile (compressed) strain from the MgO substrate. In this work, we adopted the lattice misfit in the range of $-5\% \leqslant f \leqslant +5\%$ because a small lattice misfit between the film and substrate can reduce interfacial defects.[122] By considering the lattice misfit, 89 of out of

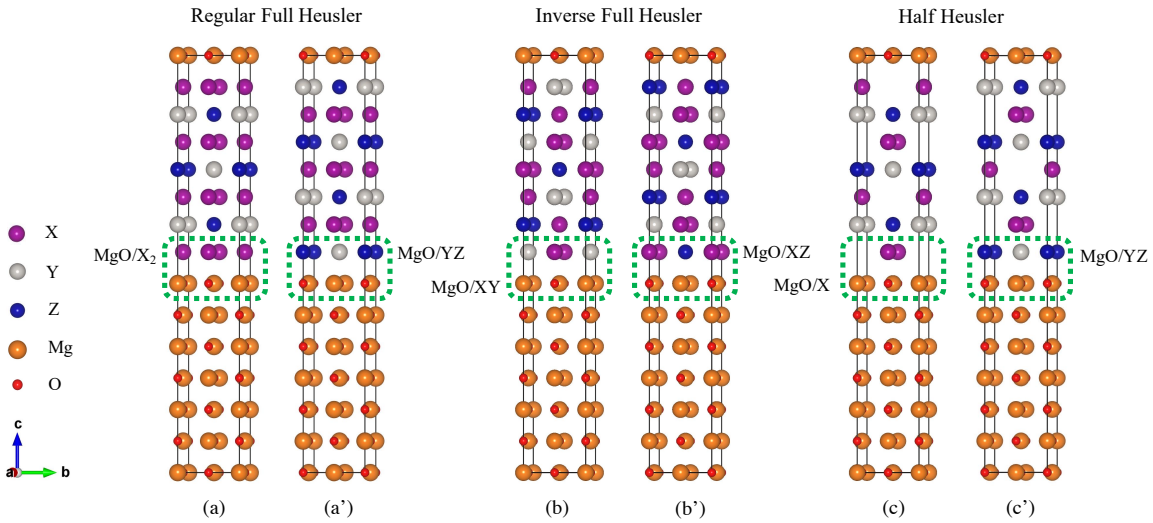

Figure 2.5: Illustration of the heterostructure models for (a,a') regular full Heusler, (b,b') inverse full Heusler, and (c,c') half Heusler. a and a' represent MgO/X_2 and MgO/YZ; b and b' represent MgO/XY and MgO/XZ; c and c' represent MgO/X and MgO/YZ interfaces, respectively. The MgO/X-based half Heusler model (c) was not employed since there is a vacancy at the interface, leading to interfacial instability.

123 full Heusler and 40 out of 64 half Heusler were found suitable for the heterostructure models with MgO.

2.3.3 Interfacial Properties

Next, we studied interfacial properties including the magnetic anisotropy constant (K_i) and cleavage energy ($E_{cleav.}$) between the screened Heusler candidates and insulating MgO layer using heterostructure models. For full Heusler (X_2YZ), there are two types of interfaces, *i.e.*, MgO/X_2 and MgO/YZ, see Figure 2.5a and 2.5b. For half Heusler (XYZ), there are also two types of interfaces, *i.e.*, MgO/X and MgO/YZ. However, as shown in Figure 2.5c, the MgO/X interface has one less atom compared to the MgO/YZ interface model, which introduces one vacancy at the interface and thus leads to the interfacial instability. Therefore, only the MgO/YZ model was considered in this work.

We calculated K_i for all these interface models and found 23 full Heusler and 3 half

Heusler candidates of which at least one interface model has a K_i value larger than 0.5 mJ/m^2. The 23 full Heusler candidates include reg. cub. Co_2CrAl, Co_2FeAl, Co_2FeGa, Co_2HfAl, Co_2HfSn, Mn_2PtCo, Ni_2MnGa, Rh_2FeIn, Rh_2MnAl, Rh_2MnGa, Rh_2MnSc, and Ru_2MnV, inv. cub. Fe_2IrGa, Fe_2IrGe, Fe_2RuGa, Mn_2CoGa, Mn_2IrGa, Mn_2IrGe, Mn_2RhGa, and Mn_2RuSn reg. tet. Mn_2TaTi, Rh_2MnSb, and Rh_2MnTi. It is worth mentioning that the bulk structures of reg. cub. Co_2CrAl, Co_2FeAl, Co_2FeGa, Co_2HfAl, Co_2HfSn, Ni_2MnGa, Rh_2MnAl and inv. cub. Mn_2CoGa, Mn_2RhGa, and Mn_2RuSn have been synthesized in experiments.[123, 124] In particular, MgO/Co_2HfSn heterostructure has K_i values of 1.19 and 1.36 mJ/m^2 for both terminations; and MgO/Fe_2IrGa and MgO/Fe_2IrGe heterostructures have K_i values of 2.74 and 2.86 mJ/m^2 for their MgO/XY termination, respectively, much larger than that in the well-known MgO/Fe system of 1.2-2.1 mJ/m^2.[11, 12, 13] The three half Heusler candidates are IrSbMn, PtCrSb, and PtMnAs, where IrSbMn has been prepared in the experiment.[125] Interestingly, the MgO/IrSbMn heterostructure shows a large K_i of 2.03 mJ/m^2. All these results are summarized in in Table 2.1 for full Heusler and Table 2.2 for half Heusler, along with other properties including the convex hull distance (E_H), cleavage energy ($E_{cleav.}$), spin-polarization (P_f), and TMR as discussed below.

For the 23 full Heusler candidates, to evaluate the relative interfacial stability for the two interfaces MgO/X_2 and MgO/YZ, we calculated their cleavage energy using following equation:[101]

$$E_{cleav.} = (E_{slab}^{X_2YZ} + E_{slab}^{MgO} - E_{HS}^{MgO/X_2YZ})/(2A), \tag{2.1}$$

where $E_{slab}^{X_2YZ}$, E_{slab}^{MgO}, andE_{HS}^{MgO/X_2YZ} are the total energy of X_2YZ slab, MgO slab, and MgO/X_2YZ heterostructure, respectively. A is the in-plane interfacial area, and factor 2 in the denominator represents two symmetrical interfaces in the heterostructure model. A larger cleavage energy means that the interface model is energetically more favorable. As shown in Table 2.1, one can clearly see that the MgO/X_2 interface is energetically more favorable than the MgO/YZ interface for most cases, except for Mn_2PtCo and Rh_2MnSc. In the case of Co_2HfAl, Ni_2MnGa, Rh_2MnGa,

Table 2.1: Summary of candidate full Heusler compounds with descriptors: $\Delta E_H \leqslant 100$, $|f| \leqslant 5\%$, and $K_i \geqslant 0.5$ for at least one interface. The ΔE_H (meV/atom) and f refer to the convex hall distance and the lattice lattice misfit with MgO substrate, respectively. The K_i (mJ/m^2), $E_{cleav.}$ (meV/Å^2), P_f, and TMR (%) represent magnetic anisotropy constant, cleavage energy, spin polarization, and tunnel magnetoresistance, respectively.

Compounds	ΔE_H	f (%)	K_i		$E_{cleav.}$		P_f		TMR	
			X_2	YZ	X_2	YZ	X_2	YZ	X_2	YZ
$Co_2CrAl^{\square*\odot}$	68	-4.8	1.40	0.07	125.47	89.57	0.84	1.00	494	inf
$Co_2FeAl^{\square*\odot}$	0	-4.6	0.91	-0.50	117.46	82.16	0.61	0.75	118	252
$Co_2FeGa^{\square*}$	0	-4.3	0.51	-0.08	115.03	56.07	0.66	0.80	156	363
$Co_2HfAl^{\square*}$	13	0.9	-0.09	0.96	127.89	61.24	0.54	1.00	80	inf
$Co_2HfSn^{\square*\odot}$	34	4.6	1.19	1.36	113.67	58.25	0.73	0.49	229	63
$Mn_2PtCo^{\square}$	0	0.8	-1.42	1.55	65.48	77.91	0.79	0.48	338	60
$Ni_2MnGa^{\square*}$	6	-2.6	0.10	0.58	101.64	51.07	0.01	0.52	0	74
$Rh_2FeIn^{\square}$	18	5.0	1.83	-0.86	94.96	26.39	0.23	0.58	11	101
$Rh_2MnAl^{\square*}$	0	0.9	-1.51	0.53	99.07	68.44	0.75	0.90	261	870
$Rh_2MnGa^{\square}$	0	1.8	-1.54	0.55	98.79	46.69	0.70	1.00	186	inf
$Rh_2MnSc^{\square}$	14	4.5	-0.35	0.86	57.65	87.44	0.44	0.30	48	19
$Ru_2MnV^{\square}$	3	0.2	0.02	0.59	117.23	96.27	0.53	0.90	80	814
$Mn_2TaTi^{\triangle}$	0	0.8	-0.23	0.63	97.49	89.08	0.43	0.62	45	127
$Rh_2MnSb^{\triangle}$	0	-1.4	0.95	-0.80	76.54	26.61	0.23	0.39	11	35
$Rh_2MnTi^{\triangle}$	0	2.8	0.60	0.26	83.61	81.15	0.07	0.83	0	448
			XY	XZ	XY	XZ	XY	XZ	XY	XZ
$Fe_2IrGa^{\boxdot\odot}$	0	-0.6	2.74	-1.17	98.24	54.61	0.67	0.36	159	30
$Fe_2IrGe^{\boxdot}$	45	-1.1	2.86	-0.92	95.55	37.54	0.12	0.25	2	13
$Fe_2RuGa^{\boxdot}$	45	-0.5	-0.24	0.62	99.58	57.04	0.61	0.56	119	91
$Mn_2CoGa^{\boxdot*\diamond}$	5	-3.6	0.06	0.51	87.18	52.09	0.34	0.20	26	8
$Mn_2IrGa^{\boxdot\diamond}$	0	0.5	1.46	0.48	76.13	49.16	0.42	0.72	42	211
$Mn_2IrGe^{\boxdot\diamond\odot}$	46	-0.4	1.54	-0.18	95.67	37.90	0.86	0.15	556	4
$Mn_2RhGa^{\boxdot*\diamond}$	47	0.1	0.57	0.81	72.69	49.83	0.65	0.73	143	222
$Mn_2RuSn^{\boxdot*\diamond}$	86	3.9	-0.01	1.00	83.82	24.96	0.09	0.28	1	17

$\square$: reg. cub., $\boxdot$: inv. cub., $\triangle$: reg. tet.

In this and subsequent table, $\diamond$ indicates the bulk compounds have a ferrimagentic ground state; $*$ indicates experimental validation of the bulk compounds; and $\odot$ represents the screened target materials using materials descriptors: $E_{cleav.}$, P_f, and TMR.

Table 2.2: Summary of candidate half Heusler compounds with descriptors: $\Delta E_H \leqslant 150$, $|f| \leqslant 5\%$, and $K_i \geqslant 0.5$.

Compounds	ΔE_H	f (%)	K_i	P_f	TMR
IrSbMn*	78	2.02	2.03	0.38	34
PtCrSb$^{\odot}$	132	3.53	1.54	0.71	199
PtMnAs$^{\odot}$	78	0.17	1.52	0.64	136

Ru_2MnV, Fe_2RuGa, and Mn_2TaTi, a positive K_i was predicted at one interface model but the corresponding interface has a relatively lower $E_{cleav.}$ than the other interface. It implies that a PMA might be less likely to be achieved in experiments because of their unstable interfacial structure.

We also calculated spin polarization (P_f) and TMR for the screened 23 full Heusler and 3 half Heusler candidates based on their Heusler/MgO heterostructure models that were built along the [001] direction of the MgO barrier. The P_f was calculated based on the spin-dependent density of states (DOS) at the Fermi level:[126]

$$P_f = \frac{\mathcal{D}_{\uparrow}(E_{\mathrm{F}}) - \mathcal{D}_{\downarrow}(E_{\mathrm{F}})}{\mathcal{D}_{\uparrow}(E_{\mathrm{F}}) + \mathcal{D}_{\downarrow}(E_{\mathrm{F}})}, \tag{2.2}$$

where $\mathcal{D}_{\uparrow}(E_{\mathrm{F}})$ and $\mathcal{D}_{\downarrow}(E_{\mathrm{F}})$ are the DOS for spin-up and spin-down channels, respectively. The TMR ratio of a MTJ was estimated using the Julliere's model: [127]

$$\mathrm{TMR} = \frac{2P_1P_2}{1 - P_1P_2}, \tag{2.3}$$

where P_1 and P_2 are spin polarization of the two FM electrodes. In the Heusler/MgO/Heusler MTJs, the same Heusler compound serves as FM electrodes whose P_f was calculated from the Heusler/MgO heterostructure, *i.e.*, $P_1 = P_2 = P_f$.

Next, we excluded the Heusler compounds with a TMR ratio less than 80% since they are not suitable for high-performance MTJ devices. For instance, in the case of Mn_2PtCo, Rh_2FeIn,

Rh_2MnSc, Fe_2IrGe, Rh_2MnSb, Rh_2MnTi, and Mn_2IrGa, these compounds were removed from our candidate list though they can form an energetically favorable interface matching with the positive K_i. Similarly, the half Heusler IrSbMn was also removed from the candidate list in spite of its large K_i of 2.03 mJ/m^2. In short, by considering all the descriptors seven candidate Heusler compounds including the reg. cub. Co_2CrAl, Co_2FeAl, Co_2HfSn, inv. cub. Fe_2IrGa and Mn_2IrGe, half Heusler PtCrSb and PtMnAs were selected as the most promising candidates for the high-performance spintronic applications.

It is noted that, very recently, a new Heusler compound, Rh_2CoSb, has been experimentally reported as a new hard magnet with a Curie temperature of 450 K and a magnetocrystalline anisotropy of 3.6 MJ/m^3.[108] Interestingly, our calculations show that Rh_2CoSb has a ΔE_H of 82 meV/atom, less than the threshold value of 100 meV/atom, and the compound does have a ferromagnetic ground state with an energy preference of 44 meV/atom, corresponding to a Curie temperature of 504 K. However, this compound was not included in our final list because it cannot form a PMA at Rh_2CoSb/MgO interface, with K_i of 0.007 mJ/m^2 for MgO/Rh_2 interface and -1.11 mJ/m^2 for MgO/CoSb interface. It is worth noting that one of the most popular Heusler compounds, Co_2FeSi, was not selected in our final list though PMA at MgO/Co_2FeSi interface has been experimentally demonstrated.[128, 129] This is because that Co_2FeSi has a large lattice misfit with MgO of more than 5%, and more importantly, the calculated K_i at both two interfaces, MgO/Co_2 and MgO/FeSi, are rather small, *e.g.*, 0.14 mJ/m^2 for MgO/FeSi interface. It is comparable with the experimental value of 0.25 mJ/m^2 at a substrate temperature of 300°C.[129]

Also noted that, in a previous experimental study, bulk PtCrSb in non-Heulser phase structure was reported as nonmagnetic.[130] However, our DFT calculations show that its ferromagnetic Heusler structure is the ground state, which awaits further experimental verification. In another work, by using *ab-initio* calculations, Ma *et al.* reported that NiMnSb/MgO (CoTiSn/MgO) interface could retain a PMA at MnMn/MgO (TiTi/MgO) interface,[131] in which

Table 2.3: Summary of seven final candidate Heusler/MgO heterostructures with calculated properties: K_i (mJ/m^2), saturation magnetization M_s (emu/cm^3), shape anisotropy K_{shape} (mJ/m^2), and effective anisotropy per unit volume K_{eff} ($\times 10^7$erg/cm^3). The interfacial layer atoms of Heusler are labeled in the brackets.

Compounds	K_i	M_s	K_{shape}	K_{eff}
Co_2CrAl	1.40 (CoCo)	472	0.11	1.63
Co_2FeAl	0.91 (CoCo)	1108	0.61	0.38
Co_2HfSn	1.19 (CoCo)	100	0.01	1.23
Fe_2IrGa	2.74 (FeIr)	1135	0.70	2.34
Mn_2IrGe	1.54 (MnIr)	862	0.46	1.10
PtCrSb	1.54 (CrSb)	642	0.26	1.29
PtMnAs	1.52 (MnAs)	895	0.46	1.18

the interface is not intrinsically from the half-Heusler/MgO heterostructure but modified by introducing one substitutional defect at the interface. In our calculations, these two compounds were excluded from the final list since their intrinsic interfaces cannot form a PMA, with K_i of 0.13 mJ/m^2 for NiMnSb/MgO and -0.24 mJ/m^2 for CoTiSn/MgO. Nevertheless, our calculations also show that these two compounds do have a ferromagnetic ground state and are thermodynamically stable, with a ΔE_H of 0 for NiMnSb and 12 meV/atom for CoTiSn. It is worth mentioning that the prototype Co_2FeAl/MgO with a K_i around 1.3 mJ/m^2 was found in our final list, which validate the rationality and effectiveness of our approach.[14, 102]

2.3.4 Robustness of Perpendicular Magnetic Anisotropy

To evaluate the robustness of PMA at the selected seven Heusler/MgO material interfaces, we calculated their effective anisotropy per unit area ($K_{\text{eff}}t_{\text{eff}}$) using the following equation:[1, 107]

$$K_{\text{eff}}t_{\text{eff}} = K_i - \frac{1}{2}\mu_0 M_s^2 t_{\text{eff}} \tag{2.4}$$

where t_{eff} is the thickness of the ferromagnetic layer, and μ_0 is the magnetic constant, and M_s is the saturation magnetization per unit volume. The term $\frac{1}{2}\mu_0 M_s^2 t_{\text{eff}}$ represents shape anisotropy per unit area (K_{shape}), which indicates the favorable energy term along the long axis, *i.e.*, the out-of-plane

direction in the case of heterostructure. Accordingly, by excluding the shape anisotropy from the K_i, the effective anisotropy K_{eff} describes how the interface contributes solely to the PMA. In this sense, a robust PMA can be determined by achieving a positive K_{eff}. The calculated K_i, M_s, K_{shape}, and K_{eff} are listed in Table 2.3. Our calculations show that all the screened candidate systems have a positive K_{eff}, indicating a robust PMA at the interface.

2.4 Conclusions

In summary, we have demonstrated a high-throughput approach to search for Heusler/MgO material interfaces with strong PMA and other desired properties for developing novel p-MTJs towards high device performance and low energy consumption. On the basis of the open quantum material repositories and five prototype structures of Heusler compounds, we have filtered around 497 thermodynamically stable ternary Heusler structures from the possible 40,000 ternary Heusler compounds using material descriptors formation energy and convex hull distance, among which 187 form ferromagnetic or ferrimagnetic coupling. By using a group of combinatorial material descriptors that determine interfacial energetic and magnetic properties, including lattice mismatch, interfacial cleavage energy, magnetic anisotropy constant, and TMR ratio, we have eventually identified five full Heusler compounds, including Co_2CrAl, Co_2HfSn, Fe_2IrGa, Mn_2IrGe, and two half-Heusler compounds PtCrSb and PtMnAs for developing novel MgO-based p-MTJs for high-performance spintronic applications. This work demonstrates an efficient approach to search for functional material interfaces by using the open quantum material repositories, developing effective material descriptors, and the large-scale *ab-initio* calculations, which can be transformative to the discovery of other types of advanced functional materials beyond Heusler compounds.

2.5 Acknowledgement

Chapter 2, in full, is a reprint of the material “High-throughput design of interfacial perpendicular magnetic anisotropy at Heusler/MgO heterostructures” as it appears in ACS Applied Materials & Interfaces, Sicong Jiang, Safdar Nazir, Kesong Yang, 14, 9734-9743, 2022. The dissertation author was the primary investigator and author of this paper.

Chapter 3

Origin of the large interfacial perpendicular magnetic anisotropy in MgO/Co_2FeAl

In chapter 2, after a systematic high-throughput screening, five full Heusler compounds, including Co_2CrAl, Co_2FeAl, Co_2HfSn, Fe_2IrGa, Mn_2IrGe, and two half-Heusler compounds PtCrSb and PtMnAs were found promising for designing p-MTJs. In this chapter, we investigated the origin of the large interfacial PMA in the MgO/Co_2FeAl structure by modeling four types of interface models for MgO/Co_2FeAl system using first-principles calculations. The origin were explained from the atomic-resolved and orbital-resolved K_i along with the perturbation theory energy analysis. In addition, we also studied the influence of 26 capping layers on the interfacial magnetic anisotropy of MgO/Co_2FeAl. This work clarifies the atomistic origin of the interfacial perpendicular magnetic anisotropy and provides guidance to further enhance interfacial K_i by adding capping layers in the MgO/Co_2FeAl.

3.1 Introduction

Magnetic tunnel junctions (MTJs) consisting of two ferromagnetic (FM) layers separated by a thin insulating barrier are core components in spin-transfer-torque magnetic random-access memory (STT-MRAM).[132, 133] In particular, the perpendicular MTJs (p-MTJs) that possessed perpendicular magnetic anisotropy (PMA) have attracted great attention in recent years because of their promising applications in the next-generation spintronic devices towards using faster and smaller magnetic bits.[134, 135, 9, 136] In p-MTJs, PMA occurs at the interface between ferromagnetic thin film and insulating barrier and its strength is characterized by the magnetic anisotropy constant (K_i), which is defined as the anisotropy energy per unit area.[13] To achieve a high thermal stability of the relative magnetization orientation of the two ferromagnetic electrodes, a large K_i is desired. As p-MTJs shrink to the nanometer scale, a larger K_i is necessary to sustain a sufficient thermal stability. A recent theoretical calculation indicated that a K_i of 4.7 mJ/m^2 is needed for a data retention time of ten years when the memory devices scale down to 10 nm.[8]

PMA has been traditionally achieved at interfaces between ferromagnetic and nonmagnetic heavy metals such as Co/Pt, however, their K_i is small (less than 1 mJ/m^2).[94] In 2010, a large K_i of 1.3 mJ/m^2 was reported at MgO/CoFeB interface, and the MTJ based on this material interface exhibits a high tunnel magnetoresistance ratio of 120% and a low switching current of about 49 μA.[9] Since then, great research efforts have been made either to tune K_i at MgO/Fe interface[13] or to explore the possibility of producing large K_i at novel MgO-based interfaces.[102, 137] Co_2FeAl, one prototype compound of full Heusler family, has received increasing interests as one possible alternative to Fe and CoFeB in the MgO-based p-MTJs in recent years because of its excellent properties including high spin polarization,[19] low magnetic damping constant (about 0.001),[20] and small lattice mismatch[138] between Co_2FeAl film and MgO substrate ($\sim$4 %). The magnetic anisotropy at MgO/Co_2FeAl interface was first reported in 2011 and was found very sensitive to the annealing.[139, 102, 137] Jiang's team[139] and Inomata's team[102] both

reported a PMA at MgO/Co_2FeAl interface, independently, and found a magnetic anisotropy transition from in-plane to out-of-plane after annealing. [102] In contrast, in-plane magnetic anisotropy was also found at MgO/Co_2FeAl interface and showed different behavior with the annealing temperature.[137, 140] A very recent experimental study also reported an evolution of the PMA at the interface between MgO and Co_2FeAl, *i.e.*, a K_i of zero for as-deposited samples and a K_i of 1.14 (2.01) mJ/m^2 for samples annealed at 320 (450)°C, which is attributed to the modification of the interface during the thermal treatment.[14]

PMA is mainly determined by the magnetic ions of a few monolayers near the interfacial region and there exist two types of interfaces in the MgO/Co_2FeAl heterostructure, *i.e.*, MgO/Co_2 and MgO/FeAl. Accordingly, one may speculate that the different magnetic anisotropy is caused by the different interfacial terminations between MgO substrate and Co_2FeAl film. Inomata's team investigated the PMA at the MgO/Co_2FeAl interface using angular-dependent x-ray magnetic circular dichroism (XMCD), and attributed the PMA mostly to the interfacial Fe atoms at the MgO/FeAl interface.[141] Later, the same team also argued that the PMA at the Co_2FeAl heterostructure is mainly contributed by the large perpendicular orbital magnetic moments of interfacial Fe ions from XMCD measurement.[142] A prior theoretical study indicated that oxygen-top FeAl termination has the highest thermal stability on the basis of density functional theory calculations,[143] which seems to support the above arguments. However, a recent computational study indicated that FeAl-termination at MgO/Co_2FeAl interface lead to an in-plane instead of out-of-plane magnetic anisotropy, while Co-termination showed the PMA with K_i up to 1.31 mJ/m^2.[16] Therefore, to clarify the atomistic origin of the magnetic anisotropy at the MgO/Co_2FeAl interface, a comprehensive study of the interfacial magnetic properties and evaluation of the relative thermodynamic stability of the two types of materials interfaces are very necessary.

Additionally, a series of recent experimental and computational studies both indicated that metal-based capping layers have a significant influence on the K_i of MgO/Co_2FeAl heterostructure,

[15, 144] in which capping layers are often used to protect the ferromagnetic layers. For instance, Cr-capped MgO/Co_2FeAl showed an in-plane magnetic anisotropy with a K_i of -0.46 mJ/m^2 while Ta-capped film exhibited a PMA with a K_i of 0.74 mJ/m^2.[15] Gabor *et al* also reported a similar K_i of 0.67 mJ/m^2 in the Ta/Co_2FeAl/MgO multilayers even in the as-deposited state.[144] As a result, adding one capping layer on MgO/Co_2FeAl heterostructure not only protects the ferromagnetic layer but also plays an important role in tuning the K_i. Consequently, a systematic evaluation of the influence of all the possible metal-based capping layers on the K_i of MgO/Co_2FeAl heterostructure is of great importance, and so far, there has been no such a report.

In this research article, we reported a comprehensive study of the interfacial magnetic and energetic properties for the MgO/Co_2FeAl interface without and with capping layers, consisting of two sections. In the first section, we considered four types of MgO/Co_2FeAl models without capping layers, including MgO/Co_2...FeAl, MgO/Co_2...Co_2, MgO/FeAl...Co_2, and MgO/FeAl...FeAl, and investigated their layer-resolved and atomic orbital-resolved K_i and interfacial cleavage energy. In the second section, we systematically investigated the influence of 26 capping layers on the interfacial K_i of the MgO/Co_2...FeAl and MgO/Co_2...Co_2 systems. Our calculations indicate that adding Fe- and W-capping layers can significantly increase the K_i of the system, and particularly, W capping leads to a giant K_i of 4.90 mJ/m^2 in MgO/Co_2...FeAl/W model. This work clarified the atomistic origin of the interfacial perpendicular magnetic anisotropy at MgO/Co_2FeAl, providing some guidance to develop novel p-MTJs with high thermal stability and large K_i.

3.2 Computational Details

DFT calculations with spin-orbit coupling (SOC) were carried out using Vienna *Ab-initio* Simulation Package (VASP).[145, 146] The projector augmented wave (PAW) pseudopotentials were employed for treating electron-ion interactions,[114] and the generalized gradient approximation (GGA) parameterized by Perdew-Burke-Ernzerhof (PBE) was used for exchange-correction

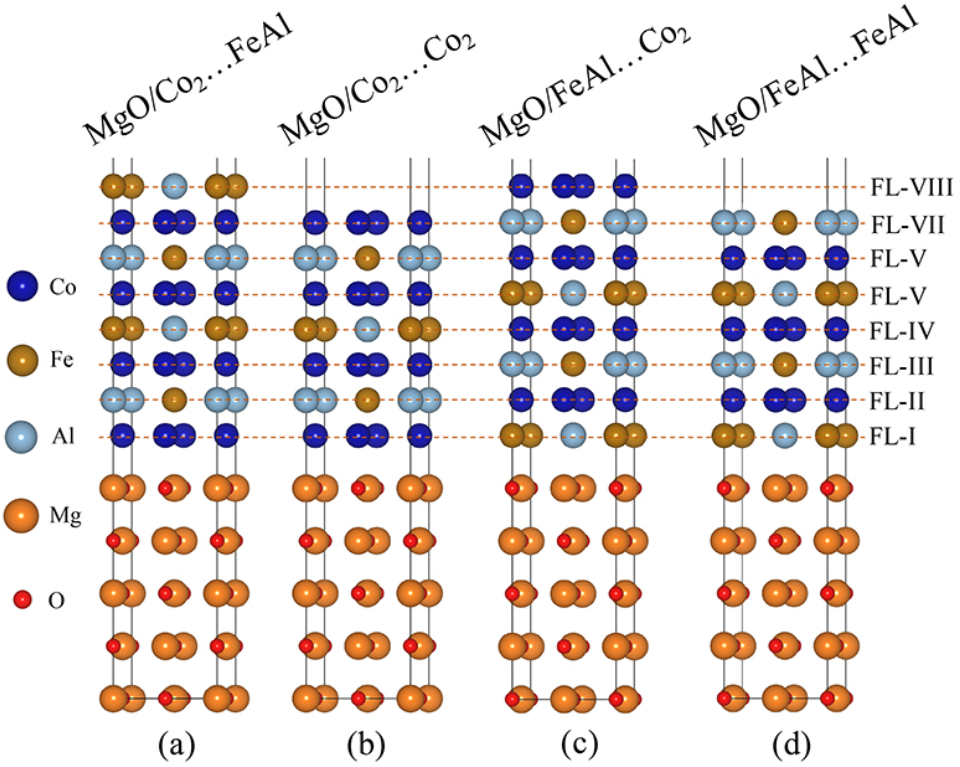

Figure 3.1: Schematic crystal structures of uncapped MgO/Co_2FeAl heterostructures. (a) MgO/Co_2 interface with FeAl surface (MgO/Co_2...FeAl), (b) MgO/Co_2 interface with Co_2 surface (MgO/Co_2...Co_2), (c) MgO/FeAl interface with Co_2 surface (MgO/FeAl...Co_2), (d) MgO/FeAl interface with FeAl surface (MgO/FeAl...FeAl).

functional.[147] The cut-off kinetic energy for plane waves was set as 450 eV. Γ-centered k-point grids were set as $6 \times 6 \times 1$ and $21 \times 21 \times 1$ for ionic relaxation and static calculations, respectively, which were determined by a careful convergence test for the perpendicular magnetic anisotropy constant (K_i), total energy, and cleavage energy of the heterostructure models, see Fig. 3.2. The convergence threshold for electronic self-consistency loop was set to 10^{-6} eV. All the atomic positions and lattice structures were fully relaxed until the residual forces were smaller than 0.02 eV/Å in the structural relaxation. The density of states (DOS) was calculated using the tetrahedron method with Blöchl corrections.[148] The in-plane lattice constant of the MgO/Co_2FeAl heterostructure model was fixed to the lattice constant of MgO (4.215Å).

The K_i was calculated by $(E_{[100]} - E_{[001]})$/A, where $E_{[100]}$ and $E_{[001]}$ represent total

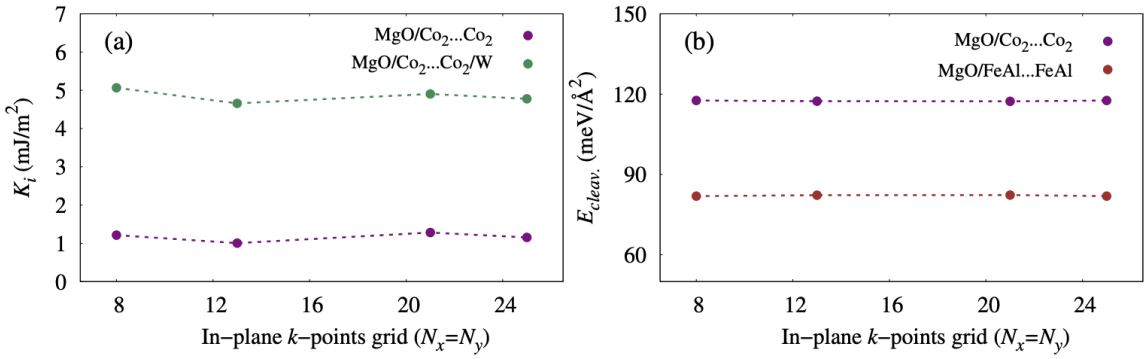

Figure 3.2: Calculated (a) interfacial magnetic anisotropy constant (K_i) and (b) cleavage energy ($E_{cleav.}$) with respect to the in-plane k-points grid.

energy with magnetization along [100] and [001] direction in a fully self-consistent-field manner, respectively, and A is the in-plane area. It is realized that another approach, *i.e.*, a so-called "force theorem", can also be used to calculate K_i, in which a fully self-consistent collinear calculation is required as the first step. After that, non-collinear calculations with magnetization along [100] and [001] direction are carried out using the frozen charge density produced from the collinear calculation, and then the K_i can be calculated based on the energy differences.[149] These two methods generally give consistent results for non-heavy metal systems, such as Fe/MgO and Fe/$MgAl_2O_4$.[150] However, according to a recent theoretical report, the results might be different for systems with heavy metals, such as Pt and Ir.[151] In this work, to avoid the failure of perturbation theory, the first approach, that is, the fully self-consistent non-collinear SOC calculations were used for K_i.

3.3 Results and Discussion

3.3.1 Uncapped MgO/Co_2FeAl

We began our study by investigating the interfacial magnetic anisotropy (K_i) and energetic properties of uncapped MgO/Co_2FeAl. Co_2FeAl has a cubic crystal structure ($L2_1$) with a

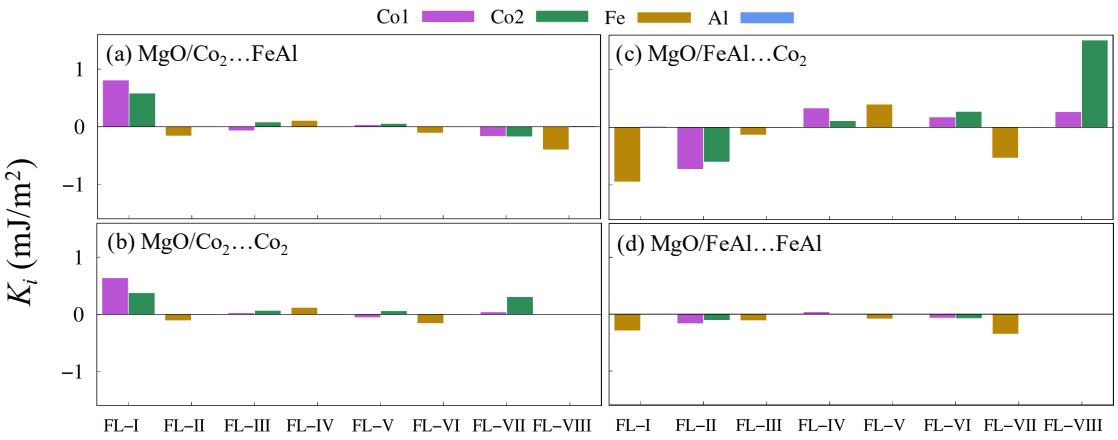

Figure 3.3: Calculated layer-resolved K_i values of different atoms for (a) MgO/Co_2...FeAl, (b) MgO/Co_2...Co_2, (c) MgO/FeAl...Co_2, (d) MgO/FeAl...FeAl structures. Label FL-I to FL-VIII corresponds with the layers from MgO/Co_2FeAl interface to Co_2FeAl surface. The purple and green bars represent two different Co atoms in the same layer, while the green and blue bars indicate Fe and Al atom, respectively in the same layer.

space group No.225 $Fm\bar{3}m$.[124, 137] The calculated lattice constants of bulk Co_2FeAl and MgO are 5.697 and 4.215 Å, respectively, close to their experimental values 5.730 and 4.211 Å.[124, 116] To match the lattice constant of MgO substrate, a 45° rotation along [001] direction was made on the conventional lattice structure of Co_2FeAl, which yields a lattice mismatch of -4.4%. The negative sign here indicates that the Co_2FeAl film undergoes a tensile strain from the MgO substrate. In principle, there are four types of MgO/Co_2FeAl slab-based heterostructure models, with all the possible combinations between the two types of MgO/Co_2FeAl interfaces (MgO/Co_2 and MgO/FeAl interfaces) and two types of Co_2FeAl surfaces (with Co_2 and FeAl terminations), as shown in Fig. 3.1. The layers in the Co_2FeAl film from the MgO/Co_2FeAl interface to the Co_2FeAl surface are labeled as FL-I to FL-VIII, respectively. For convenience, the

Table 3.1: Total K_i values of uncapped MgO/Co_2FeAl system with different terminations.

Structure	K_i (mJ/m^2)
MgO/Co_2...FeAl	0.60
MgO/Co_2...Co_2	1.28
MgO/FeAl...Co_2	0.12
MgO/FeAl...FeAl	-1.13

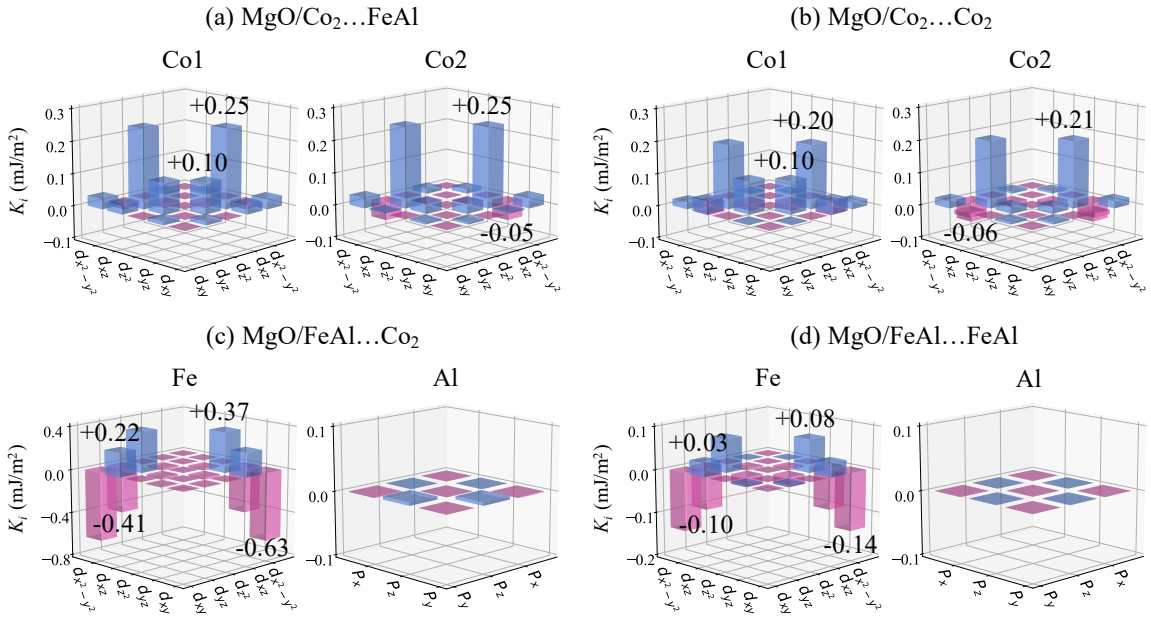

Figure 3.4: Calculated atomic-resolved K_i contributions from different orbital hybridizations. (a) and (b) are *d*-orbital hybridization of interfacial Co atoms in MgO/Co_2...FeAl and MgO/Co_2...Co_2 structure, respectively. (c) and (d) are *d*-orbital hybridization of interfacial Fe atom and *p*-orbital hybridization of interfacial Al atom in MgO/FeAl...Co_2 and MgO/FeAl...FeAl structure, respectively.

heterostructure model consisting of MgO/Co_2 interface and FeAl-terminated surface is referred to as MgO/Co_2...FeAl, along with the other three models, MgO/Co_2...Co_2, MgO/FeAl...Co_2, and MgO/FeAl...FeAl.

In each model, Co_2FeAl film was built on the MgO substrate with a thickness of five monolayers along [001] direction, and a thickness of more than 15 Å vacuum was added on the film to avoid the interaction between images in the periodic lattice. Our test calculations show that increasing the thickness of MgO monolayers more than five has no effects on the magnetic anisotropy, which is consistent with the prior computational study,[16] see Fig. 3.5 in the appendix. It is realized that, however, when the MgO was grown on the ferromagnetic Co_2FeAl as over-layers, its thickness could be a crucial factor that influence the magnetic anisotropy of MgO/Co_2FeAl system according to a recent experimental study.[152]

The K_i as a function of the thickness of Co_2FeAl film (number of layers) was studied for

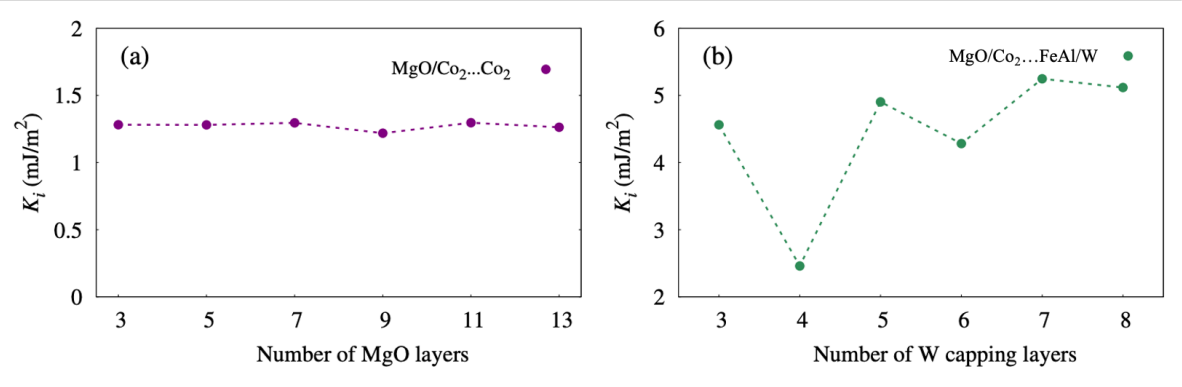

Figure 3.5: Calculated K_i with respect to the number of (a) MgO layers and (b) W capping layers.

the four types of heterostructure models, MgO/Co_2...FeAl, MgO/Co_2...Co_2, MgO/FeAl...Co_2, and MgO/FeAl...FeAl. Our calculations show that the calculated K_i generally tends to be saturated when the number of Co_2FeAl layers is larger than five for all the types of heterostructure models, as shown in the Fig. 3.6 of appendix. This implies there exists a range of the film thickness to produce the desired perpendicular magnetic anisotropy. In fact, it was experimentally reported that the critical thickness for Co_2FeAl film to maintain out-of-plane K_i was around 1.1 nm after annealing at 300°C.[102, 153] Therefore, in this work, we choose seven layers (the thickness of Co_2FeAl film is about 0.8 nm) for MgO/Co_2...FeAl and MgO/FeAl...Co_2 system, and eight layers (about 1 nm) for MgO/FeAl...Co_2 and MgO/FeAl...FeAl system to build up the uncapped MgO/Co_2FeAl models. Additionally, it is worth noting that the MgO/FeAl...FeAl model has a positive K_i (with an easy magnetization axis along out-of-plane direction) when the Co_2FeAl film is ultra thin (one layer), and the K_i becomes negative (with an easy magnetization axis along in-plane direction) for multilayers of Co_2FeAl film. The calculated K_i of MgO/Co_2FeAl model with the designated film thickness are 0.60 mJ/m^2 for MgO/Co_2...FeAl, 1.28 mJ/m^2 for MgO/Co_2...Co_2, 0.12 mJ/m^2 for MgO/FeAl...Co_2, and -1.13 mJ/m^2 for MgO/FeAl...FeAl, as listed in Table 3.1. Our calculated K_i of 1.28 mJ/m^2 for MgO/Co_2...Co_2 structure is in good agreement with experimental values of 1.04 mJ/m^2[102] and 1.14 mJ/m^2[14], and is also well consistent with a recent DFT calculation of 1.31 mJ/m^2.[16]

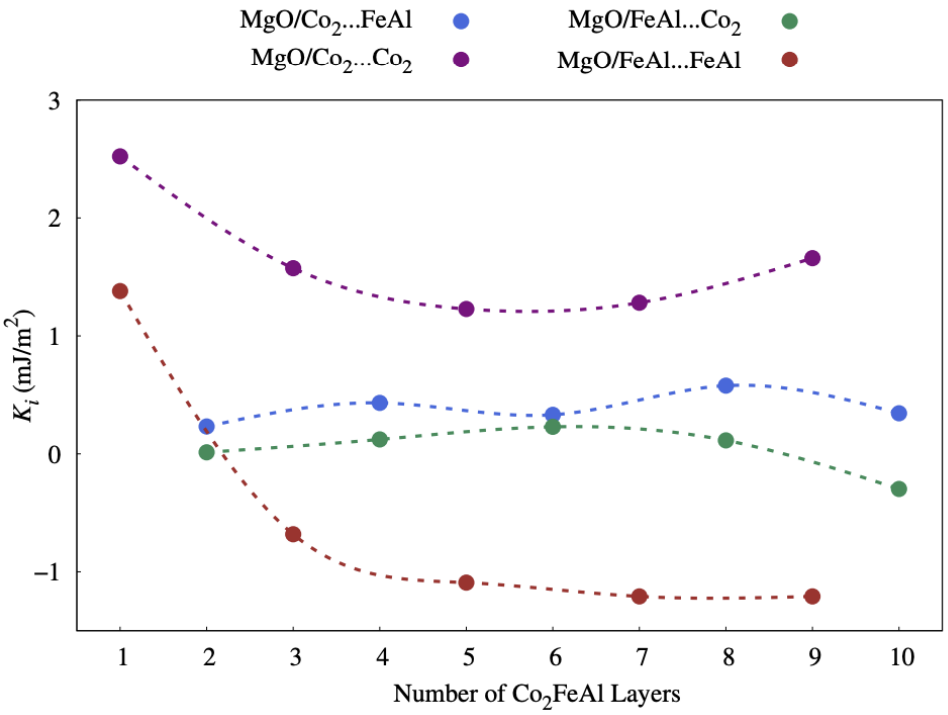

Figure 3.6: Calculated K_i MgO/Co_2FeAl with respect to number of Co_2FeAl layers.

The effective anisotropy for the MgO/Co_2...Co_2 model was estimated using the equation:[1, 107]

$$K_{\text{eff}} t_{\text{eff}} = K_i - \frac{1}{2}\mu_0 M_s^2 t_{\text{eff}} \tag{3.1}$$

where K_{eff} is the effective anisotropy per unit volume, t_{eff} is the thickness of the ferromagnetic layer, μ_0 is the magnetic constant, and M_s is the saturation magnetization per unit volume. The term $\frac{1}{2}\mu_0 M_s^2$ represents demagnetizing energy per unit volume. In our calculations, the total magnetization for MgO/Co_2...Co_2 is 17.15 μ_B, and the effective thickness is 7.944 Å. Accordingly, the saturation magnetization M_s can be estimated to be 1127 emu/cm^3, which is close to the experimental value of 1140 emu/cm^3.[14] The term $\frac{1}{2}\mu_0 M_s^2 t_{\text{eff}}$ can be estimated to be around 0.63 mJ/m^2, which is much less than the K_i considered in this study. Therefore, it is reasonable to conclude that the effective anisotropy still favors the PMA in the MgO/Co_2...Co_2 model.

To understand the origin of the K_i, we calculated layer-resolved K_i for the four types of

models, which clearly shows the atomic contributions to the K_i, see Fig. 3.3. The layer-resolved K_i was calculated based on the energy difference in non-collinear calculations projected for the atom in each layer. As one can see, Al atom barely contributes to K_i, however, Co and Fe atoms play an important role in producing the K_i. For the models MgO/Co_2...FeAl and MgO/Co_2...Co_2, the two interfacial Co atoms in the FL-I layer contribute most of the out-of-plane K_i, resulting in a positive total K_i of 0.60 mJ/m^2 and 1.28 mJ/m^2, respectively, see Fig. 3.3a and 3.3b. On the contrary, for the models MgO/FeAl...Co_2 and MgO/FeAl...FeAl, the interfacial Fe atoms (FL-I) and Co atoms (IF-II) cause negative K_i, which explains the relatively low K_i (0.12 mJ/m^2) in MgO/FeAl...Co_2 and even negative K_i (-1.13 mJ/m^2) in MgO/FeAl...FeAl. In the model MgO/FeAl...Co_2, the surface Co atoms in the layer FL-VIII cause a large out-of-plane K_i, cancels out the in-plane K_i, and leads to a total positive but low K_i, see Fig. 3.3c. In the model MgO/FeAl...FeAl, almost all the layers contribute in-plane K_i, leading to a total negative K_i, see Fig. 3.3d. Interestingly, although the models MgO/FeAl...Co_2 and MgO/FeAl...FeAl share the same interface, *i.e.*, MgO/FeAl, their layer-resolved K_i are significantly different, which may be attributed to the structure symmetry of the Co_2FeAl layer.[133] That is, one additional Co_2 layer in the MgO/FeAl...Co_2 model can significantly change the layer-resolved K_i compared to the model MgO/FeAl...FeAl in which the ferromagnetic Co_2FeAl layer is symmetrical. In short, our calculations reveal that the MgO/Co_2 interface produces the out-of-plane K_i while the MgO/FeAl interface produces in-plane K_i.

To further understand the microscopic origin of K_i, we calculated orbital-resolved K_i for the interfacial atoms, *i.e.*, Co 3*d* orbitals at the MgO/Co_2 interface and Fe 3*d* and Al 3*p* orbitals at MgO/FeAl interface, as shown in Fig. 3.4. For the models MgO/Co_2...FeAl and MgO/Co_2...Co_2, the out-of-plane K_i mainly comes from hybridization between d_{xz} and d_{yz} orbitals of the interfacial Co atoms at the MgO/Co_2 interface, around 0.25 mJ/m^2 and 0.20 mJ/m^2, respectively, see Fig. 3.4a and 3.4b. The hybridization between d_{z^2} and d_{yz} also contributes to the out-of-plane K_i in both structures, however, the magnitude is much small. For the models MgO/FeAl...FeAl and

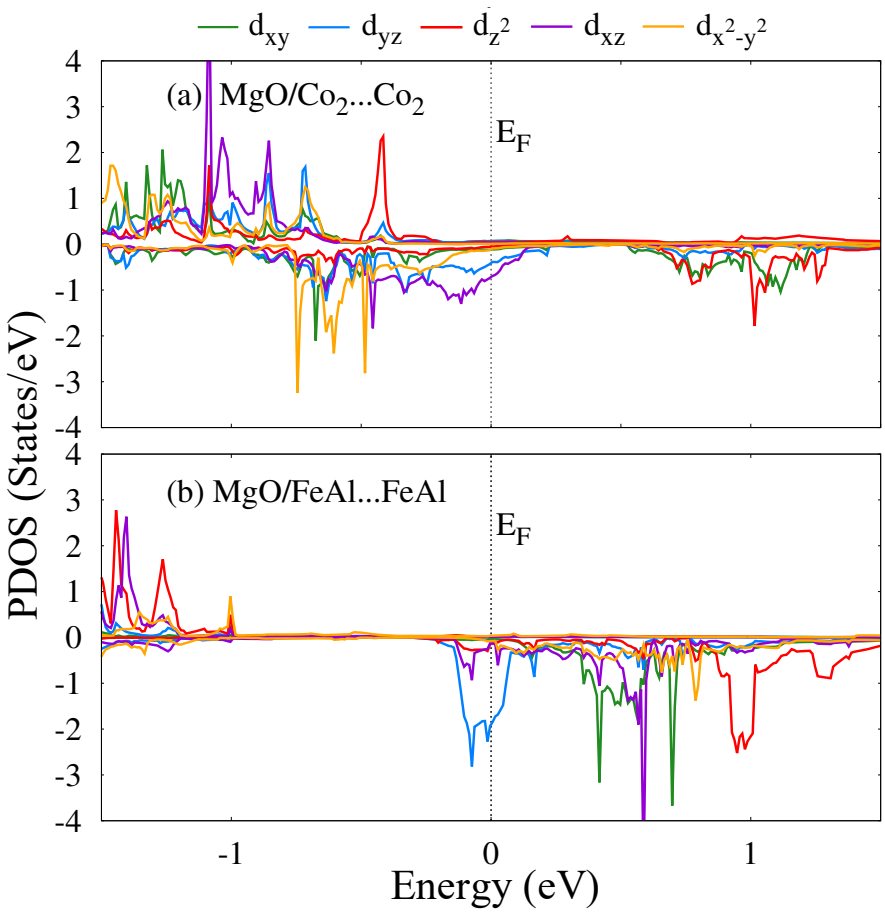

Figure 3.7: Calculated projected density of states (PDOS) of *d* orbitals for (a) Co2 atom at MgO/Co_2 interface in the $MgO/Co_2...Co_2$ model and (b) Fe atom at MgO/FeAl interface in the MgO/FeAl...FeAl model.

$MgO/FeAl...Co_2$, d_{xz} and d_{yz} orbital hybridization of Fe atoms at MgO/FeAl interface also yields out-of-plane K_i, about 0.37 $mJ/m^2$and 0.08 mJ/m^2, respectively, as shown in Fig. 3.4c and 3.4d. However, the orbital hybridization between $d_{x^2-y^2}$ and d_{xy}, and $d_{x^2-y^2}$ and d_{yz}, leads to an in-plane (negative) K_i and the resulting relatively low out-of-plane total K_i for the model $MgO/FeAl...Co_2$ and even negative K_i for MgO/FeAl...FeAl model.

The SOC effects on the magnetic anisotropy energy (MAE) can be derived from the

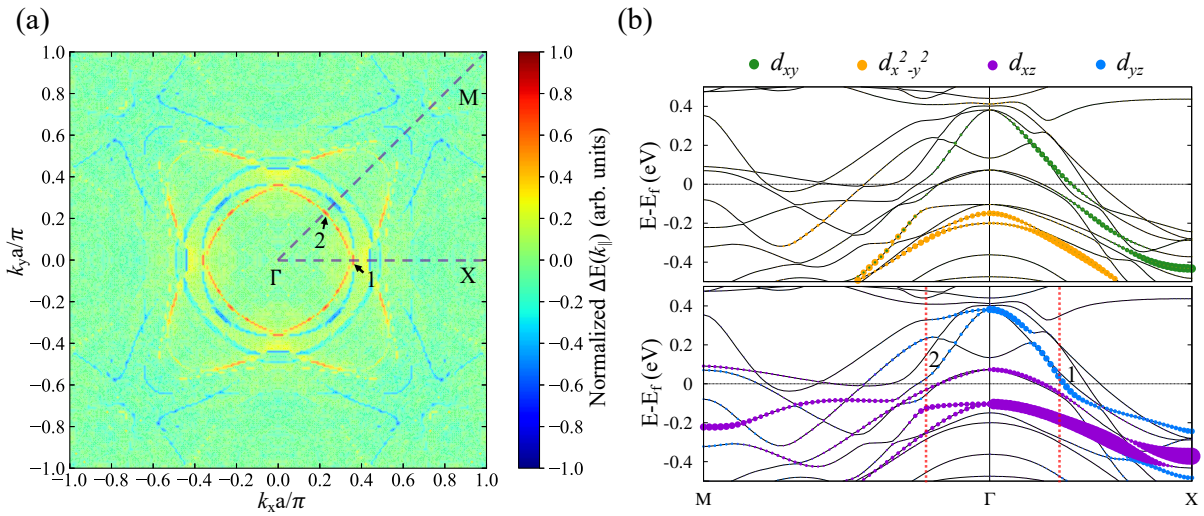

Figure 3.8: The k-resolved MAE and d-orbital projected band structure for MgO/Co_2...Co_2 structure. (a) Distribution of MAE of interfacial Co atom (Co atom at MgO/Co_2 interface) in the 2D Brillouin zone. The MAE value was normalized to the maximum positive value of the 2D Brillouin zone. The red and blue colors represent out-of-plane and in-plane MAE, respectively. (b) d-orbital projected band structure of interfacial Co atom in spin-down states. The positions of vertical red dash lines 1 and 2 correspond to the out-of-plane MAE from coupling between d_{xz} and d_{yz} orbitals.

second perturbation theory:[154]

$$
\begin{aligned}
MAE \approx & (\xi)^2 \sum_{o^{\downarrow},u^{\downarrow}} \frac{|\langle o^{\downarrow}|L_z|u^{\downarrow}\rangle|^2 - |\langle o^{\downarrow}|L_x|u^{\downarrow}\rangle|^2}{\varepsilon_{u^{\downarrow}} - \varepsilon_{o^{\downarrow}}} \\
& + (\xi)^2 \sum_{o^{\uparrow},u^{\downarrow}} \frac{|\langle o^{\uparrow}|L_x|u^{\downarrow}\rangle|^2 - |\langle o^{\uparrow}|L_z|u^{\downarrow}\rangle|^2}{\varepsilon_{u^{\downarrow}} - \varepsilon_{o^{\uparrow}}}
\end{aligned}
\tag{3.2}
$$

where ξ is the SOC constant; $o^{\uparrow}(u^{\uparrow})$ and $o^{\downarrow}(u^{\downarrow})$ denote the occupied (unoccupied) spin-up and spin-down eigenstates, respectively; $\varepsilon_{o^{\uparrow}(u^{\uparrow})}$ and $\varepsilon_{o^{\downarrow}(u^{\downarrow})}$ represent eigenvalues of occupied (unoccupied) spin-up and spin-down states, respectively; the $L_z(L_x)$ are the angular momentum operators. This theory has been used to successfully explain the K_i distribution of interfacial Fe over Brillouin zone in Fe/MgO,[155, 156] Fe/$CuInSe_2$,[157] and Fe/$MgAl_2O_4$.[150] For a system with a large spin polarization like MgO/Co_2FeAl, the coupling effects from the opposite spin channel can be neglected, and thus the MAE is mainly determined by the coupling between

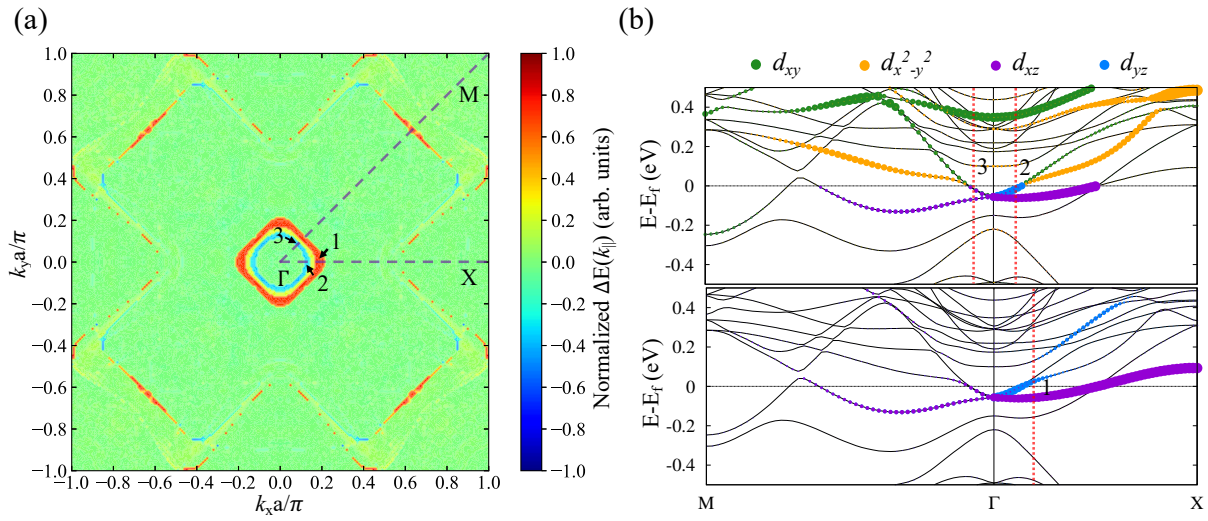

Figure 3.9: The k-resolved MAE and d-orbital projected band structure for MgO/FeAl...FeAl structure. (a) Distribution of MAE of interfacial Fe atom (Fe atom at MgO/FeAl interface) in the 2D Brillouin zone. The MAE value was normalized to the maximum positive value of the 2D Brillouin zone. The red and blue colors represent out-of-plane and in-plane MAE, respectively. (b) d-orbital projected band structure of interfacial Fe atom in spin-down states. The position of vertical red dash line 1 corresponds to the out-of-plane MAE from coupling between d_{xz} and d_{yz} orbitals, and the positions of vertical red dash lines 2 and 3 correspond to the in-plane MAE from coupling between d_{yz} and $d_{x^2-y^2}$ orbitals and coupling between d_{xz} and $d_{x^2-y^2}$ orbitals.

the occupied and unoccupied spin-down states near the Fermi level.[154] In this case, the orbital coupling between occupied and unoccupied states yields a positive K_i if these states share the same quantum number $|m|$, and the coupling yields a negative K_i if the quantum numbers of these states differ by one. To be specific, the orbital coupling between occupied and unoccupied spin-down states, *i.e.*, d_{xy} and $d_{x^2-y^2}$ (with $|m| = 2$), and between d_{xz} and d_{yz} (with $|m| = 1$) will contribute to a positive K_i.[1, 158]

To qualitatively understand how the orbital hybridization determines magnetic anisotropy, we calculated projected density of states (PDOS) of d orbitals for the interfacial Co atom in MgO/Co_2...Co_2 model and for the interfacial Fe atom in MgO/FeAl...FeAl model, as shown in Fig. 3.7a and 3.7b, respectively. For the MgO/Co_2...Co_2 model, spin-down d_{yz} and d_{xz} orbitals contribute both occupied and unoccupied states in the very vicinity ($\pm$0.1 eV) of the Fermi level, and hence their orbital coupling between occupied and unoccupied states leads to an out-of-plane

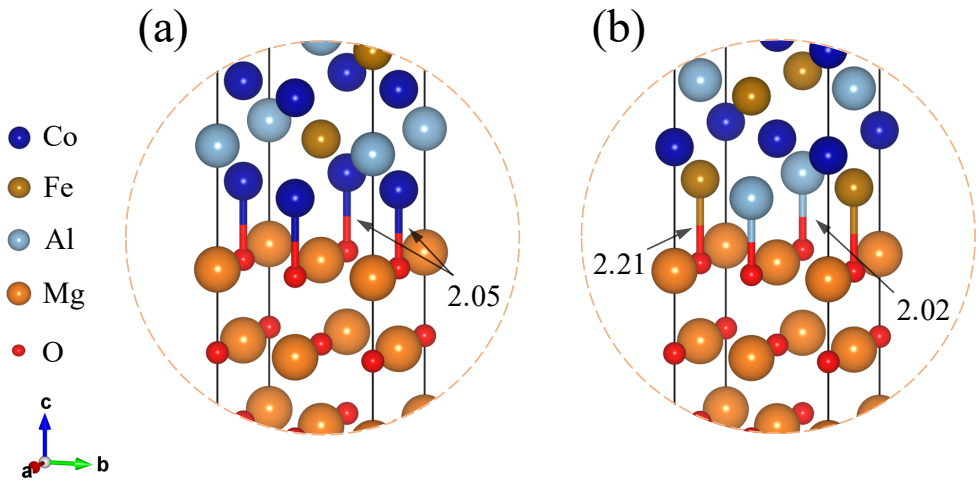

Figure 3.10: Schematic illustration of interfacial bond length in the unit of Å at (a) MgO/Co_2 interface and (b) MgO/FeAl interface.

K_i. This is also consistent with the orbital-resolved K_i in Fig. 3.4b. For the MgO/FeAl...FeAl model, the orbital coupling between occupied d_{xz} and unoccupied d_{yz} states leads to positive K_i, as shown in the orbital-resolved K_i in Fig. 3.4d, similar to the case of MgO/Co_2...Co_2 model. However, as discussed below from the k-space-resolved MAE, the orbital coupling between d_{yz} (d_{xz}) and $d_{x^2-y^2}$ states leads to negative K_i, thus resulting in a negative K_i in total.

To deeply understand the relationship between orbital hybridization and magnetic anisotropy, we further calculated k-space-resolved MAE projected on the two-dimensional interfacial Brillouin zone using a so-called "force theorem" approach[159], see Fig. 3.8a and 3.9a. The d-orbital projected band structures for the two models, MgO/Co_2...Co_2 and MgO/FeAl...FeAl, are also shown in Fig. 3.8b and 3.9b, respectively. For the MgO/Co_2...Co_2 model, as shown in Fig. 3.8a and 3.8b, its positive MAE at k-points 1 and 2 arises from the coupling between occupied and unoccupied spin-down states d_{xz} and d_{yz} along Γ-M and Γ-X, respectively. This conclusion is also in good agreement with our orbital-resolved K_i values for interfacial Co atoms in Fig. 3.4b. For MgO/FeAl...FeAl model, as shown in Fig. 3.9a and 3.9b, its positive MAE at k-point 1 arises from the coupling between occupied and unoccupied spin-down states d_{xz} and d_{yz} along Γ-X;

while the negative MAE at k-points 2 and 3 comes from the coupling between occupied and unoccupied spin-down d_{yz} and $d_{x^2-y^2}$ orbitals along Γ-X and between d_{xz} and $d_{x^2-y^2}$ orbitals along Γ-M, respectively.

To evaluate relative interfacial thermal stability, we calculated cleavage energy of MgO/Co_2 and MgO/FeAl interfaces using the bulk heterostructure model of MgO/Co_2FeAl (without vacuum) based on the below equation:[160]

$$E_{cleav.} = (E_{slab}^{Co_2FeAl} + E_{slab}^{MgO} - E_{HS}^{MgO/Co_2FeAl})/2A \tag{3.3}$$

where $E_{slab}^{Co_2FeAl}$, E_{slab}^{MgO}, andE_{HS}^{MgO/Co_2FeAl} are the total energy of Co_2FeAl slab, MgO slab, and MgO/Co_2FeAl heterostructure, respectively. A is the in-plane interfacial area, and factor 2 in the denominator represents two symmetrical interfaces in the heterostructure model. The calculated cleavage energy was 117 meV/Å^2 for MgO/Co_2 interface and 82 meV/Å^2 for MgO/FeAl interface, indicating that the MgO/Co_2 interface is energetically more favorable than the MgO/FeAl interface. Accordingly, we can conclude that the MgO/Co_2 interface is more likely to be formed than the MgO/FeAl interface in the experiments. Considering the positive K_i at MgO/Co_2 interface and the negative (or close to zero) K_i at MgO/FeAl interface, this conclusion is also well consistent with the experimentally observed perpendicular magnetic anisotropy at the interface of MgO/Co_2FeAl.[14, 102]

The relative thermal stability of the two interface models can be understood from the interfacial bond length and the resulting bond strength. The local geometrical structures of the two interface models are shown in Fig. 3.10. The two Co-O bonds at MgO/Co_2 interface are equivalent, with a bond length of 2.05 Å, while at MgO/FeAl interface, the relaxed Fe-O and Al-O bonds are different mainly because of the different atomic radii for Fe and Al, with a bond length of 2.21 Å and 2.02 Å, respectively. Accordingly, the relatively low cleavage energy at MgO/FeAl interface can be attributed to the unmatched Fe-O and Al-O bond length and the

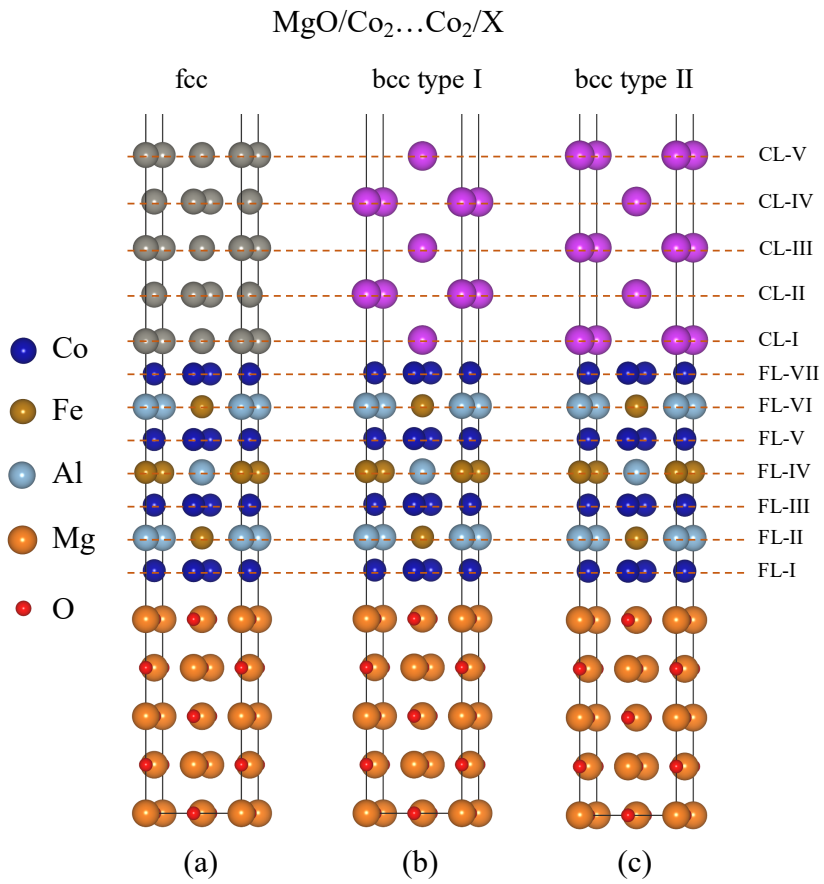

Figure 3.11: Schematic crystal structures of capped MgO/Co_2...Co_2 heterostructure with (a) FCC structure capping layer, (b) BCC type I structure capping layer, and (c) BCC type II structure capping layer.

resulting relatively weak bond strength, while the highly uniform interfacial structure (equivalent Co-O bonds) at the MgO/Co_2 interface leads to relatively high cleavage energy. Note that the unmatched bond strength between Fe-O and Al-O bonds can also be proven from the Bader charge analysis for the interfacial O atoms.[161]

3.3.2 Capped MgO/Co_2FeAl

In this section, we studied the influence of adding capping layers on the interfacial magnetic anisotropy of MgO/Co_2FeAl. A total number of 26 metal elements including 3*d* (Ti, V, Cr, Mn, Fe, Ni, and Cu), 4*d* (Zr, Nb, Mo, Tc, Ru, Rh, Pd, and Ag), 5*d* (Hf, Ta, W, Re, Os, Ir, Pt,

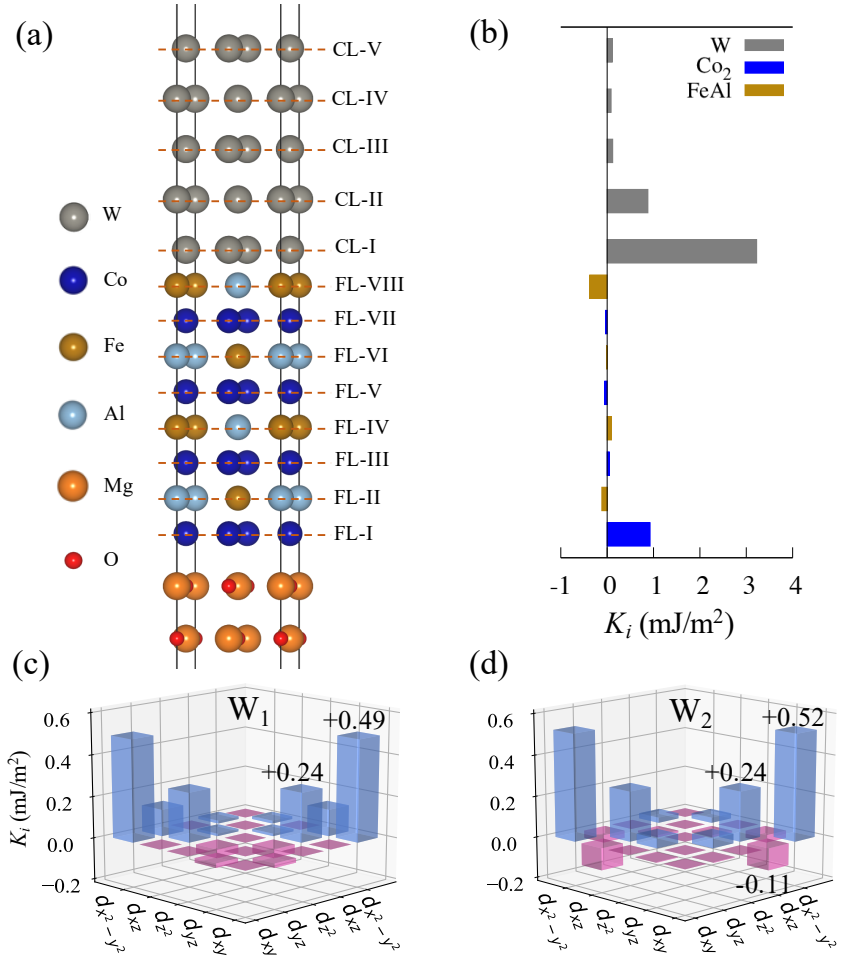

Figure 3.12: (a) Schematic crystal structure of W-capped MgO/Co_2...FeAl (MgO/Co_2...FeAl/W) (b) layer-resolved K_i value of MgO/Co_2...FeAl/W (c) and (d) K_i contributions from different d orbital hybridizations at the interfacial atoms of W1 and W2 of MgO/Co_2...FeAl/W.

Table 3.2: Summary of total K_i values of selected capping elements with lattice mismatch (f) smaller than 7%. The lattice mismatch is defined as $f = (a_f - a_s)/a_s$, where a_s and a_f are the lattice constant of substrate and film, respectively.

X	f(%)	K_i (mJ/m^2)	
		MgO/Co_2...FeAl/X	MgO/Co_2...Co_2/X
Ti	-2.5	0.71	1.00
V	0.4	0.98	0.87
Cr	-4.4	1.20	1.22
Mn	-6.1	0.73	0.48
Fe	-4.4	2.59	2.13
Ni	-6.4	-0.37	1.79
Cu	-3.6	1.21	1.22
Nb	0.4	0.58	1.18
Mo	-4.8	1.37	0.93
Pd	-6.2	1.86	0.60
Ag	-1.3	1.15	1.23
Hf	6.3	1.67	0.93
Ta	0.3	-0.72	0.63
W	6.2	4.90	2.46
Re	-6.9	0.27	-1.63
Pt	-5.6	0.56	-1.37
Au	-1.0	1.82	1.33
Tl (I)	-6.0	-1.76	2.12
Tl (II)			2.14
Pb (I)	-5.0	-0.35	2.01
Pb (II)			2.29
Bi (I)	-5.4	0.40	0.13
Bi (II)			2.08

and Au) TMs, and 6p (Tl, Pb, and Bi) metals were considered as capping layers. This is based on the consideration that these elements have a relatively large spin-orbit coupling (SOC) interaction that is likely to be capable of tuning the interfacial magnetic anisotropy.[13] The Co element is not included due to the large lattice mismatch between FCC-Co and MgO substrate ($\sim$16 %). Since our calculations show that the MgO/Co_2 interface is energetically more favorable than the MgO/FeAl interface, here we only considered MgO/Co_2...FeAl and MgO/Co_2...Co_2 models. We built the capped-MgO/Co_2FeAl by adding the FCC-type or BCC-type structures of these metal elements on top of the Co_2FeAl film while maintaining the thickness of vacuum around 15 Å,

Table 3.3: Summary of total K_i for all the capped MgO/Co_2FeAl. MCFX, MCCX, MFCX, and MFFX represent the model of MgO/Co_2...FeAl/X, MgO/Co_2...Co_2/X, MgO/FeAl...Co_2/X, and MgO/FeAl...FeAl/X,respectively.⊡: FCC structure, ⊞ : BCC structure

X	Lattice mismatch(%)	K_i (mJ/m^2)			
		MCFX	MCCX	MFCX	MFFX
Uncapped	-	0.60	1.28	0.12	-1.13
Ti⊡	-2.5	0.71	1.00	0.59	0.26
V⊞	0.4	0.98	0.87	0.53	0.61
Cr⊞	-4.4	1.20	1.22	0.92	0.47
Mn⊞	-6.1	0.73	0.48	1.39	1.44
Fe⊞	-4.4	2.59	2.13	5.72	5.49
Ni⊞	-6.4	-0.37	1.79	0.53	0.52
Cu⊞	-3.6	1.21	1.22	0.19	0.87
Zr⊡	7.6	1.33	1.40	-1.03	-0.62
Nb⊡	0.4	0.58	1.18	-0.80	-1.19
Mo⊡	-4.8	1.37	0.93	-1.16	-0.31
Tc⊡	-7.8	1.03	1.13	-0.17	-0.54
Ru⊡	-9.3	-3.26	1.07	-0.89	-5.67
Rh⊡	-8.8	-2.54	-1.39	-3.17	0.28
Pd⊡	-6.2	1.86	0.60	-0.31	-1.73
Ag⊡	-1.3	1.15	1.23	-0.59	-0.49
Hf⊡	6.3	1.67	0.93	-0.81	-0.36
Ta⊡	0.3	-0.72	0.63	-1.36	-3.26
W⊞	6.2	4.90	2.46	-1.57	2.16
Re⊡	-6.9	0.27	-1.63	-3.60	-0.67
Os⊡	-8.4	-0.13	0.30	-1.05	-1.04
Ir⊡	-8.0	-1.33	0.93	-0.94	-1.93
Pt⊡	-5.6	0.56	-1.37	-2.43	-2.75
Au⊡	-1.0	1.82	1.33	-0.08	-0.31
Bi⊞ (I)	-5.4	0.40	0.13	-1.39	-1.04
Bi⊞ (II)			2.08	2.69	
Pb⊞ (I)	-5.0	-0.35	2.01	-0.24	-0.42
Pb⊞ (II)			2.29	0.54	
Tl⊞ (I)	-6.0	-1.76	2.12	-0.28	-0.53
Tl⊞ (II)			2.14	-0.24	

see Fig. 3.11. It is noted that, for the MgO/Co_2...Co_2 model, there are two types of interfacial structures between Co_2FeAl film and BCC-type capping layer (including Tl, Pb, and Bi), and one type of interfacial structure between the Co_2FeAl film and FCC-type capping layer, as shown in the schematic crystal structures in Fig. 3.11. The layers of capping elemental compound are labeled as CL-I, CL-II, CL-III, CL-IV, and CL-V, respectively. In the case of V-, Cr-, Mn-, Fe-, Ni-, Cu-, and W-capped structures, to produce the best lattice match, a 45° rotation along [001] direction was made on the conventional bulk structure of BCC-type V, Cr, Mn, Fe, Ni, Cu, and W, leading to only one type of interfacial structure. By taking W-capped MgO/Co_2FeAl as one example, we also studied the total K_i as a function of the number of capping layers, as shown in the Fig. 3.5. Our calculations show that the K_i of the system with an odd number of capping layers (3, 5, and 7) is generally larger than that with an even number (4 and 6), and in spite of this, the K_i still tends to be saturated as the number of capping layers is larger than five.

Table 3.2 shows the summary of K_i values of selected capped MgO/Co_2FeAl systems that have a lattice mismatch (between Co_2FeAl and capping elemental bulk structure) less than 7%. The detailed results of all the 26 capped models are shown in the Table 3.3. It shows that Fe-, Mo-, Pd-, Hf-, W-, and Au-capped MgO/Co_2...FeAl structures show a larger K_i of 2.59, 1.37, 1.86, 1.67, 4.90, and 1.82 mJ/m^2 than the uncapped structure. The Tl-, Pb-, and Bi-capped MgO/Co_2FeAl structures with a type II structure also exhibit a large K_i of 2.14, 2.29, and 2.08 mJ/m^2. It is especially worth mentioning that W capping leads to a giant K_i value of 4.90 mJ/m^2 in MgO/Co_2...FeAl/W structure and a K_i of 2.46 mJ/m^2 in the MgO/Co_2...Co_2/W structure. Interestingly, prior experimental and computational studies indicated that W can also improve K_i in the Fe/W/MgO[13, 162] and MgO/CoFeB/W/CoFeB/MgO[163] systems in which a thin W interface layer was inserted as doping. Additionally, our calculation for MgO/Co_2...Co_2/Ta yield a K_i value of 0.63 mJ/m^2, which is in good agreement with the experimental value of 0.67 mJ/m^2.[144] To elucidate the origin of the giant K_i in MgO/Co_2...FeAl/W structure, we calculated its layer-resolved K_i and atomic orbital-resolved K_i in Fig. 3.12. It clearly shows that the large K_i

of MgO/Co_2...FeAl/W is mainly contributed by the interfacial W atoms at the CL-I (3.22 mJ/m^2) and CL-II (0.88 mJ/m^2) layers. The K_i from the interfacial Co atoms of Co_2FeAl is almost the same with that in the uncapped MgO/Co_2FeAl model, suggesting that the W capping layers has no significant influence on the magnetic anisotropy of the Co_2FeAl film but does enhance the total K_i of the MgO/Co_2...FeAl/W system. The orbital-resolved K_i of the two interfacial W atoms at CL-I layer were plotted in Fig. 3.12c and 3.12d. It shows that the out-of-plane K_i largely comes from the d orbital hybridization between $d_{x^2-y^2}$ and d_{xy} (around 0.50 mJ/m^2), and between d_{xz} and d_{yz} (0.24 mJ/m^2) in both W atoms.

3.4 Conclusion

In conclusion, we have systematically investigated the interfacial magnetic and energetic properties in the MgO/Co_2FeAl heterostructure by modeling four types of interfacial models using first-principles calculations. Our results show that MgO/Co_2 interface can produce out-of-plane K_i while MgO/FeAl interface can produce in-plane K_i, and the former interface is energetically more favorable than the later one and thus is likely to be formed practically. The calculated K_i of 1.28 mJ/m^2 in the MgO/Co_2...Co_2 structure is well consistent with the experimental value. In addition, the influence of 26 capping layers on the interfacial magnetic anisotropy was explored. It is found that Fe- and W-capping can significantly enhance the interfacial K_i in the MgO/Co_2FeAl, and particularly, a giant K_i of 4.90 mJ/m^2 can be achieved in the W-capped model. This work reveals the atomistic origin of the large perpendicular magnetic anisotropy at MgO/CO_2FeAl interface and offers insights to tune interfacial K_i via adding capping layers in the MgO/Co_2FeAl.

3.5 Acknowledgement

Chapter 3, in full, is a reprint of the material “Origin of the large interfacial perpendicular magnetic anisotropy in MgO/Co_2FeAl” as it appears in Physical Review B, Sicong Jiang, Safdar Nazir, Kesong Yang, 101, 134405, 2020. The dissertation author was the primary investigator and author of this paper.

Chapter 4

Accelerate the Discovery of Quaternary Heusler Materials for Perpendicular Magnetic Tunnel Junctions via High-throughput first-principle Calculations

In chapter 2 and 3, we concentrated on the screening and understanding of PMA of ternary Heusler/MgO based structures. In this chapter, we further extended our investigations to the quaternary Heusler compounds, which offer much larger compositional space for tuning materials properties. In addition to the descriptors mentioned in chapter 2, we also considered the phase stability of quaternary compounds by studying the competing phases including space group #129, and #215. 7 out of 3094 stable quaternary Heusler compounds were found feasible for future applications in the p-MTJs. The origin of the PMA in these quaternary Heusler/MgO heterostructures was further analyzed by the layer-resolved and atomic-orbital-resolved K_i distributions. This

work demonstrates an effective method to accelerate the discovery of novel quaternary Heusler based functional materials interfaces by means of high-throughput DFT calculations with efficient materials descriptors and large open quantum materials repositories.

4.1 Introduction

To date, magnetic tunnel junctions (MTJs) with a core structure of two ferromagnetic (FM) layers separated by a thin insulating tunnel barrier have attracted great interest due to their wide applications in the memory recording devices such as magnetic random-access memories (MRAMs)[1, 2, 3, 4, 5]. As one of the critical building blocks in the filed of spintronics, MTJs also have potentials in the next-generation computing schemes, such as quantum computing[85, 86, 164]. In spite of their promising usage, the traditional MTJs with in-plane magnetic anisotropy can suffer from issues of low thermal stability, high switching current, and slow reversal speed. Nevertheless, these challenges can be gradually overcome when it turns to the perpendicular MTJs (p-MTJs) with perpendicular magnetic anisotropy (PMA)[6, 7]. The strength of the anisotropy in MTJs can be characterized by the magnetic anisotropy per unit area (K_i), where in p-MTJs the large positive K_i is desired to counteract the demagnetization energy and maintain a sufficient thermal stability as the size of the building blocks shrink to the nanoscale[1, 8].

PMA has been traditionally found in materials interfaces between magnetic Co layers and heavy nonmagnetic layers with strong spin-orbit coupling (SOC) interactions,*e.g.*, Co/Pt, Co/Pd, and Co/Au, though the K_i value is less than 1.0 mJ/m^2[165, 93, 166, 94]. In addition, PMA has also been observed in ferromagnetic thin films without strong SOC, such as Co[95]. In 2010, Ikeda et al. successfully synthesized p-MTJ Ta/CoFeB/MgO/CoFeB/Ta with a large K_i of 1.3 mJ/m^2, high TMR ratio of 120 %, and a low switching current of about 49 μA at the same time.[9] Since then, great efforts have been made to search for alternative novel materials interfaces with different ferromagnetic layer and insulating tunnel barrier, such

as Co_2FeAl/MgO [14, 102], Mn_3Ga/MgO[91], MgO/Co(111)[103, 104], Fe/$MgAl_2O_4$[105], Co_2FeAl/$NiFe_2O_4$[106], Fe/$CuInSe_2$[107], NiFeB/MgO[167], to optimize the desired properties, e.g., high thermal stability, high spin polarization, low damping constant, high TMR ratio.

Among all the materials interfaces that have been invested, Heusler alloys based heterostructure are promising candidates for p-MTJs due to their fascinating properties.[17, 18, 19, 20, 21, 22, 23] In addition, Heusler alloy is a large family of intermetallic compounds with more than 1500 compositions.[36, 37] The tunable compositions in Heusler compounds afford the best play ground for novel materials design and screening. In particular, compared to the ternary Heusler compounds (X_2YZ or XYZ) with only three elements, quaternary Heusler compounds $XX'YZ$ with four elements leads to much larger composition space[109, 168]. Previous high-throughput materials design of quaternary Heusler compounds mainly concentrate on the thermoelectric properties[84] and spin-gapless semiconductors[53, 169]. However, their feasibility of applications in developing novel materials interface for next-generation spintronic devices remains unknown. Therefore, it is indispensable to perform a high-throughput computational design of quaternary Heusler alloy based p-MTJs via first-principle calculations to provide enlightening guidance to both theoretical and experimental research in the future.

In this paper, we presented a systematical high-throughput screening of quaternary Heusler compounds to search for feasible materials interfaces for the application of p-MTJs with long retention time and low switching current. After a careful screening with a series of effective descriptors, seven quaternary Heusler based materials interfaces with PMA were selected in our final list. The origin of the PMA in the MgO/quaternary Heusler heterostructures was further analyzed by the layer-resolved and atomic-orbital-resolved K_i distributions. Notably, a significantly large K_i of 5.00 mJ/m^2 were found in the heterostructure model of MgO/IrMnZnTi. This work demonstrates an effective way to accelerate the discovery of quaternary Heusler materials and open up possibilities for the functional materials interface by employing effective materials descriptors on the basis of high-throughput calculations and large open quantum

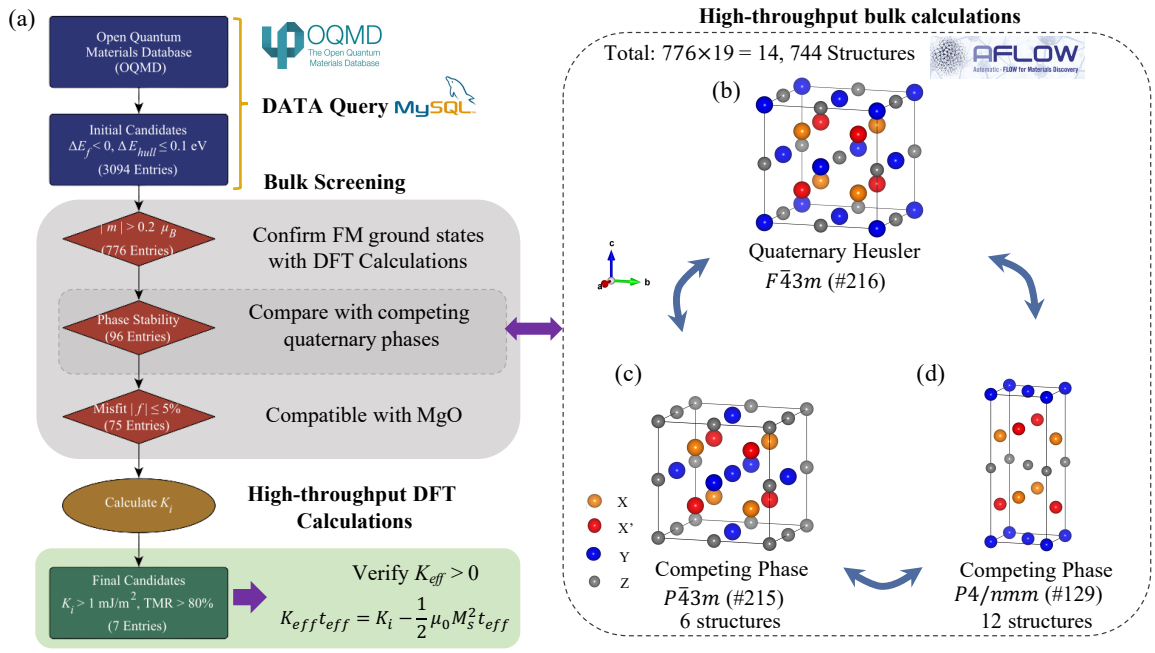

Figure 4.1: Schematic workflow of high-throughput screening of bulk Heusler compounds for the application of p-MTJs. A total number of 3094 Entries were initially selected from the Open Quantum Materials Database (OQMD) via the MySQL. Materials descriptors of formation energy (ΔE_f), convex hull distance (ΔE_{hull}), lattice mismatch with MgO, interfacial cleavage energy ($E_{cleav.}$), magnetic anisotropy constant (K_i), and tunnel magnetoresistance ratio (TMR) were considered for the screening process (a). Schematic representation of (b) Quaternary Heusler compounds with space group of $F\bar{4}3m$ (#216), (c) and (d) competing quaternary phases with space of $P\bar{4}3m$(#215) and $P4/nmm$(#129), respectively.

materials repositories.

4.2 Methods

The automatic framework AFLOW[113] based on Vienna *Ab-initio* Simulation Package (VASP)[146] were performed for high-throughput density functional theory (DFT) calculations of bulk quaternary compounds. The projector augmented wave (PAW) pseudopotentials[114] were used for electron-ion interactions. The generalized gradient approximation (GGA) parameterized by Perdew-Burke-Ernzerhof (PBE) was used for exchange-correction functional[115]. A convergence threshold of 0.01 meV/atom was set for the structure relaxation. The k-points grid

of 0.05 $Å^{-1}$ and 0.04 $Å^{-1}$ were set for structural relaxation and static calculations, respectively. Other related computational settings including the cutoff energy were appropriately generated by the AFLOW code for both structural relaxation and static calculations[113]. In the heterostructure calculations, Γ-centered *k*-points grids were set to $8 \times 8 \times 1$ and $13 \times 13 \times 1$ for structural relaxation and static calculation, respectively. All the lattice parameters and atomic positions were fully relaxed until the residual forces were smaller than the threshold of 0.005 eV/Å. The electronic self-consistency loop including spin-orbit coupling (SOC) calculations were performed with a convergence threshold of 10^{-6} eV. The magnetic anisotropy constant K_i was calculated as $(E_{[100]} - E_{[001]})/(2A)$,[101] where $E_{[100]}$ ($E_{[001]}$) represents the total energy including SOC with magnetization along [100] ([001]) direction in a fully self-consistent-field manner. The factor of 2 in the denominator represents two symmetrical interfaces in the heterostructure model; A is the in-plane area.

4.3 Results and Discussion

Our high-throughput computational design can be mainly divided into three steps: (1)DATA Query, (2) Bulk Screening, and (3) Heterostructure Screening. The detailed workflow are shown in Figure 4.1.

4.3.1 DATA Query

As the first step, we queried the Open Quantum Materials Database (OQMD)[170] version 1.4 using the MySQL code. We choose the OQMD database because they can provide the data of convex hull distance (ΔE_{Hull}) for quaternary compounds, which serves as an important threshold in our screening process. A recent machine learning paper made it possible to predict the convex hull distance based on thousands of DFT calculations of formation energy in the OQMD database[54]. The formation energy ΔE_f of quaternary Heusler can be defined as $\Delta E_f = E_{XX'YZ}$ -

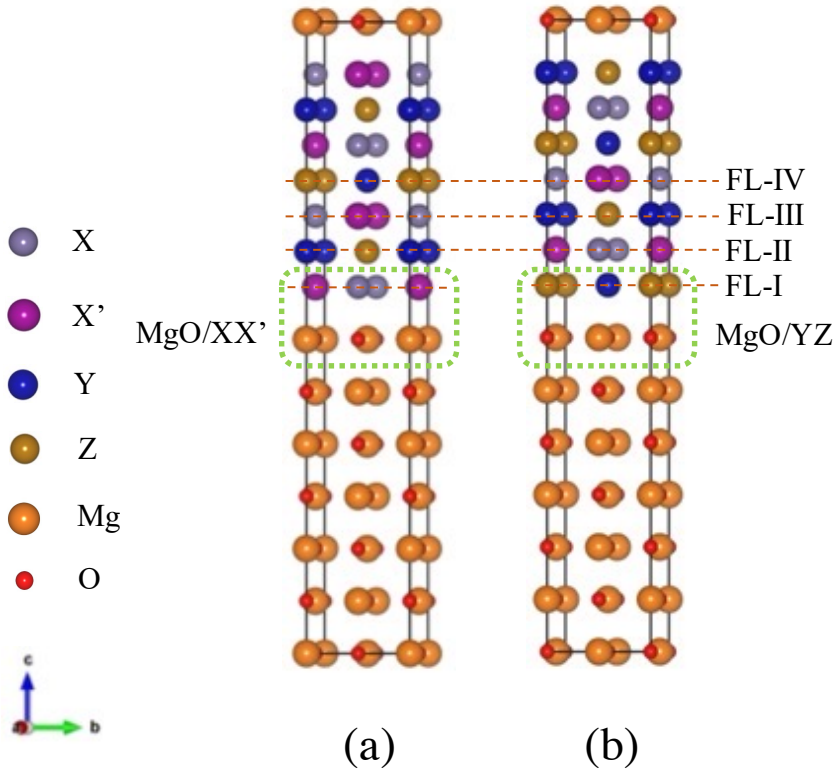

Figure 4.2: Illustration of the heterostructure models for (a) MgO/XX' and (b) MgO/YZ interfaces. The MgO substrate and quaternary Heusler film were both set as seven layers.The FL-I, FL-II, FL-III, and FL-IV represents the first, second, third, and fourth layer from the MgO/quaternary Heusler interface, respectively.

($E_X + E_{X'} + E_Y + E_Z$), where $E_{XX'YZ}$, E_X, $E_{X'}$, E_Y and E_Z are the total energy for the compound $XX'YZ$ and for the bulk X, X', Y, and Z single element ground-state phase, respectively. A negative ΔE_f reveals that at 0K the compound is stable against its constituent element. The ΔE_{Hull} can be described as $\Delta E_{Hull} = \Delta E_f$ - E_h, where ΔE_f is the formation energy and E_h is the convex hull energy of the compound[58]. The ΔE_{Hull} can reflect the thermodynamic stability of a compound against its competing phases, including binary and ternary phases. The threshold of ΔE_{Hull} can be set as high as 0.1 eV/atom[53]. More strict value of 0.03-0.05 eV/atom were also used in previous high-throughput papers[62, 61]. In our DATA query step, we selected 3094 entries based on two criteria: $\Delta E_f < 0$ and $\Delta E_{hull} \leqslant 0.1$ eV from the OQMD database.

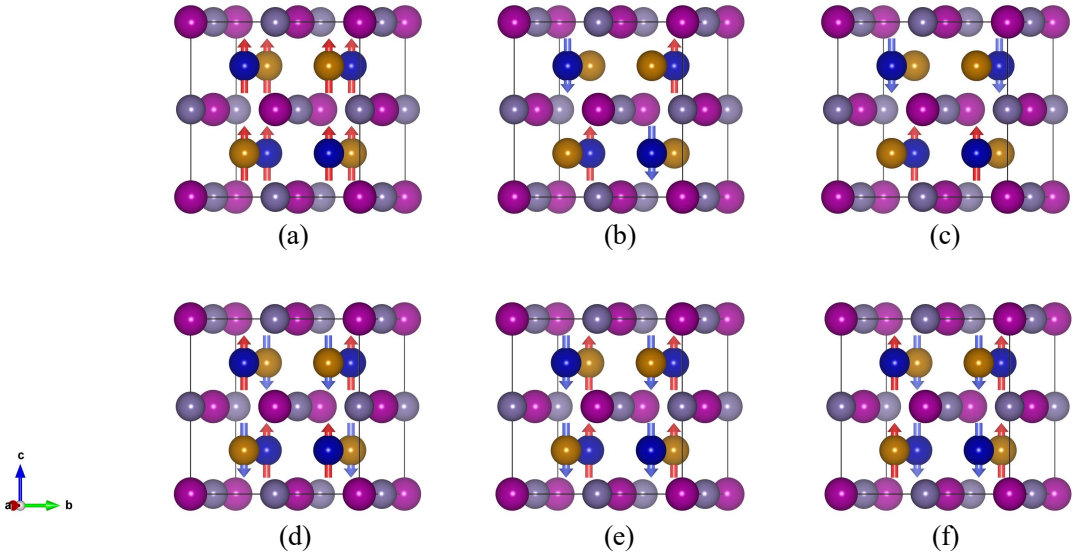

Figure 4.3: (a) Possible FM configuration of quaternary Heusler if two atoms are magnetic. Possible AFM or FI configuration of quaternary Heusler if one atom is magnetic (b-c) or two atoms (d-f) are magnetic, respectively.

4.3.2 Bulk Screening

(i) Magnetic structure: In the DATA query step, we selected 3094 thermodynamically stable compounds. However, most of the compounds we selected in the previous step are non-magnetic and are not suitable for the application of p-MTJs. By using the descriptor of spin magnetic moment m, we found 776 out of 3094 entries with $|m| > 0.2\ \mu B$/f.u.. Since the OQMD database only provide data for ferromagnetic (FM) configurations, we further considered the ferrimagnetic (FI) and antiferromagnetic (AFM) configurations of these 776 compounds. The magnetic configurations of FM, FI, and AFM of these 776 entries were calculated by our high-throughput DFT calculations with the AFLOW code. The detailed magnetic structure configurations were shown in the Figure 4.3. In General, for the AFM and FI structures, we not only consider the opposite spin magnetic moment between different elements but also considered the opposite spin magnetic moment in the same element of different atoms. After this step, 484 compounds were confirmed with FM ground states, 80 compounds were confirmed with FI

Table 4.1: Summary of candidate quaternary Heusler compounds with descriptors: $\Delta E_H \leqslant 0.1$, $-5\% \leqslant f \leqslant 5\%$, and $K_i \geqslant 0.5$ for at least one termination. The ΔE_{Hull} (eV/atom) and f refer to the convex hall distance and the lattice lattice misfit with MgO substrate, respectively. The K_i (mJ/m^2), $E_{cleav.}$ (meV/Å^2), P_f, and TMR (%) indicate magnetic anisotropy constant, cleavage energy, spin polarization, and tunnel magnetoresistance, respectively.

Compounds	ΔE_{Hull}	f (%)	K_i		$E_{cleav.}$		P_f		TMR	
			XX'	YZ	XX'	YZ	XX'	YZ	XX'	YZ
AlTiOsMn$^{\odot}$	0.020	1.4	0.58	1.76	87.19	104.41		0.68		170
GeMnCoFe*	0.013	-4.3	0.16	0.71	48.81	109.99				
IrCrAlTi$^{\odot}$	0.045	2.2	1.77	0.43	102.20	81.55	0.69		184	
IrCrGaTi$^{\odot}$	0.039	2.2	1.45	0.15	100.06	66.15	0.68		173	
IrMnZnTi$^{\odot}$	0.083	1.6	5.00	0.77	79.37	76.05	0.63		135	
MnGaPtFe	0.078	0.2	-0.68	3.89	50.29	70.67		0.46		52
OsCoAlCr	0.062	-1.6	0.01	2.24	126.41	87.11				
OsCrAlNb	0.051	3.8	1.84	0.41	115.84	68.82	0.51		71	
OsCrAlTa$^{\odot}$	0.058	3.7	1.68	-0.53	115.95	74.18	0.63		130	
OsCrAlTi	0.019	2.6	0.02	1.16	117.21	86.73				
OsCrAlV$^{\diamond\odot}$	0.054	0.6	1.68	-0.08	118.53	96.24	0.58		101	
OsCrGaNb	0.071	3.9	2.05	0.96	114.21	57.80	0.53		79	
OsCrGaTi	0.088	2.7	0.37	0.88	117.58	67.92				
OsCrZnNb	0.090	4.1	-0.02	0.87	116.37	69.92				
OsCrZnTa	0.083	4.0	-0.65	0.60	116.26	75.69				
RuMnGaSc	0.079	4.6	0.63	0.83	86.78	46.69				
TaGaOsCr$^{\odot}$	0.085	3.8	0.73	1.40	64.50	114.07		0.62		125
TiZnIrCr	0.049	2.5	0.95	-0.46	76.91	104.35				
VGaOsCr$^{\diamond}$	0.077	0.8	-0.28	1.88	73.92	118.64		0.51		69

$\diamond$ indicates bulk compounds with FI ground state, $\odot$ represents the target quaternary Heusler after screening, and $*$ shows the experimentally synthesized compound.

ground states, and 202 compounds were confirmed with AFM ground states, see the details in Table A.3 of the appendix.

(ii) Phase stability: As was shown in Figure 4.1 b, the conventional quaternary Heusler structure has a space group of $F\bar{4}3m$ (#216), where X and X' atoms occupy the Wyckoff positions 4*c* (1/4, 1/4, 1/4) and 4*d* (3/4, 3/4, 3/4), respectively, and Y and Z atoms occupy 4*a* (0, 0, 0) and 4*b* (1/2, 1/2, 1/2), respectively. Accordingly, for a given composition without positions of each atom, there are three unique materials structures due to their space group symmetry[168], see detailed structures in Figure 4.4. Due to the limit data points of quaternary phases in the current quantum

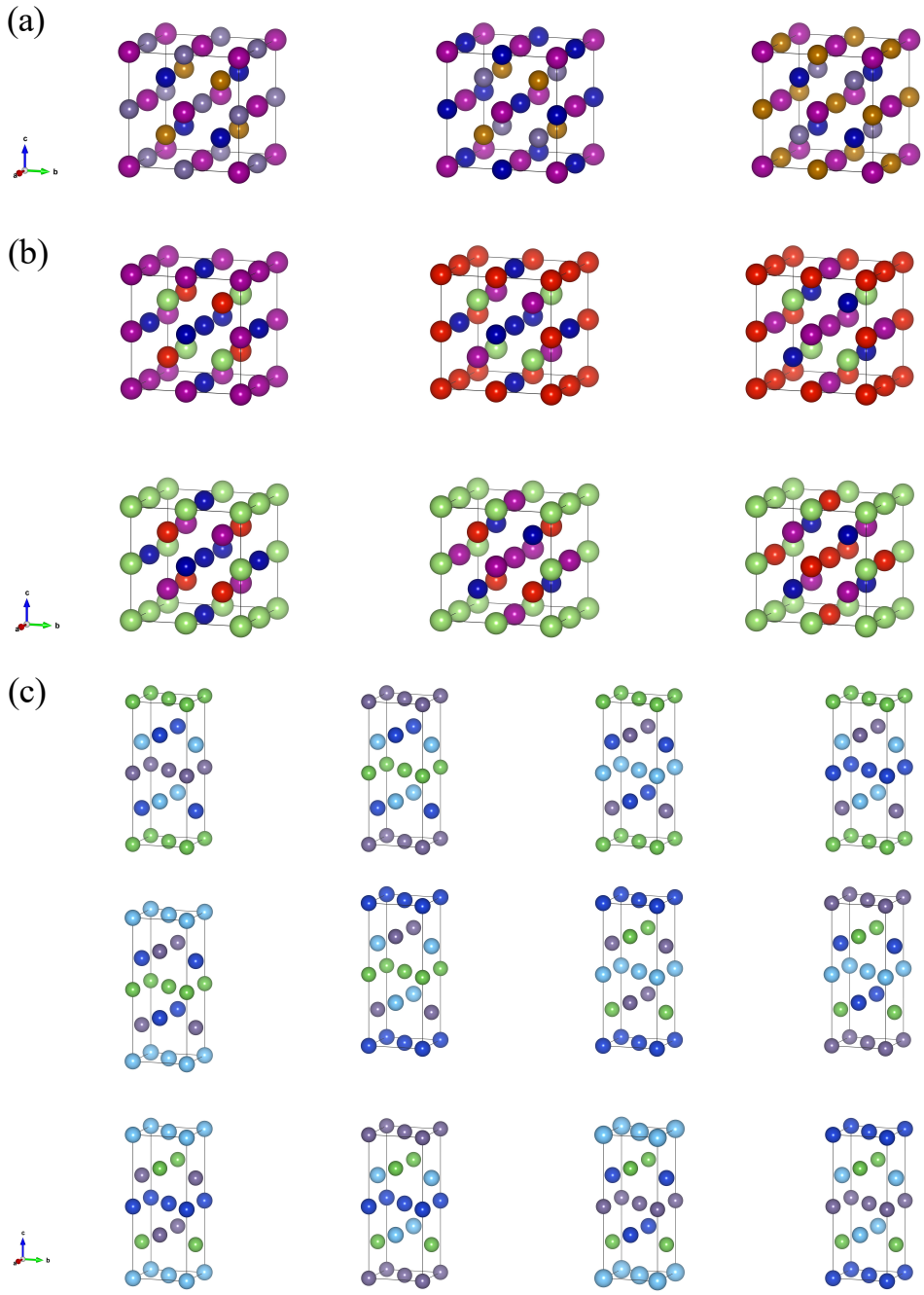

Figure 4.4: Schematic crystal structure of (a) 3 unique structures of quaternary Heusler compound with space group $P\bar{4}3m$(#216) (b) 6 unique structures of quaternary compound with space group $P\bar{4}3m$(#215) (c) 12 unique structures of quaternary compound with space group $P4/nmm$(#129).

materials repositories, the ΔE_{Hull} can only be calculated based on ternary, binary and limited data points of quaternary phases. Therefore, we further investigated the phase stability of 776 entries from our previous step, by considering two extra quaternary competing phases, including space group $P\bar{4}3m$(#215) and $P4/nmm$(#129), see Figure 4.1c and 4.1d, respectively. According to the symmetry of their space group, $P\bar{4}3m$(#215) has 6 unique structures and $P4/nmm$(#129) has 12 unique structures for a given composition without positions of each atom. We showed the detailed schematic crystal structure of these 19 structures (1 quaternary Heusler structure and 18 competing structures) in Figure 4.4. Next, we did a high-throughput bulk calculations for these 14, 744 structures (776 $\times$ 19). Noted that, if the total energy of the structure is 25 meV/atom lower than its competing structures, we considered it as the stable structure of that composition. By using the 25 meV/atom criterion, 96 compositions were confirmed with stable quaternary Heusler structures, 21 compositions were confirmed with stable $P\bar{4}3m$(#215) structures, 44 compositions were confirmed with stable $P4/nmm$(#129) structures.

(iii) Lattice misfit (f): We calculated the the lattice misfit between the bulk quaternary Heusler and the MgO substrate with the following formula: $f = (a_f - a_s)/a_s$, where a_f and a_s are the lattice constants of film and substrate, respectively. The sign of f represents the strain of quaternary Heusler film undergoes from the MgO substrate, where positive sign indicates compression and negative sign reveals tension. It is generally considered that a relatively large misfit between the film and substrate can increase the strain in the film layer and make it unstable and less likely to grow on the substrate. Accordingly, in this work, we selected compounds with $|f| \leqslant 5\%$ based on our previous empirical experience[122, 171]. After this step, 75 quaternary compounds were confirmed as FM or FI stable and were suitable to build up heterostructure models with MgO as the substrate.

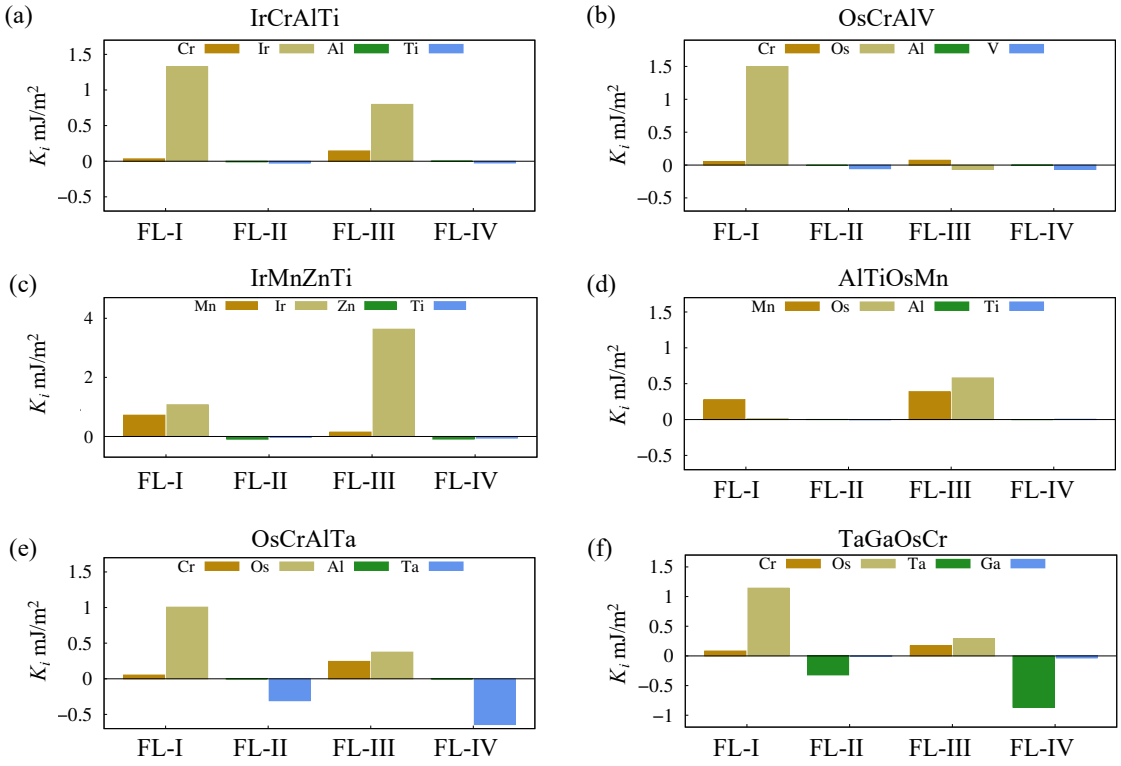

Figure 4.5: Calculated layer-resolved K_i values for (a) MgO/IrCrAlTi with CrIr as interface (b) MgO/OsCrAlV with CrOs as interface (c) MgO/IrMnZnTi with IrMn as interface (d) MgO/AlTiOsMn with MnOs as interface (e) MgO/OsCrAlTa with CrOs as interface (f) MgO/TaGaOsCr with CrOs as interface. Labels FL-I, FL-II, FL-III, and FL-IV correspond to the first, second, third and third quaternary Heusler film layers from the MgO/quaternary Heusler interface.

4.3.3 Heterostructure Screening

(i) Magnetic Anisotropy (K_i): We build up our heterostructure model with seven layers of quaternary Heusler film and seven layers of MgO substrate to represent MgO-based MTJs in experiments. Previous calculations have proved that seven layers of MgO substrate are enough to converge the magnetic anisotropy[16, 101]. To match the lattice parameter of MgO substrate of 4.215 Å, 45° rotation was made along the [001] direction of the bulk structure of conventional quaternary Heusler. In general, there are two symmetric types of heterostructures, MgO/XX' and MgO/YZ, where their schematic crystal structures were shown in Figure 4.2a and 4.2b, respectively. Before we built up the heterostructures, 34 out of 75 compounds contain Li, Be, and

Tc, which are not suitable for our applications, were removed from our list. Accordingly, we calculated the magnetic anisotropy K_i for both MgO/XX' and MgO/YZ models for the remaining 41 bulk candidates. Table 4.1 shows the calculated results for the 19 selected candidates, where in these candidates at least one interface model has K_i larger than 0.5 mJ/m^2. Noted that compound GeMnCoFe has been successfully synthesized by experiments[172]. In the heterostructures of MgO/AlTiOsMn, MgO/IrMnZnTi, MgO/OsCrGaNb, and MgO/TaGaOsCr both terminations have PMA and at least one interface model has a K_i larger than 1 mJ/m^2. Meanwhile, in the case of MgO/IrMnZnTi and MgO/MnGaPtFe, compared to the K_i of 1.2-2.1 mJ/m^2 in the MgO/Fe system[11, 12, 13], a much larger K_i of 5.00 mJ/m^2 and 3.89 mJ/m^2, were calculated for IrMn and PtGe termination, respectively.

(ii) Cleavage Energy ($E_{cleav.}$): Since we have two models for each candidate, we further analyzed the interface stability by using the cleavage energy to determine the most stable interface model. The cleavage energy of MgO/quaternary Heusler heterostructure can be defined as:

$$E_{cleav.} = (E_{slab}^{XX'YZ} + E_{slab}^{MgO} - E_{HS}^{MgO/XX'YZ})/(2A), \tag{4.1}$$

where $E_{slab}^{XX'YZ}$, E_{slab}^{MgO}, and$E_{HS}^{MgO/XX'YZ}$ are the total energy of $XX'YZ$ slab, MgO slab, and MgO/$XX'YZ$ heterostructure, respectively. A is the in-plane interfacial area; the factor 2 in the denominator indicates two symmetrical interfaces in the model. Interfaces with relatively large $E_{cleav.}$ ($>$ 15 meV/Å^2) are tend to be more stable that those with smaller $E_{cleav.}$. If two interfaces have close $E_{cleav.}$, both interfaces are feasible depending on the experimental techniques. In particular, considering the $E_{cleav.}$, the interface models with PMA for compounds OsCoAlCr, OsCrAlTi, OsCrZnNb, OsCrZnTa, and TiZnIrCr are not stable. Therefore, we removed these compounds from our final list.

(iii) Spin polarization (P_f): We estimated the spin polarization (P_f) for heterostructures

with $K_i > 1$ mJ/m^2 in the most stable interface model using the following equations[126]:

$$P_f = \frac{\mathcal{D}_+(E_\mathrm{F}) - \mathcal{D}_-(E_\mathrm{F})}{\mathcal{D}_+(E_\mathrm{F}) + \mathcal{D}_-(E_\mathrm{F})}, \tag{4.2}$$

where $\mathcal{D}_+(E_\mathrm{F})$ and $\mathcal{D}_-(E_\mathrm{F})$ are the DOS for majority and minority channels at Fermi level, respectively.

(iv) TMR ratio: The TMR ratio of the corresponding models were calculated with the Julliere's euqation[127]:

$$\mathrm{TMR} = \frac{2P_1P_2}{1 - P_1P_2}, \tag{4.3}$$

where P_1 and P_2 are spin polarization of the two FM or FI electrodes calculated in (iii). In the TMR ratio calculation of Heusler/MgO/Heusler MTJs models, we assumed that the two electrodes consist of the same quaternary Heusler compound leading to $P_1 = P_2 = P_f$. Notably, compound MnGaPtFe, OsCrAlNb, OsCrGaNb, and VGaOsCr were removed from our final list due to the low spin polarization and low estimated TMR $< 80\%$.

(v) Effective magnetic anisotropy (K_{eff}): In the finite thin film, the shape anisotropy spontaneously favours in plane. Therefore, we calculated the effective magnetic anisotropy (K_{eff}) by considering the shape anisotropy (K_{shape}) to verify the robustness of PMA. The K_{eff} can be defined as[1]:

$$K_\mathrm{eff} = \frac{K_i}{t_\mathrm{eff}} - \frac{1}{2}\mu_0 M_s^2 \tag{4.4}$$

where $\frac{1}{2}\mu_0 M_s^2$ represents the shape anisotropy per unit volume, t_eff is the thickness of the FM or FI layer, μ_0 is the magnetic constant, and M_s is the saturation magnetization per unit volume. Table 4.2 shows the calculated K_{eff} for seven candidate systems in our final list. Considering the shape anisotropy, our calculations confirmed that all screened candidate systems have a positive K_{eff} revealing a robust PMA in our models.

Table 4.2: Summary of seven final candidate Heusler/MgO heterostructures with calculated properties: K_i (mJ/m^2), saturation magnetization M_s (emu/cm^3), shape anisotropy K_{shape} ($\times 10^7$erg/cm^3), and effective anisotropy per unit volume K_{eff} ($\times 10^7$erg/cm^3).

Compounds	Interface	K_i	M_s	K_{shape}	K_{eff}
AlTiOsMn	OsMn	1.76	569	0.20	1.71
IrCrAlTi	IrCr	1.77	493	0.15	1.59
IrCrGaTi	IrCr	1.45	495	0.15	1.27
IrMnZnTi	IrMn	5.00	643	0.26	4.48
OsCrAlTa	OsCr	1.68	496	0.15	1.45
OsCrAlV	OsCr	1.68	515	0.17	1.53
TaGaOsCr	OsCr	1.40	545	0.19	1.26

By using the descriptors mentioned above, we screened the 75 quaternary Heusler based MgO heterostructures. The heterostructures with PMA should match with the interfaces with the larger cleavage energy. Meanwhile, the estimated TMR value of the p-MTJ with the corresponding MgO/quaternary Heusler interface should be larger than 80%. As was shown in Table 4.1, the heterostructure screening process gives us seven final candidates, including AsTiOsMn, IrCrAlTi, IrCrGaTi, IrMnZnTi, OsCrAlTa, OsCrAlV, TaGaOsCr.

It is noted that previous experimentally synthesized quaternary Heusler CoFeMnSi is not included in our list because of the large lattice misfit with MgO substrate [172]. Besides, our calculations show that the energy difference between the space group #216 phase and #215 phase is less than 15 meV/atom. Thus, the quaternary phase of CoFeMnSi may not be stable, which is also consistent with the reported DO_3 disordering in the literature[172, 173]. Previously theoretically predicted compounds FeCrTiAl[169] and experimentally reported compound CoRhMnGe [174] were screened in our list of 75 compounds, but not in our final list due to the in-plane magnetic anisotropy in the heterostructures. The compound CoFeCrGe were experimentally confirmed as the ordered phase[175], but our DFT calculations show that phase with space group #215 has the lowest total energy.

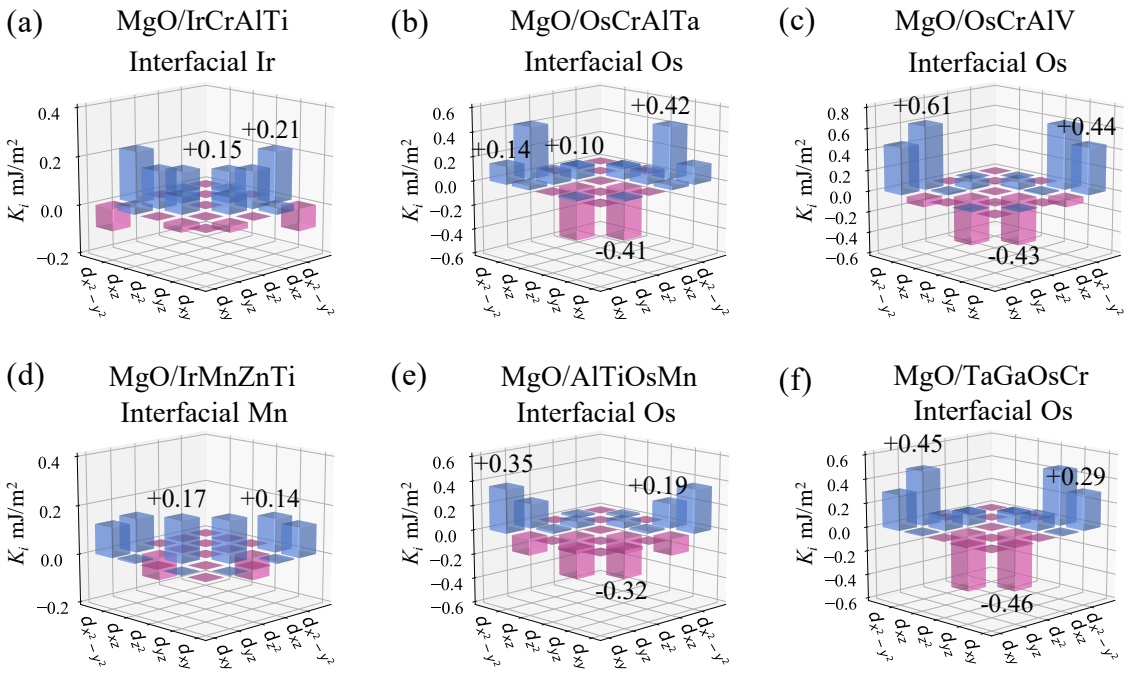

Figure 4.6: Calculated atomic-resolved K_i distribution from d-orbital hybridizations in selected six MgO/quaternary Heusler heterostructure models. (a-f) d-orbital hybridizations of interfacial Ir, Os, Os, Mn, Os, and Os atoms in the MgO/IrCrAlTi, MgO/OsCrAlTa, MgO/OsCrAlV, MgO/IrMnZnTi, MgO/AlTiOsMn, and MgO/TaGaOsCr, respectively

4.3.4 Origin of PMA

To understand the origin of PMA, we calculated the layer-resolved K_i distributions for our selected promising quaternary Heusler heterostructures, see Figure 4.5. Since the layer-resolved K_i distribution of MgO/IrCrAlTi and MgO/IrCrGaTi are similar, we only show the results of MgO/IrCrAlTi. As one can see that, in all cases, PMA mainly comes from the Ir, Os, and Mn atoms. In the case of MgO/IrCrAlTi and MgO/IrMnZnTi, the PMA results from the Ir atoms in the FL-I and FL-III layers, see figure 4.5a and 4.5c. Besides, the interfacial Mn atom in the FL-I layer also have positive contributions, while the other atoms barely contribute to the magnetic anisotropy. As is shown in figure 4.5b, 4.5e, and 4.5f, in the case of MgO/OsCrAlV, MgO/OsCrAlTa, MgO/TaGaOsCr, the PMA mainly attributes to the interfacial Os atoms in the FL-I layer. In addition, Mn or Cr atoms in the FL-I and FL-III layers also contribute to the PMA,

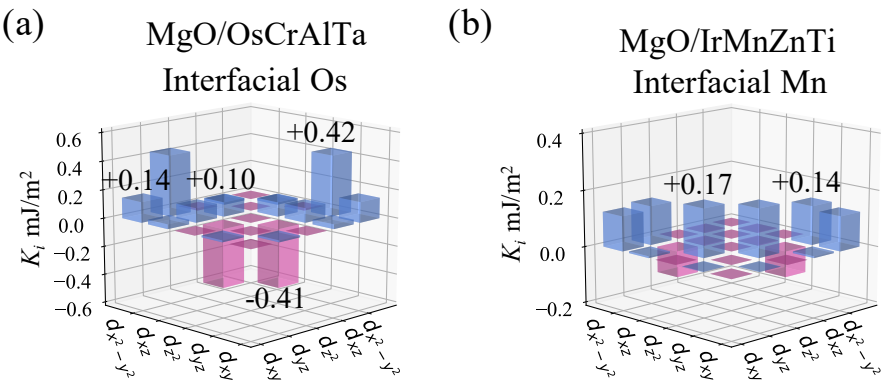

Figure 4.7: Calculated atomic-resolved K_i distribution from d-orbital hybridizations of (a) interfacial Os in the MgO/OsCrAlTa and (b) interfacial Mn in the MgO/IrMnZnTi.

while the Ta atoms in the FL-II and FL-IV layers result in the in-plane magnetic anisotropy. It is worth noting that in the case of MgO/AlTiOsMn, though the Os atom is in the FL-I layer, it barely has contributions to the magnetic anisotropy. Accordingly, the PMA comes from the interfacial Mn atom and the Os and Mn atoms in the FL-III layer.

To further understand the microscopic origin of the interfacial magnetic anisotropy, we calculated the orbital-resolved K_i for the atoms in the FL-I layer. Figure 4.6a shows the d-orbital hybridization of interfacial Ir atom in the MgO/IrCrAlTi model, where the PMA mainly attributes from the hybridization between d_{yz}, $d_{x^2-y^2}$, and d_{z^2}, around 0.21 mJ/m^2 and 0.15 mJ/m^2, respectively. In figure 4.6d, one can see that PMA of interfacial Mn in the MgO/IrMnZnTi heterostructure attributes from the hybridization bewteen d_{yz}, d_{z^2}, and $d_{x^2-y^2}$. In the case of MgO/OsCrAlTa, MgO/OsCrAlV, MgO/AlTiOsMn, and MgO/TaGaOsCr, d-orbital hybridization between $d_{x^2-y^2}$, d_{xy}, and d_{yz} of the interfacial Os atom show out-of-plane magnetic anisotropy, while in-plane magnetic anisotropy results from the hybridization between d_{z^2} and d_{yz}, see figure 4.6b, 4.6c, 4.6e, and 4.6f, respectively. Noted that the total K_i of interfacial Os atom in the MgO/AlTiOsMn is around zero, due to the cancellation between the out-of-plane and in-plane magnetic anisotropy, which is consistent with our results in figure 4.5d.

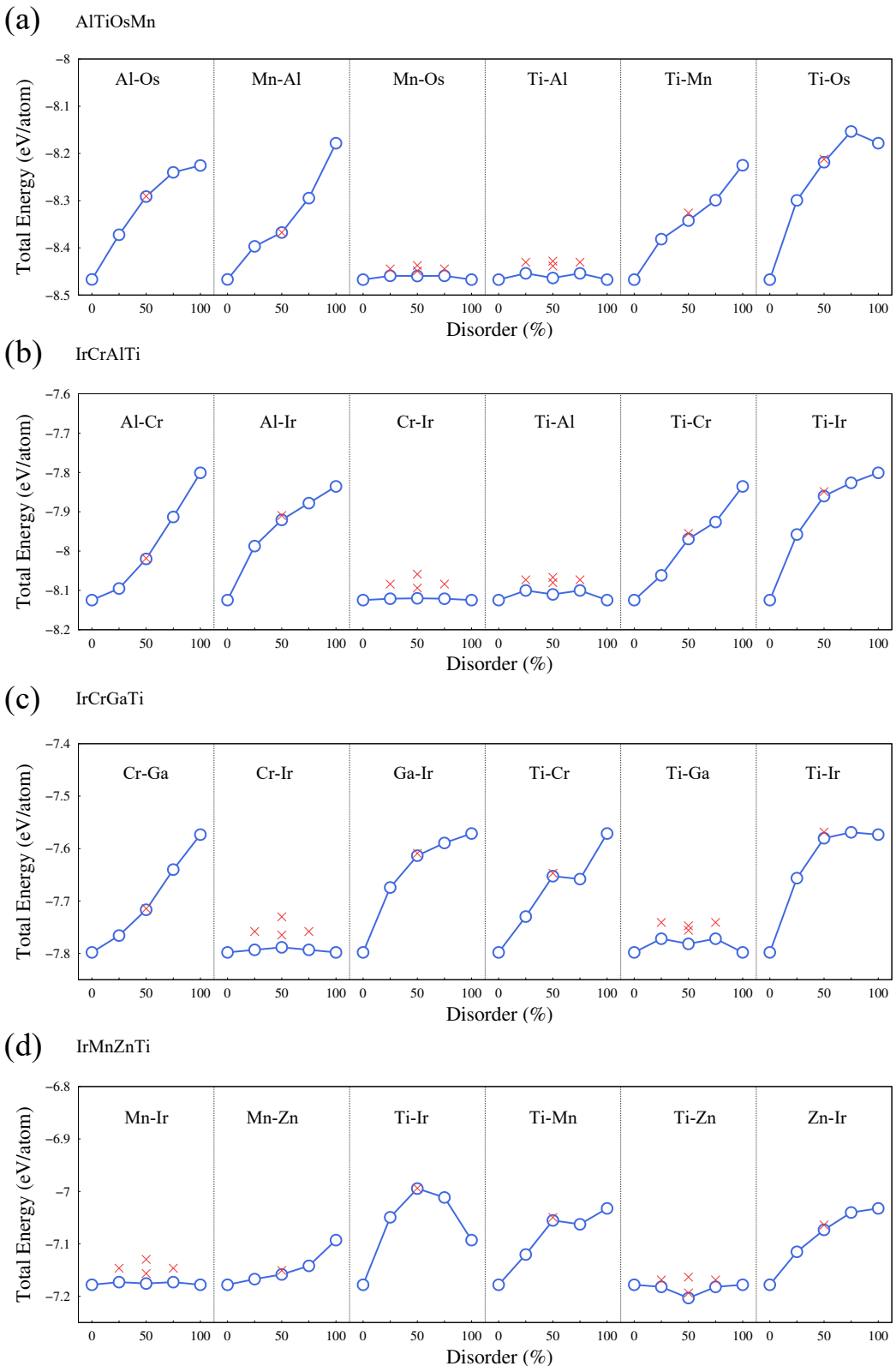

Figure 4.8: Disorder effects of (a) AlTiOsMn (b) IrCrAlTi (c) IrCrGaTi (d) IrMnZnTi.

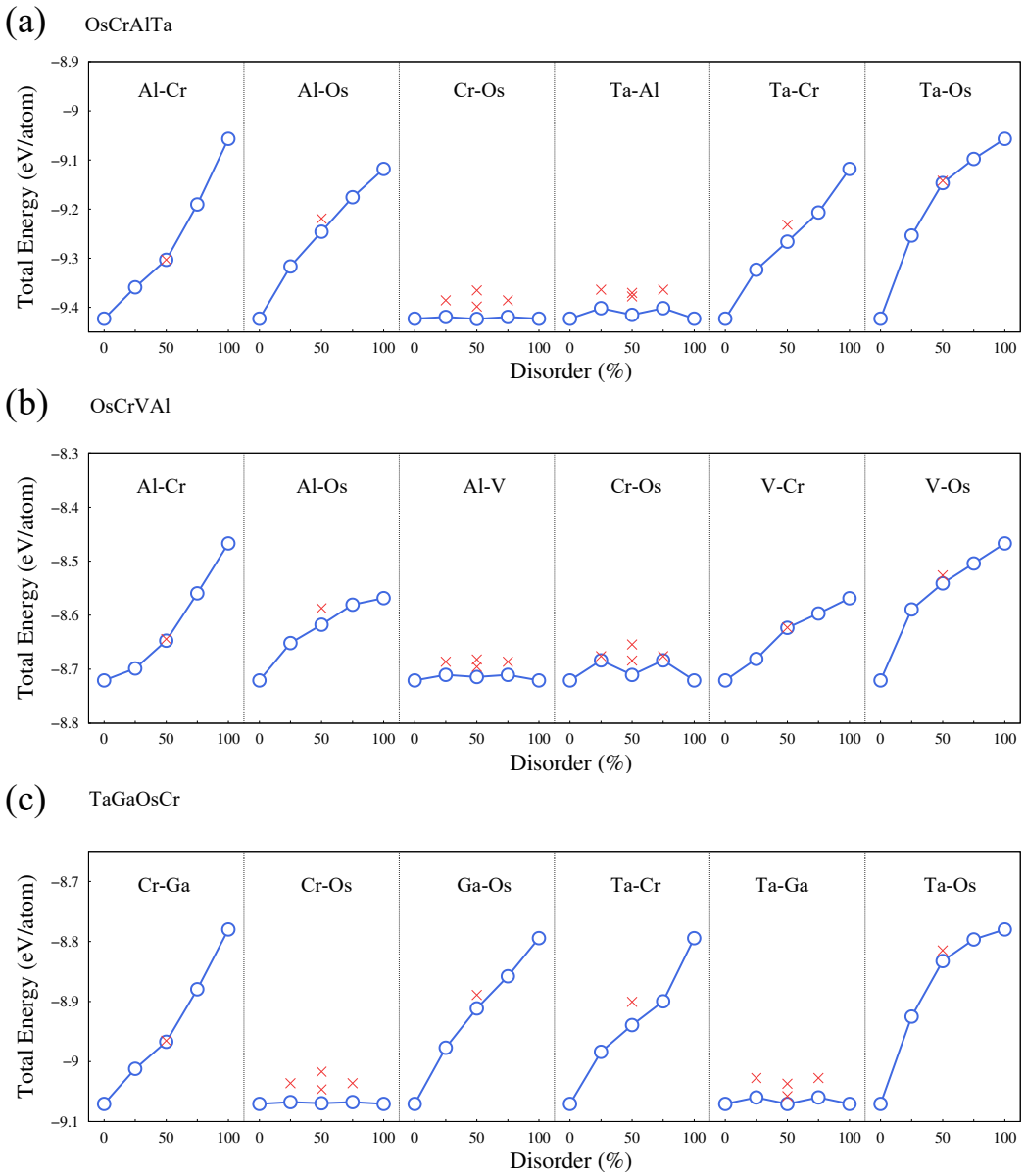

Figure 4.9: Disorder effects of (a) OsCrAlTa (b) OsCrVAl (c) TaGaOsCr.

4.3.5 Disordering Effects

We developed a method to verify the ordered structure of the seven selected quaternary Heusler compounds by swapping atoms. Since quaternary heusler compound has four atoms, there are six combinations between atom swapping. For example, in the case of IrCrAlTi, the swapping combinations are Al-Cr, Al-Ir, Cr-Ir, Ti-Al, Ti-Cr, and Ti-Ir. In the Figure 4.8 and 4.9, we show the total energy vs. the disorder percentage for all seven selected quaternary Heusler compounds. In the swap combination of Al-Cr, 50% disorder means swapping 2 Al atoms with 2 Cr atoms, and 100% disorder means swapping 4 Al atoms with 4 Cr atoms. Accordingly, 0% and 100% disorder correspond to ordered structures. Due to the symmetry of space group no. 216, in the case of IrCrAlTi, the total energy points of swap combinations of Cr-Ir and Ti-Al are symmetric along the 50% disorder. If the energy difference between the ordered structures and the disordered structures is more than 25 meV/atom and the disordered structure has the lowest total energy, we considered the compound is tend to be disorder. By using the swapping method, we confirmed that all selected seven quaternary heusler compound are in favour of ordered structure. Noted that in the case of IrMnZnTi, the Ti-Zn disorder structure has the lowest total energy, but we still consider it favours ordered structure due to the energy difference between the ordered and disordered structures is less than 25 meV/atom.

4.4 Conclusion

In summary, we have performed a systematic high-throughput screening of quaternary Heusler compounds for the application of p-MTJs. By using the descriptors of ΔE_f and ΔE_{Hull}, 3094 quaternary Heusler entries were recognized as thermodynamically stable from the OQMD database, among which 484, 80, and 202 compounds were confirmed with FM, FI, and AFM ground states, respectively. 97 most stable quaternary Heusler structures were futher filtered by considering the competing phases of space group of $P\bar{4}3m$(#215) and $P4/nmm$(#129). A

total number of 7 quaternary Heusler compounds,including AlTiOsMn, IrCrAlTi, IrCrGaTi, IrMnZnTi, OsCrAlTa, OsCrAlTa, OsCrAlV, and TaGaOsCr were eventually selected as our final candidates using a series descriptors of lattice misfit, magnetic anisotropy constant, cleavage energy, spin polarization, TMR ratio, effective magnetic anisotropy, and disordering effects. This work demonstrates an efficient way to accelerate the discovery of quaternary Heusler materials for the functional materials interface via combinations of effective materials descriptors and high-throughput first-principle calculations on the basis of large quantum materials repositories.

4.5 Acknowledgement

Chapter 4, in full, is submitted for publication of the material "Accelerate the Discovery of Quaternary Heusler Materials for Perpendicular Magnetic Tunnel Junctions via High-throughput first-principle Calculations", Sicong Jiang, Kesong Yang. The dissertation author was the primary investigator and author of this paper.

Chapter 5

Evaluate disorder effects of the quaternary heusler compound via high-throughput *ab-initio* calculation

In chapter 4, we presented a high-throughput screening for the quaternary Heusler compounds and selected 7 promising candidate materials interfaces. In this chapter, we provided a swapping method to evaluate the disorder effects in quaternary Heusler compounds. We proved the accuracy and efficiency of our method by testing three different cases, the ordered structure of CoFeCrGe, the $L2_1$ disordering in the CoMnCrAl due to mixing of Co-Mn or Al-Cr, and the DO_3 disordering in the CoFeMnGe results from the mixing of Co-Fe-Mn. It is worth mentioning that our calculation of the DO_3 CoFeMnGe is in good agreement with a recent experimental research. Our approach can be used to provide a quick guide for future prediction of phase stability of Heusler compounds and can be extended to other materials beyond Heusler family.

5.1 Introduction

Heusler compounds are one of the most exciting families of ternary and quaternary intermetallic compounds in the field of spintronics, since the first discovery of half-metallicity of NiMnSb by de Groot *et al.* in 1983[24]. Lasting for more than 100 years, Heusler compounds have continuously attracted great attention due to their excellent properties including half-metallicity [27, 28, 29], ferromagnetism[30], antiferromagnetism [31], ferrimagnetism [32], giant anomalous hall effect[33], superconductivity[34, 35], thermoelectricity[41, 40, 176, 83, 84], topological property[43], and magnetic shape memory effect[177, 178]. To date, apart from the traditional ternary Full Heusler (X_2YZ) and Half Heusler (XYZ) compounds the discovery and prediction of equiatomic quaternary heusler ($XX'YZ$) compounds with stoichiometry $1:1:1:1$, where X, X', and Y are transition metals (TMs) and Z is the main group element, offers much larger composition space in tuning the materials properties[179, 168, 109]. Despite the wide applications of quaternary Heusler compounds, their potential applications in the memory recording such as magnetic tunnel junctions (MTJs) can be strongly affected by the common disordering effects between atoms. This is mainly associated with the detriment of the half-metallicity in quaternary Heusler phases by the atomic disordering[180].

Significant efforts have been made to investigate the degree of chemical order in quaternary Heusler compounds. In 2015, Venkateswara et al. studied the $L2_1$ disordered structure in CoMnCrAl resulting from the mixing of Al and Cr atoms[175]. Later, by using DFT calcualtions, Johnson et al. verified the possibility of $L2_1$ disordering in the CoMnCrAl, while the half-metallicity can be still maintained[180]. Apart from the $L2_1$ disodering, B2 disordering is also studied in the quaternary Heusler compounds. In 2011, Klaer et al. observed the B2 type disorder in the CoFeMnAl[181] due to the influence of Al atom[182]. Highly ordered B2 structure were also reported in the CoFeCrAl[183, 184]. In 2015, by employing the neutron diffraction, Halder et al. confirmed the B2 disordering of NiCoMnAl, where completely random distributions were

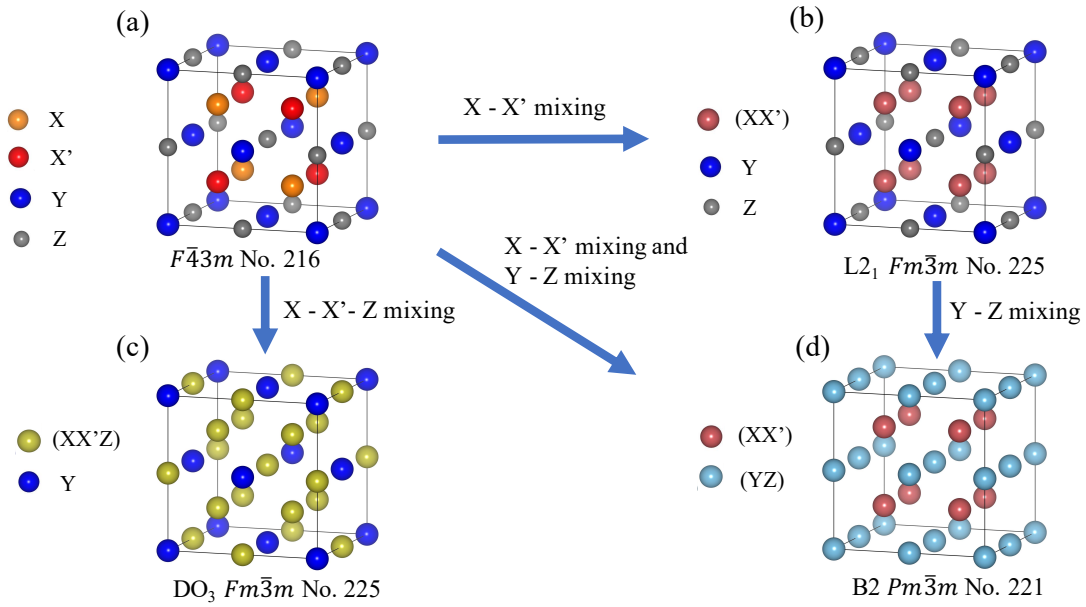

Figure 5.1: Schematic illustration of crystal structures of quaternary Heusler for (a) ordered phase with space group $F\bar{4}3m$(#216) (b) $L2_1$ phase with space group $Fm\bar{3}m$(#225) (c) DO_3 phase with space group $Fm\bar{3}m$(#225) (d) B2 phase with space group $Pm\bar{3}m$(#221).

found between Mn and Al atoms, and between Ni and Co atoms[185]. Bainsla et al. observed DO_3 disordering in CoFeCrGa[186], and CoMnFeZ (Z = Si, Ge)[187, 188] by means of ^{57}Fe Mössbauer spectroscopic measurement.

Despite the substantial experimental investigations, an efficient computational method that can predict the chemical disorder including the $L2_1$, B2, and DO_3 phases in quaternary Heusler compounds is lacking. In this paper, we proposed a swapping method to predict the disordering effects in the quaternary Heusler ($XX'YZ$) compounds. We proved the accuracy and efficiency of our method by testing three different cases, the ordered structure of CoFeCrGe, the $L2_1$ disordering in the CoMnCrAl, and the DO_3 disordering in the CoFeMnGe. It is worth mentioning that our calculation of the DO_3 CoFeMnGe is in good agreement with a recent experimental research. Our approach can be used to provide a quick guide for future prediction of phase stability of Heusler compounds and can be extended to other materials beyond Heusler family.

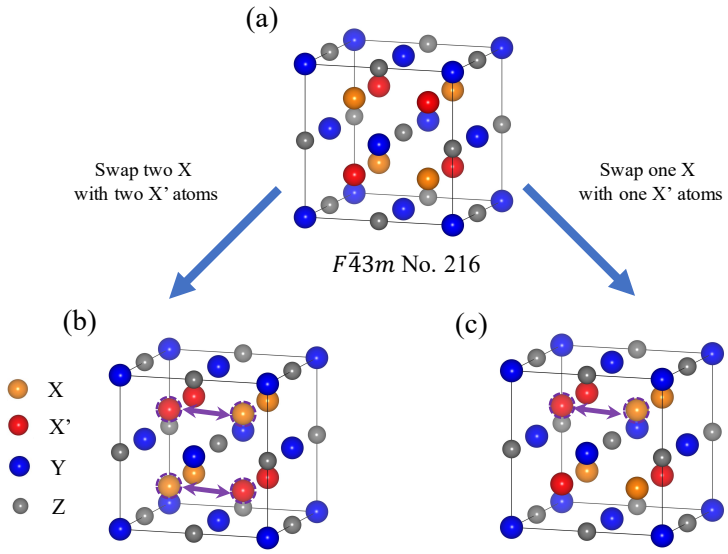

Figure 5.2: Illustration of the swapping method for quaternary Heusler $XX'YZ$ (a) ordered structure (b) swapping two X with two X' atoms (c) swapping one X with one X' atom.

5.2 Methods

The first-principles calculations were carried out for bulk quaternary Heusler compounds using the automatic framework AFLOW[113] based on Vienna *Ab-initio* Simulation Package (VASP)[146]. The projector augmented wave (PAW) pseudopotentials[114] were used for electron-ion interactions and the generalized gradient approximation (GGA) parameterized by Perdew-Burke-Ernzerhof (PBE) was used for exchange-correction functional.[115] All structures were fully relaxed with a convergence tolerance of 0.01 meV/atom and a k-points grid of 0.05 Å^{-1}. A much denser k-points grid of 0.04 Å^{-1} were set for static calculations. Cutoff energy and all other computational parameters were automatically generated in appropriate values by the AFLOW code for both structural relaxation and static calculations.

5.3 Results and Discussion

As was shown in Table 5.1 for a given quaternary Heusler composition, depending on the occupation of different lattice sites, there are three energetically non-degenerate ordered $F\bar{4}3m$ (#216) structures[53, 173]. Fig. 5.1a shows the ordered structure of Type I quaternary Hesuler compounds, where X and X' atoms are at the Wyckoff positions 4c (1/4, 1/4, 1/4) and 4d (3/4, 3/4, 3/4), respectively, and Y and Z atoms take the position of 4a (0, 0, 0) and 4b (1/2, 1/2, 1/2), respectively. In Fig. 5.1b, if the random distribution happens between X-X' atoms, the $L2_1$ phase with space group of $Fm\bar{3}m$(#225) can form, where $X(X')$ atoms occupy the Wyckoff position 8c (1/4, 1/4, 1/4), and Y and Z atoms are at 4a (0, 0, 0) and 4b (1/2, 1/2, 1/2), respectively. If the random distribution are between the X-X'-Z atoms, a disordered DO_3 phase with space group $Fm\bar{3}m$(#225) may exist, see Fig. 5.1c. Accordingly, Fig. 5.1d shows the random distribution between X-X' and Y-Z, resulting in the disordered B2 phase with space group of $Pm\bar{3}m$(#221). A complete disorder between all four elements can lead to the structure of A2 phase (bcc lattice), where all lattice sites become equivalent.

We developed a swapping method to analyze the disordering effects of the quaternary Heusler with python scripts and pymatgen package[189]. Fig. 5.2a shows the ordered structure of quaternary Heusler compound. For a quaternary Heusler compounds with the stoichiometric composition $XX'YZ$, there are six combinations between atom swapping, including X-X', X-Y, X-Z, X'-Y, X'-Z, and Y-Z. In each swapping combination, the cases can be further divided by the number of atoms swapped. Two types of swapping cases between two atoms were displayed in Fig. 5.2b and 5.2c for swapping two X with two X' atoms and swapping one X with one X' atom, respectively. Due to the symmetry of space group $F\bar{4}3m$(#216), swapping three $X(Y)$ with three $X'(Z)$ and swapping one $X(Y)$ with one $X'(Z)$ atom give the same structure. Meanwhile, structures we got after switching four X with four X' atoms and switching four Y with four Z atoms are identical to the initial ordered structure. Noted that the total number of unique structures after

Table 5.1: Three groups of energetically non-degenerate Wyckoff positions of quaternary Heusler compounds. Due to the symmetry of space group $F\bar{4}3m$(#216), switching between $X(Y)$ and $X'(Z)$ does not change the structure.

Crystal structure	4*a* (0,0,0)	4*b* (1/2,1/2,1/2)	4*c* (1/4,1/4,1/4)	4*d* (3/4,3/4,3/4)
Type I	Y	Z	X	X'
Type II	X'	Z	X	Y
Type III	X	Z	Y	X'

swapping one or two $X(Y)$ with $X'(Z)$ atoms are two and three, respectively.

Fig. 5.3a and Fig. 5.3b show the 6 swap cases of total energy vs. disorder percentage for CoFeCrGe and CoMnCrAl, respectively. The swapping combinations are Co-Cr, Co-Fe, Co-Ge, Fe-Cr, Ge-Cr, and Ge-Fe, for quaternary Heusler CoFeCrGe. In the swap combination of Co-Cr, 50% disorder means swapping 2 Co atoms with 2 Cr atoms, and 100% disorder means swapping 4 Co atoms with 4 Cr atoms. Accordingly, 0% and 100% disorder indicate ordered structures. Due to the symmetry of space group $F\bar{4}3m$(#216), the total energy points of swap combinations of Co-Fe and Ge-Cr are symmetric along the 50% disorder. The blue hollow point represents the lowest energy at the disorder percentage, and the red cross indicates total energy of the structure with same disorder percentage. Consequently, a concave-like graph along the 0 to 100% disorder implies that the swapped two atoms are tend to be mixed, while a convex-like graph or a monotonic increasing graph shows that the corresponding swapped two atoms are less likely to be disordered. Based on our DFT calculations, the quaternary Heusler CoFeCrGe with Type I has the lowest total energy among three groups of energetically non-degenerate Wyckoff positions, which is in good agreement with both previous theoretical calculations and experiments[175]. As was shown in Fig. 5.3a, the Co-Cr, Co-Fe, Co-Ge, Ge-Cr, and Ge-Fe are not tend to be mixed, since the ordered structures have the lowest total energy, compared with structures with swapped atoms. For the swapping combination of Fe-Cr, though the total energy of 50% disorder of Fe-Cr is less than the ordered structure, we can still consider the CoFeCrGe is ordered. This is because the energy difference between the 50% disorder of Fe-Cr and ordered structure is only 18.4 meV/atom.

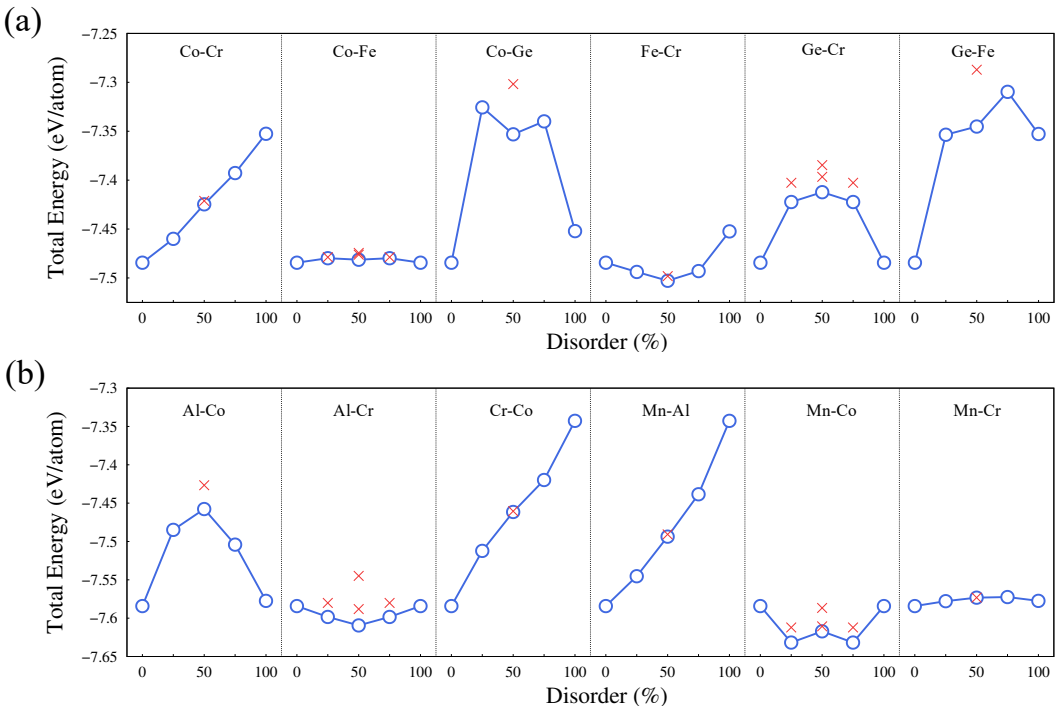

Figure 5.3: 6 swap cases of total energy vs. disorder for (a) CoFeCrGe, which was reported with an ordered structure in previous experiments and (b) CoMnCrAl, which was reported with $L2_1$ disordering by both experiments and theoretical calculations.

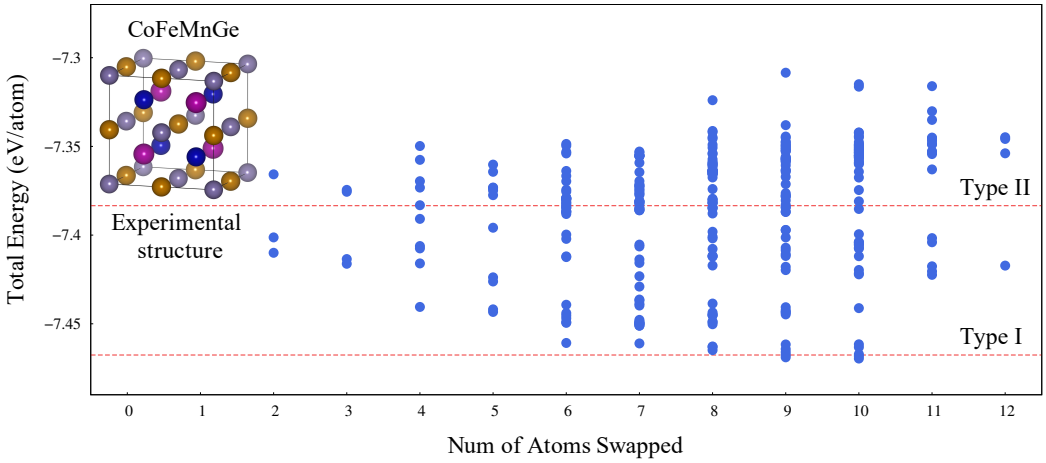

Figure 5.4: Total energy vs. the num of atoms swapped up to 12 atoms to represent the DO_3 disordering in CoFeMnGe. The red dash-line represent the

In general, if the energy difference between the ordered structures and the disordered structures is more than 25 meV/atom (k_bT at room temperature) and the disordered structure has the lowest total energy, we considered the compound is tend to be disorder. Therefore, our disorder analysis using the swap method shows that quaternary Heusler CoFeCrGe is an ordered structure. This is also consistent with previous experimental research[175]. In the case of CoMnCrAl, 6 swapping combinations of Al-Co, Al-Cr, Cr-Co, Mn-Al, Mn-Co, and Mn-Cr were shown in Fig. 5.3b. According to our DFT calculations, the most stable ordered quaternary structure for CoMnCrAl is Type I, among the three groups of energetically non-degenerate Wyckoff positions, consistent with previous XRD refinment data and DFT calculations[175]. This total energy vs. disorder percentage figure implies that Al-Co, Cr-Co, Mn-Al, Mn-Cr are not tend to be mixed, while Al-Cr and Mn-Co show convex-like graph. The total energy difference between the ordered structure and the disordered structure with the lowest energy are 25.3 meV/atom and 47.6 meV/atom for Al-Cr mixing and Mn-Co mixing, respectively. In particular, the mixing of Al-Cr was reported from the rietveld refinement of XRD data in a previous experiment[175] and the the mixing of Mn-Co was confirmed in the earlier DFT calculation[180]. These two cases discussed above show the reliability of the swapping method, where the general tendency of mixing between atoms can be achieved in a fast and efficient way.

Next, We further extend the swapping method to investigated the DO_3 mixing between three elements, X, X', and Z. Since there are 16 atoms in the conventional structure of quaternary Heusler compounds, the number of atoms swapped can be up to 12 for DO_3 disordering. Considering all the possible combinations of swapping there are 34,650 structures, where only 309 of them are unique structures. Fig. 5.4 shows the distribution of total energy vs. the number of atoms swapped for all these 309 unique structures. The red dash-lines from bottom to top show the total energy of the ordered quaternary structure of Type I CoFeMnGe and Type II CoFeMnGe, respectively. Noted that due to the nearly equal scattering amplitudes of all elements in CoFeMnGe, earlier experiments can not perform an accurate order-disorder analysis of the

synthesized CoFeMnGe compound[172]. However, previous DFT calculation shows that Type I structure is the most stable[172]. This is in agreement with our results in Fig. 5.4, where Type I structure shows the lowest total energy among the three types of ordered structures. Interestingly, in order to perform the analysis of order-disorder on CoFeMnGe compound, a recent experiments performed the ^{57}Fe Mössbauer spectroscopic measurement and confirmed that the synthesized structure by arc melting is Type II CoFeMnGe with considerable amount of DO_3 disordered phase[187]. According to our calculation results in Fig. 5.4, there are a large amount of data points with DO_3 disordering below the red dash-line of Type II structure. In other words, on the basis of our calculation, if the structure of synthesized CoFeMnGe is Type II, considerable amount of disordered DO_3 phases can be found. Therefore, their findings can prove the reliability of our swapping method in predicting the DO_3 disordering in the quaternary Heusler compounds.

5.4 Conclusion

In summary, we demonstrated an effective approach to predict the disordering effects in the quaternary Heusler compounds. The swapping method is tested to be reliable and are able to provide a quick guide on the tendency of atom mixing for quaternary Heusler compounds. By using the 12 atoms swapping method, we successfully verified the DO_3 disordering in CoFeMnGe, a recent experimental reported compound. Our approach can serve as an efficient tool for future understanding of phase stability of Heusler compounds.

5.5 Acknowledgement

Chapter 5, in part, is being prepared for submission for publication of the material "Evaluate disorder effects of the quaternary heusler compound via high-throughput *ab-initio* calculation", Sicong Jiang, Kesong Yang. The dissertation author was the primary investigator

and author of this paper.

Chapter 6

Summary and Outlook

In summary, we have presented a systematic high-throughput screening of Heusler/MgO material interface with strong PMA for the application of novel p-MTJs towards high thermal stability and low energy consumption. A general workflow including querying open quantum material repositories, developing effective material descriptors, and performing large-scale *ab-initio* calculations was provided. Our work not only provides a guide for the future discovery of novel Heusler alloys but also opens up possibilities for other advanced functional materials beyond Heusler families.

Thanks to the high-throughput computational materials design approach, hundreds of novel Heusler alloys have been identified from a large number of candidate compounds, awaiting further experimental validation. Also, as shown in Fig. 1.1, the highly tunable structures and compositions of Heusler alloys allow for a wide variety of properties, which leads to novel applications beyond spintronics and thermoelectrics. Accordingly, there is still much space to further explore their novel properties for enhanced functional applications. Several possible future research directions were highlighted as below:

i) Interface-driven magnetic effects such as perpendicular magnetic anisotropy at the magnetic metal/oxide interface are attracting increasing attention because of their promising

spintronic applications [1, 101, 190, 138, 191, 9]. As one large family of compounds, Heusler alloys provide one ideal platform to study the interfacial magnetic effects and to design the desired interfacial magnetic properties, and thus future research efforts on such aspects are desired.

ii) Many Heusler alloys are promising candidates for spintronic devices due to their high spin polarization and potentially large TMR ratio [190, 138]. However, for the epitaxially grown Heusler films, their half-metallicity and spin polarization are strongly dependent on the surface configurations [192, 193, 194, 195]. Hence, systematic computational studies of the surface properties of Heusler alloys could be one future research direction.

iii) In addition to the high spin polarization, other parameters including the TMR ratio and damping constant are also of critical importance for spintronic devices such as STT-MRAM [133]. To date, it is impossible to directly calculate these parameters using the traditional first-principles DFT calculations in a high-throughput fashion. Therefore, future research efforts could be devoted to the development of computational techniques such as machine learning algorithms to predict these material properties in a high-throughput fashion.

iv) High-entropy materials such as alloys and ceramics have attracted increasing attention because of their superior properties and potential functional applications [196, 197]. The fundamental idea is that the increased configuration entropy caused by the presence of multiple elements in near-equiatomic proportions stabilize the compounds, which make those metastable compounds with desired properties possible to be synthesized in the experiment. Half Heusler and quaternary Heusler have the exactly equiatomic composition and thus it is expected that the solid solutions formed between half Heusler compounds (or between quaternary Heusler compounds) are excellent high-entropy alloys, offering great opportunities for novel materials design. For example, in 2019, Karati *et al.* reported a high-entropy alloy, $Ti_2NiCoSnSb$ with half Heusler structure, from the combination of half Heusler compounds TiNiSn and TiCoSb, with enhanced properties for thermoelectric applications [198]. Hence, it is expected that high-entropy Heusler alloys could be one future research direction.

v) Similar to the case of perovskite (ABX_3) and double perovskite ($AA'BB'X_6$), the concept of double half Heusler ($X'X''Y_2Z_2$), *e.g.*, $FeNiTi_2Sb_2$, has been recently proposed [199]. Compared to traditional half Heusler compounds with only three atoms in the primitive unit cell, the double half Heusler compounds have more atoms in the primitive unit cell, thus resulting in a potentially lower lattice thermal conductivity. Besides, their quaternary compositions also offer a much larger phase space than the ternary half Heusler compounds. Therefore, double half Heusler compounds provide one ideal materials platform to search for promising candidates for low-thermal-conductivity materials, which is worthy of future research efforts.

6.1 Acknowledgement

Chapter 6, in part, is a reprint of the material "Review of high-throughput computational design of Heusler alloys" as it appears in Journal of Alloys and Compounds, Sicong Jiang, Kesong Yang, 867, 158854, 2021. The dissertation author was the primary investigator and author of this paper.

Appendix A

Thermodynamically stable full, half, and quaternary Heusler compounds

Table A.1: Summary of 363 thermodynamically stable full Heusler compounds predicted from large-scale *ab-initio* calculations. Listed properties: convex hull distance ΔE_H (meV/atom), formation energy ΔE_f (eV/atom), lattice parameters a, b, c (Å), spin moment (μB/f.u.), structure type, and magnetic ordering type. The structure type includes regular cubic (reg. cub.), regular tetragonal (reg. tet.), inverse cubic (inv. cub.) and inverse tetragonal (inv. tet.). The magnetic type includes nonmagnetic (NM), ferromagnetic (FM), ferrimagnetic (FI), and antiferromagnetic (AFM).

Compounds	ΔE_H	ΔE_f	a	b	c	Spin moment	Structure type	Magnetic type
Ag_2CdSc	0	-0.2538	6.771	6.771	6.771	0.00	reg. cub.	NM
Ag_2CdY	0	-0.3067	6.999	6.999	6.999	0.00	reg. cub.	NM
Ag_2CdZr	0	-0.1011	6.777	6.777	6.777	0.00	reg. cub.	NM
Au_2CdLa	0	-0.6713	7.221	7.221	7.221	0.00	reg. cub.	NM
Au_2CdY	0	-0.6765	4.918	4.918	7.037	0.00	reg. tet.	NM
Au_2CdZr	0	-0.4598	6.783	6.783	6.783	0.00	reg. cub.	NM
Au_2CuZn	0	-0.1399	6.264	6.264	6.264	0.00	reg. cub.	NM
Au_2HfZn	0	-0.4408	6.591	6.591	6.591	0.00	reg. cub.	NM
Au_2HgLa	0	-0.6289	7.214	7.214	7.214	0.00	reg. cub.	NM
Au_2MnAl	7	-0.2585	6.375	6.375	6.375	3.87	reg. cub.	FM
Au_2MnZn	9	-0.1572	6.379	6.379	6.379	4.08	reg. cub.	FM
Au_2TiZn	0	-0.3432	4.566	4.566	6.390	0.00	reg. tet.	NM
Au_2ZnZr	0	-0.4694	6.636	6.636	6.636	0.00	reg. cub.	NM
Co_2CrAl	68	-0.2297	5.674	5.674	5.674	3.00	reg. cub.	FM
Co_2CrGa	32	-0.1016	5.713	5.713	5.713	3.03	reg. cub.	FM
Co_2CuGe	50	-0.0622	5.684	5.684	5.684	0.00	reg. cub.	NM
Co_2CuSi	57	-0.2454	5.570	5.570	5.570	0.00	reg. cub.	NM
Co_2FeAl	0	-0.3540	5.685	5.685	5.685	4.97	reg. cub.	FM

Continued on next page

Table A.1 – continued from previous page

Compounds	ΔE_H	ΔE_f	a	b	c	Spin moment	Structure type	Magnetic type
Co_2FeGa	0	-0.2200	5.707	5.707	5.707	5.02	reg. cub.	FM
Co_2FeGe	0	-0.1564	5.741	5.741	5.741	5.62	reg. cub.	FM
Co_2FeSi	0	-0.3472	5.609	5.609	5.609	5.42	reg. cub.	FM
Co_2FeSn	73	-0.0256	6.002	6.002	6.002	5.70	reg. cub.	FM
Co_2HfAl	13	-0.5726	6.012	6.012	6.012	1.00	reg. cub.	FM
Co_2HfGa	0	-0.4787	6.018	6.018	6.018	1.02	reg. cub.	FM
Co_2HfSc	18	-0.3959	4.425	4.425	6.268	0.98	reg. tet.	FM
Co_2HfSn	34	-0.3942	6.236	6.236	6.236	2.00	reg. cub.	FM
Co_2HfZn	0	-0.3231	4.230	4.230	5.990	0.00	reg. tet.	NM
Co_2IrGe	89	-0.0656	3.759	3.759	7.128	2.48	inv. tet.	FM
Co_2MnAl	0	-0.3538	3.989	3.989	5.700	4.02	reg. tet.	FM
Co_2MnGa	0	-0.2310	4.033	4.033	5.717	4.12	reg. tet.	FM
Co_2MnGe	0	-0.2484	5.723	5.723	5.723	5.00	reg. cub.	FM
Co_2MnSb	6	-0.0899	6.000	6.000	6.000	6.00	reg. cub.	FM
Co_2MnSi	0	-0.4296	3.949	3.949	5.623	5.00	reg. tet.	FM
Co_2MnSn	1	-0.1268	5.955	5.955	5.955	5.03	reg. cub.	FM
Co_2MnTi	0	-0.2802	5.807	5.807	5.807	4.94	reg. cub.	FM
Co_2MoGa	83	-0.0868	3.791	3.791	7.009	0.77	reg. tet.	FM
Co_2NbAl	0	-0.4273	5.956	5.956	5.956	2.00	reg. cub.	FM
Co_2NbZn	4	-0.1810	3.981	3.981	6.496	0.00	reg. tet.	NM
Co_2NiAl	74	-0.2732	3.678	3.678	6.732	2.65	inv. tet.	FM
Co_2NiGa	55	-0.1614	3.679	3.679	6.782	2.70	inv. tet.	FM

Continued on next page

Table A.1 – continued from previous page

Compounds	ΔE_H	ΔE_f	a	b	c	Spin moment	Structure type	Magnetic type
Co_2NiGe	44	-0.1200	3.655	3.655	6.793	2.36	inv. tet.	FM
Co_2NiSi	63	-0.3142	3.553	3.553	6.810	2.23	inv. tet.	FM
Co_2TaAl	0	-0.4608	5.938	5.938	5.938	1.96	reg. cub.	FM
Co_2TaZn	2	-0.2220	4.001	4.001	6.399	0.00	reg. tet.	NM
Co_2TiAl	0	-0.6027	5.813	5.813	5.813	0.97	reg. cub.	FM
Co_2TiGa	0	-0.5034	5.825	5.825	5.825	1.01	reg. cub.	FM
Co_2TiGe	0	-0.4822	5.837	5.837	5.837	2.00	reg. cub.	FM
Co_2TiSi	28	-0.6452	5.733	5.733	5.733	1.99	reg. cub.	FM
Co_2TiSn	0	-0.3654	6.072	6.072	6.072	2.00	reg. cub.	FM
Co_2TiZn	0	-0.3400	4.094	4.094	5.793	0.00	reg. tet.	NM
Co_2VAl	0	-0.4099	5.719	5.719	5.719	2.00	reg. cub.	FM
Co_2VGa	0	-0.2960	5.751	5.751	5.751	2.00	reg. cub.	FM
Co_2VSn	76	-0.0785	5.983	5.983	5.983	2.99	reg. cub.	FM
Co_2VZn	8	-0.1464	3.825	3.825	6.315	0.00	reg. tet.	NM
Co_2ZnZr	5	-0.2635	4.261	4.261	6.040	0.00	reg. tet.	NM
Co_2ZrAl	0	-0.5051	6.060	6.060	6.060	1.00	reg. cub.	FM
Co_2ZrSn	45	-0.3808	6.278	6.278	6.278	2.00	reg. cub.	FM
Cu_2AuPd	15	-0.1119	4.002	4.002	7.002	0.00	reg. tet.	NM
Cu_2CdZr	0	-0.1522	6.360	6.360	6.360	0.00	reg. cub.	NM
Cu_2HfZn	0	-0.1965	6.126	6.126	6.126	0.00	reg. cub.	NM
Cu_2MnAl	64	-0.1208	5.845	5.845	5.845	3.47	reg. cub.	FM
Cu_2TiZn	0	-0.1503	5.940	5.940	5.940	0.00	reg. cub.	NM

Continued on next page

Table A.1 – continued from previous page

Compounds	ΔE_H	ΔE_f	a	b	c	Spin moment	Structure type	Magnetic type
Cu_2ZnZr	0	-0.2202	6.172	6.172	6.172	0.00	reg. cub.	NM
Fe_2CoGe	0	-0.1449	5.679	5.679	5.679	5.03	inv. cub.	FM
Fe_2CoSi	0	-0.3570	5.590	5.590	5.590	4.93	inv. cub.	FM
Fe_2CuAl	44	-0.1523	3.568	3.568	7.701	4.63	reg. tet.	FM
Fe_2CuGa	55	-0.0798	3.591	3.591	7.650	4.72	reg. tet.	FM
Fe_2IrGa	0	-0.1987	5.923	5.923	5.923	5.13	inv. cub.	FM
Fe_2IrGe	45	-0.1085	5.894	5.894	5.894	4.93	inv. cub.	FM
Fe_2MnAl	16	-0.1954	5.671	5.671	5.671	0.00	reg. cub.	AFM
Fe_2MnGa	52	-0.0743	5.654	5.654	5.654	0.00	reg. cub.	AFM
Fe_2MnGe	14	-0.1112	3.987	3.987	5.797	3.12	reg. tet.	FM
Fe_2MnSi	6	-0.3365	5.557	5.557	5.557	3.00	reg. cub.	FM
Fe_2NiAl	47	-0.2765	5.727	5.727	5.727	4.77	inv. cub.	FM
Fe_2NiGa	33	-0.1663	5.752	5.752	5.752	4.87	inv. cub.	FM
Fe_2NiGe	11	-0.1532	3.546	3.546	7.572	4.84	reg. tet.	FM
Fe_2NiSi	46	-0.3211	3.482	3.482	7.402	4.68	reg. tet.	FM
Fe_2PtGa	72	-0.2343	5.901	5.901	5.901	5.04	inv. cub.	FM
Fe_2PtGe	83	-0.1536	3.680	3.680	8.086	5.23	reg. tet.	FM
Fe_2RhGa	87	-0.2520	5.887	5.887	5.887	5.03	inv. cub.	FM
Fe_2RuGa	45	-0.1015	5.928	5.928	5.928	5.51	inv. cub.	FM
Fe_2RuGe	35	-0.0918	5.810	5.810	5.810	4.89	inv. cub.	FM
Hf_2CoRe	0	-0.4025	4.547	4.547	6.429	0.00	reg. tet.	AFM
Hf_2CoTc	1	-0.4902	6.409	6.409	6.409	0.00	reg. cub.	NM

Continued on next page

Table A.1 – continued from previous page

Compounds	ΔE_H	ΔE_f	a	b	c	Spin moment	Structure type	Magnetic type
Hf_2CuRe	5	-0.2915	6.509	6.509	6.509	0.00	reg. cub.	NM
Hf_2CuTc	34	-0.3344	4.589	4.589	6.498	0.00	reg. tet.	NM
Hf_2FeOs	0	-0.5201	4.529	4.529	6.399	0.00	reg. tet.	NM
Hf_2IrMn	0	-0.6489	6.414	6.414	6.414	0.00	reg. cub.	NM
Hf_2IrMo	0	-0.6000	6.553	6.553	6.553	0.00	reg. cub.	NM
Hf_2IrRe	0	-0.7324	6.533	6.533	6.533	0.00	reg. cub.	NM
Hf_2IrTc	0	-0.8495	6.516	6.516	6.516	0.00	reg. cub.	NM
Hf_2MoRh	19	-0.5254	6.553	6.553	6.553	0.00	reg. cub.	NM
Hf_2OsRu	0	-0.7628	6.489	6.489	6.489	0.00	reg. cub.	NM
Hf_2OsTc	0	-0.6201	6.501	6.501	6.501	0.00	reg. cub.	NM
Hf_2PdRe	48	-0.5481	6.579	6.579	6.579	0.00	reg. cub.	NM
Hf_2PdTc	61	-0.6156	6.569	6.569	6.569	0.00	reg. cub.	NM
Hf_2ReRh	24	-0.6898	6.528	6.528	6.528	0.00	reg. cub.	NM
Hf_2ReZn	55	-0.2893	4.655	4.655	6.591	0.00	reg. tet.	NM
Hf_2RhTc	15	-0.7855	6.513	6.513	6.513	0.00	reg. cub.	NM
Hf_2RuTc	1	-0.6639	6.489	6.489	6.489	0.00	reg. cub.	NM
Hg_2AgLa	0	-0.4020	7.329	7.329	7.329	0.00	reg. cub.	NM
Hg_2AgSc	0	-0.2685	6.890	6.890	6.890	0.00	reg. cub.	NM
Hg_2AgY	0	-0.3637	7.099	7.099	7.099	0.00	reg. cub.	NM
Hg_2CdLa	0	-0.4679	7.427	7.427	7.427	0.00	reg. cub.	NM
Hg_2CdSc	0	-0.2767	7.009	7.009	7.009	0.00	reg. cub.	NM
Hg_2CdY	0	-0.3938	7.207	7.207	7.207	0.00	reg. cub.	NM

Continued on next page

Table A.1 – continued from previous page

Compounds	ΔE_H	ΔE_f	a	b	c	Spin moment	Structure type	Magnetic type
Ir_2HfZn	0	-0.7297	4.461	4.461	6.309	0.00	reg. tet.	NM
Ir_2TiZn	0	-0.6856	4.333	4.333	6.122	0.00	reg. tet.	NM
Ir_2ZnZr	10	-0.6297	6.351	6.351	6.351	0.00	reg. cub.	NM
Mn_2CoAl	33	-0.2704	5.664	5.664	5.664	2.03	inv. cub.	FI
Mn_2CoCr	0	-0.0662	5.680	5.680	5.680	4.84	reg. cub.	FI
Mn_2CoGa	5	-0.1798	5.746	5.746	5.746	2.01	inv. cub.	FI
Mn_2CoSi	20	-0.3614	5.563	5.563	5.563	3.00	inv. cub.	FI
Mn_2CuGa	73	-0.0374	3.834	3.834	7.142	5.85	reg. tet.	FM
Mn_2CuGe	40	-0.0508	3.769	3.769	7.175	5.30	reg. tet.	FM
Mn_2FeAl	74	-0.1525	5.748	5.748	5.748	2.89	inv. cub.	FI
Mn_2FeGa	48	-0.0953	5.761	5.761	5.761	1.04	inv. cub.	FI
Mn_2FeGe	0	-0.1525	5.729	5.729	5.729	2.00	inv. cub.	FI
Mn_2FeSi	0	-0.3769	5.608	5.608	5.608	2.00	inv. cub.	FI
Mn_2IrGa	0	-0.2750	5.988	5.988	5.988	1.69	inv. cub.	FI
Mn_2IrGe	46	-0.1747	5.940	5.940	5.940	3.00	inv. cub.	FI
Mn_2MoGa	76	-0.0719	5.898	5.898	5.898	1.03	reg. cub.	FI
Mn_2MoGe	62	-0.0628	5.881	5.881	5.881	0.00	reg. cub.	NM
Mn_2NbTi	3	-0.2408	6.031	6.031	6.031	0.49	reg. cub.	FM
Mn_2NiAl	76	-0.2782	5.806	5.806	5.806	1.17	inv. cub.	FI
Mn_2NiGa	35	-0.1390	5.828	5.828	5.828	1.20	inv. cub.	FI
Mn_2NiGe	72	-0.1454	3.716	3.716	7.201	0.00	reg. tet.	AFM
Mn_2OsGe	34	-0.0730	5.916	5.916	5.916	2.01	inv. cub.	FI

Continued on next page

Table A.1 – continued from previous page

Compounds	ΔE_H	ΔE_f	a	b	c	Spin moment	Structure type	Magnetic type
Mn_2PtCo	0	0.3577	5.799	5.799	5.799	2.25	reg. cub.	FM
Mn_2PtGa	96	-0.2686	3.900	3.900	7.575	0.00	reg. tet.	AFM
Mn_2PtGe	69	-0.1955	3.883	3.883	7.642	0.00	reg. tet.	AFM
Mn_2PtPd	0	-0.2304	6.138	6.138	6.138	0.00	reg. cub.	AFM
Mn_2PtRh	0	-0.2487	6.081	6.081	6.081	0.00	reg. cub.	AFM
Mn_2PtV	37	-0.3204	4.246	4.246	6.037	4.84	reg. tet.	FI
Mn_2RhGa	47	-0.1406	5.967	5.967	5.967	1.63	inv. cub.	FI
Mn_2RhGe	64	-0.2436	5.927	5.927	5.927	3.00	inv. cub.	FI
Mn_2RuGe	0	-0.2052	5.896	5.896	5.896	1.92	inv. cub.	FI
Mn_2RuSi	8	-0.3884	5.749	5.749	5.749	1.94	inv. cub.	FI
Mn_2RuSn	86	-0.0436	6.195	6.195	6.195	1.68	inv. cub.	FI
Mn_2TaTi	0	-0.2874	4.247	4.247	6.006	0.48	reg. tet.	FM
Mn_2TiV	5	-0.2850	5.797	5.797	5.797	0.00	reg. cub.	NM
Mn_2TiW	1	-0.2420	4.192	4.192	5.931	0.00	reg. tet.	NM
Mn_2VAl	0	-0.3329	5.764	5.764	5.764	1.99	reg. cub.	FI
Mn_2VGa	0	-0.2453	5.802	5.802	5.802	1.99	reg. cub.	FI
Mn_2WGa	61	-0.0875	5.905	5.905	5.905	0.95	reg. cub.	FI
Mn_2WGe	61	-0.0350	5.883	5.883	5.883	0.00	reg. cub.	NM
Mo_2NbTa	1	-0.1597	6.456	6.456	6.456	0.00	reg. cub.	NM
Mo_2NbW	0	-0.1031	4.522	4.522	6.392	0.00	reg. tet.	NM
Mo_2TaW	0	-0.1349	4.523	4.523	6.398	0.00	reg. tet.	NM
Mo_2TiW	1	-0.1235	4.470	4.470	6.316	0.00	reg. tet.	NM

Continued on next page

Table A.1 – continued from previous page

Compounds	ΔE_H	ΔE_f	a	b	c	Spin moment	Structure type	Magnetic type
Mo_2VW	0	-0.0991	4.413	4.413	6.240	0.00	reg. tet.	NM
Nb_2CrOs	5	-0.1890	4.440	4.440	6.286	0.00	reg. tet.	NM
Nb_2MoOs	0	-0.2696	4.526	4.526	6.402	0.00	reg. tet.	NM
Nb_2MoRe	0	-0.2389	6.422	6.422	6.422	0.00	reg. cub.	NM
Nb_2MoRu	1	-0.2484	4.520	4.520	6.390	0.00	reg. tet.	NM
Nb_2MoTc	5	-0.2458	6.410	6.410	6.410	0.00	reg. cub.	NM
Nb_2OsW	6	-0.1867	4.536	4.536	6.413	0.00	reg. tet.	NM
Nb_2ReTc	0	-0.3261	4.513	4.513	6.386	0.00	reg. tet.	NM
Ni_2CoGe	73	-0.1607	3.671	3.671	6.740	0.96	inv. tet.	FM
Ni_2CoSb	94	-0.0232	3.913	3.913	6.538	0.00	inv. tet.	NM
Ni_2CoSi	80	-0.3445	3.610	3.610	6.577	0.86	inv. tet.	FM
Ni_2FeAl	59	-0.3181	3.676	3.676	6.862	3.17	reg. tet.	FM
Ni_2HfZn	0	-0.3329	6.054	6.054	6.054	0.00	reg. cub.	NM
Ni_2MnAl	0	-0.4002	5.752	5.752	5.752	4.01	reg. cub.	FM
Ni_2MnGa	6	-0.2984	5.805	5.805	5.805	4.04	reg. cub.	FM
Ni_2MnGe	17	-0.2367	5.810	5.810	5.810	3.95	reg. cub.	FM
Ni_2MnSb	68	-0.1158	6.002	6.002	6.002	3.91	reg. cub.	FM
Ni_2MnSi	70	-0.3628	5.679	5.679	5.679	3.80	reg. cub.	FM
Ni_2MnSn	12	-0.1775	5.995	5.995	5.995	4.01	reg. cub.	FM
Ni_2TiZn	0	-0.2959	5.863	5.863	5.863	0.00	reg. cub.	NM
Os_2HfSc	0	-0.5543	6.451	6.451	6.451	0.00	reg. cub.	NM
Os_2NbSc	1	-0.4477	4.511	4.511	6.387	0.00	reg. tet.	NM

Continued on next page

Table A.1 – continued from previous page

Compounds	ΔE_H	ΔE_f	a	b	c	Spin moment	Structure type	Magnetic type
Os_2ScTa	0	-0.5308	6.376	6.376	6.376	0.00	reg. cub.	NM
Os_2ScZr	0	-0.4698	6.489	6.489	6.489	0.00	reg. cub.	NM
Os_2TaTi	0	-0.4810	4.438	4.438	6.284	0.00	reg. tet.	NM
Pd_2AgCd	5	-0.2588	4.294	4.294	7.352	0.00	reg. tet.	NM
Pd_2AgHg	6	-0.1463	4.343	4.343	7.310	0.00	reg. tet.	NM
Pd_2AuCd	9	-0.2950	4.291	4.291	7.385	0.00	reg. tet.	NM
Pd_2AuHg	6	-0.1627	4.375	4.375	7.234	0.00	reg. tet.	NM
Pd_2CdSc	0	-0.7208	6.552	6.552	6.552	0.00	reg. cub.	NM
Pd_2CdY	0	-0.7280	6.777	6.777	6.777	0.00	reg. cub.	NM
Pd_2CdZr	0	-0.5800	6.595	6.595	6.595	0.00	reg. cub.	NM
Pd_2CuZn	0	-0.3970	6.047	6.047	6.047	0.00	reg. cub.	NM
Pd_2HfZn	13	-0.6689	4.075	4.075	7.739	0.00	reg. tet.	NM
Pd_2MnAu	68	-0.2344	4.029	4.029	7.727	0.00	reg. tet.	AFM
Pd_2MnCu	18	-0.2313	6.094	6.094	6.094	0.00	reg. cub.	AFM
Pd_2MnGa	35	-0.4773	4.029	4.029	7.294	4.10	reg. tet.	FM
Pd_2MnGe	79	-0.3360	6.217	6.217	6.217	4.11	reg. cub.	FM
Pd_2MnSb	15	-0.3319	6.434	6.434	6.434	4.29	reg. cub.	FM
Pd_2MnSn	0	-0.4322	6.388	6.388	6.388	4.13	reg. cub.	FM
Pd_2MnZn	19	-0.4164	4.102	4.102	6.914	0.00	reg. tet.	AFM
Pd_2ScZn	12	-0.7775	4.154	4.154	7.390	0.00	reg. tet.	NM
Pd_2TiZn	31	-0.5627	3.981	3.981	7.500	0.00	reg. tet.	NM
Pd_2ZnZr	16	-0.6330	4.098	4.098	7.813	0.00	reg. tet.	NM

Continued on next page

Table A.1 – continued from previous page

Compounds	ΔE_H	ΔE_f	a	b	c	Spin moment	Structure type	Magnetic type
Pt_2MnZn	51	-0.4960	4.020	4.020	7.201	0.00	reg. tet.	AFM
Pt_2ScZn	52	-0.9280	4.131	4.131	7.498	0.00	reg. tet.	NM
Re_2MoTi	0	-0.2671	4.418	4.418	6.250	0.00	reg. tet.	NM
Re_2NbTa	1	-0.3548	4.527	4.527	6.397	0.00	reg. tet.	NM
Re_2NbTi	0	-0.3741	4.469	4.469	6.310	0.00	reg. tet.	NM
Re_2TaTi	0	-0.4304	4.473	4.473	6.318	0.00	reg. tet.	NM
Re_2TiV	7	-0.3734	4.337	4.337	6.127	0.00	reg. tet.	NM
Re_2TiW	0	-0.3218	4.427	4.427	6.259	0.00	reg. tet.	NM
Rh_2CdHf	22	-0.6753	4.547	4.547	6.471	0.00	reg. tet.	NM
Rh_2CdSc	14	-0.6178	4.545	4.545	6.450	0.00	reg. tet.	NM
Rh_2CdZr	1	-0.6188	4.572	4.572	6.522	0.00	reg. tet.	NM
Rh_2CoSb	82	-0.2012	4.017	4.017	7.346	2.05	reg. tet.	FM
Rh_2CoSn	67	-0.2369	4.077	4.077	7.161	2.29	reg. tet.	FM
Rh_2CuTa	10	-0.4502	6.133	6.133	6.133	0.00	reg. cub.	NM
Rh_2FeGa	0	-0.4284	5.996	5.996	5.996	4.25	reg. cub.	FM
Rh_2FeIn	18	-0.2226	6.257	6.257	6.257	4.24	reg. cub.	FM
Rh_2FeSn	46	-0.2846	6.256	6.256	6.256	3.55	reg. cub.	FM
Rh_2FeZn	0	-0.2748	6.015	6.015	6.015	4.24	reg. cub.	FM
Rh_2HfZn	0	-0.8496	4.431	4.431	6.275	0.00	reg. tet.	NM
Rh_2MnAl	0	-0.7016	6.016	6.016	6.016	4.09	reg. cub.	FM
Rh_2MnGa	0	-0.5451	6.068	6.068	6.068	4.12	reg. cub.	FM
Rh_2MnGe	3	-0.4564	6.080	6.080	6.080	4.75	reg. cub.	FM

Continued on next page

Table A.1 – continued from previous page

Compounds	ΔE_H	ΔE_f	a	b	c	Spin moment	Structure type	Magnetic type
Rh_2MnHf	12	-0.6647	6.289	6.289	6.289	4.66	reg. cub.	FM
Rh_2MnIn	0	-0.3530	6.293	6.293	6.293	4.34	reg. cub.	FM
Rh_2MnPb	28	-0.1252	4.337	4.337	6.879	0.00	reg. tet.	AFM
Rh_2MnSb	0	-0.3839	4.158	4.158	7.183	4.19	reg. tet.	FM
Rh_2MnSc	14	-0.6272	6.231	6.231	6.231	4.33	reg. cub.	FM
Rh_2MnSn	0	-0.4722	6.271	6.271	6.271	4.76	reg. cub.	FM
Rh_2MnTi	0	-0.5797	4.334	4.334	6.126	5.76	reg. tet.	FM
Rh_2MnZn	5	-0.3150	6.018	6.018	6.018	3.36	reg. cub.	FM
Rh_2MnZr	12	-0.5866	6.344	6.344	6.344	4.72	reg. cub.	FM
Rh_2NbZn	49	-0.4819	4.106	4.106	7.078	0.00	reg. tet.	NM
Rh_2ScZn	9	-0.7728	4.407	4.407	6.243	0.00	reg. tet.	NM
Rh_2TaZn	46	-0.5412	4.118	4.118	7.008	0.00	reg. tet.	NM
Rh_2TiZn	0	-0.7669	4.310	4.310	6.096	0.00	reg. tet.	NM
Rh_2VZn	26	-0.4128	4.017	4.017	6.768	0.00	reg. tet.	NM
Rh_2ZnZr	0	-0.7679	4.455	4.455	6.339	0.00	reg. tet.	NM
Ru_2FeGa	2	-0.1385	5.949	5.949	5.949	3.11	reg. cub.	FM
Ru_2FeGe	0	-0.1415	6.015	6.015	6.015	3.98	reg. cub.	FM
Ru_2HfSc	1	-0.7248	6.430	6.430	6.430	0.00	reg. cub.	NM
Ru_2MnGa	0	-0.2607	5.998	5.998	5.998	0.00	reg. cub.	AFM
Ru_2MnNb	6	-0.1884	6.192	6.192	6.192	4.10	reg. cub.	FM
Ru_2MnTa	7	-0.2614	6.181	6.181	6.181	4.09	reg. cub.	FM
Ru_2MnV	3	-0.1559	5.974	5.974	5.974	3.94	reg. cub.	FM

Continued on next page

Table A.1 – continued from previous page

Compounds	ΔE_H	ΔE_f	a	b	c	Spin moment	Structure type	Magnetic type
Ru_2NbSc	0	-0.5450	6.363	6.363	6.363	0.00	reg. cub.	NM
Ru_2NbZn	5	-0.2704	4.375	4.375	6.185	0.00	reg. tet.	NM
Ru_2ScTa	0	-0.6243	6.353	6.353	6.353	0.00	reg. cub.	NM
Ru_2ScTi	22	-0.6440	6.269	6.269	6.269	0.00	reg. cub.	NM
Ru_2ScV	18	-0.4551	4.367	4.367	6.181	0.00	reg. tet.	NM
Ru_2ScZr	1	-0.6439	6.470	6.470	6.470	0.00	reg. cub.	NM
Ru_2TaTi	0	-0.5416	4.423	4.423	6.251	0.00	reg. tet.	NM
Ru_2TaY	84	-0.3352	4.625	4.625	6.543	0.00	reg. tet.	NM
Ru_2TaZn	12	-0.3415	4.378	4.378	6.184	0.00	reg. tet.	NM
Ru_2VZn	24	-0.2157	6.005	6.005	6.005	0.00	reg. cub.	NM
Ru_2WZn	0	-0.1227	6.127	6.127	6.127	0.00	reg. cub.	NM
Sc_2AgHg	0	-0.3718	6.945	6.945	6.945	0.00	reg. cub.	NM
Sc_2AgOs	76	-0.3739	4.672	4.672	6.582	0.00	reg. tet.	NM
Sc_2AgRu	79	-0.4404	4.680	4.680	6.584	0.00	reg. tet.	NM
Sc_2AuRu	81	-0.6740	4.671	4.671	6.530	0.00	reg. tet.	NM
Sc_2CoIr	1	-0.7202	4.494	4.494	6.376	0.88	reg. tet.	FM
Sc_2CoRu	0	-0.4658	6.327	6.327	6.327	0.00	reg. cub.	NM
Sc_2CuIr	1	-0.6980	6.454	6.454	6.454	0.00	reg. cub.	NM
Sc_2CuOs	0	-0.4057	6.429	6.429	6.429	0.00	reg. cub.	NM
Sc_2CuPt	1	-0.7973	6.526	6.526	6.526	0.00	reg. cub.	NM
Sc_2CuRu	14	-0.4675	6.427	6.427	6.427	0.00	reg. cub.	NM
Sc_2IrNi	1	-0.7531	4.538	4.538	6.369	0.00	reg. tet.	NM

Continued on next page

Table A.1 – continued from previous page

Compounds	ΔE_H	ΔE_f	a	b	c	Spin moment	Structure type	Magnetic type
Sc_2IrPd	1	-0.9893	4.630	4.630	6.493	0.00	reg. tet.	NM
Sc_2IrRh	0	-1.0411	4.569	4.569	6.442	0.00	reg. tet.	NM
Sc_2IrRu	0	-0.8283	4.540	4.540	6.423	0.00	reg. tet.	NM
Sc_2IrZn	0	-0.7217	4.625	4.625	6.572	0.00	reg. tet.	NM
Sc_2NiOs	0	-0.4460	4.514	4.514	6.368	0.00	reg. tet.	NM
Sc_2NiPt	0	-0.8427	6.477	6.477	6.477	0.00	reg. cub.	NM
Sc_2NiRu	9	-0.5278	4.506	4.506	6.361	0.00	reg. tet.	NM
Sc_2OsPd	44	-0.6866	4.598	4.598	6.489	0.00	reg. tet.	NM
Sc_2OsPt	41	-0.8384	4.583	4.583	6.465	0.00	reg. tet.	NM
Sc_2OsZn	25	-0.4376	6.525	6.525	6.525	0.00	reg. cub.	NM
Sc_2PdPt	0	-1.0899	6.604	6.604	6.604	0.00	reg. cub.	NM
Sc_2PdRu	39	-0.7792	4.596	4.596	6.488	0.00	reg. tet.	NM
Sc_2PtRu	17	-0.9581	4.575	4.575	6.462	0.00	reg. tet.	NM
Sc_2PtZn	1	-0.8374	6.628	6.628	6.628	0.00	reg. cub.	NM
Sc_2RhRu	2	-0.8172	6.429	6.429	6.429	0.00	reg. cub.	NM
Sc_2RuZn	45	-0.4906	6.533	6.533	6.533	0.00	reg. cub.	NM
Ta_2CrOs	0	-0.3031	6.274	6.274	6.274	0.00	reg. cub.	NM
Ta_2CrRu	21	-0.2731	4.423	4.423	6.252	0.00	reg. tet.	NM
Ta_2MoOs	0	-0.3898	4.529	4.529	6.402	0.00	reg. tet.	NM
Ta_2MoRe	0	-0.3341	4.545	4.545	6.431	0.00	reg. tet.	NM
Ta_2MoRu	0	-0.3698	4.522	4.522	6.390	0.00	reg. tet.	NM
Ta_2MoTc	6	-0.3484	6.412	6.412	6.412	0.00	reg. cub.	NM

Continued on next page

Table A.1 – continued from previous page

Compounds	ΔE_H	ΔE_f	a	b	c	Spin moment	Structure type	Magnetic type
Ta_2NbOs	0	-0.3151	4.567	4.567	6.461	0.00	reg. tet.	NM
Ta_2NbRu	17	-0.2668	6.452	6.452	6.452	0.00	reg. cub.	NM
Ta_2OsRe	0	-0.3443	6.385	6.385	6.385	0.00	reg. cub.	NM
Ta_2OsTc	0	-0.4041	4.499	4.499	6.368	0.00	reg. tet.	NM
Ta_2OsW	0	-0.2964	4.538	4.538	6.421	0.00	reg. tet.	NM
Ta_2ReRu	7	-0.3700	4.509	4.509	6.371	0.00	reg. tet.	NM
Ta_2ReTc	0	-0.4577	4.518	4.518	6.386	0.00	reg. tet.	NM
Ta_2ReW	6	-0.2700	4.555	4.555	6.438	0.00	reg. tet.	NM
Ta_2RuTc	7	-0.4113	4.492	4.492	6.354	0.00	reg. tet.	NM
Ta_2RuW	7	-0.2817	4.533	4.533	6.410	0.00	reg. tet.	NM
Tc_2HfMo	0	-0.2899	4.502	4.502	6.363	0.00	reg. tet.	NM
Tc_2HfNb	10	-0.4418	4.554	4.554	6.443	0.00	reg. tet.	NM
Tc_2HfTa	5	-0.5075	6.437	6.437	6.437	0.00	reg. cub.	NM
Tc_2HfW	0	-0.3410	4.504	4.504	6.369	0.00	reg. tet.	NM
Tc_2MoTi	0	-0.3368	4.397	4.397	6.217	0.00	reg. tet.	NM
Tc_2NbTa	0	-0.4278	4.505	4.505	6.372	0.00	reg. tet.	NM
Tc_2NbTi	0	-0.4524	4.446	4.446	6.296	0.00	reg. tet.	NM
Tc_2NbZr	10	-0.3640	4.574	4.574	6.474	0.00	reg. tet.	NM
Tc_2TaTi	0	-0.5198	6.291	6.291	6.291	0.00	reg. cub.	NM
Tc_2TaZr	7	-0.4268	4.572	4.572	6.467	0.00	reg. tet.	NM
Tc_2TiV	4	-0.4390	6.108	6.108	6.108	0.00	reg. cub.	NM
Tc_2TiW	0	-0.3902	4.403	4.403	6.230	0.00	reg. tet.	NM

Continued on next page

Table A.1 – continued from previous page

Compounds	ΔE_H	ΔE_f	a	b	c	Spin moment	Structure type	Magnetic type
Tc_2WZr	0	-0.2520	4.526	4.526	6.400	0.00	reg. tet.	NM
Ti_2CoIr	21	-0.6236	6.113	6.113	6.113	1.57	reg. cub.	FM
Ti_2CoMn	12	-0.3725	5.905	5.905	5.905	0.00	reg. cub.	NM
Ti_2CoRe	0	-0.4196	6.092	6.092	6.092	0.00	reg. cub.	AFM
Ti_2CoTc	0	-0.4916	6.068	6.068	6.068	0.00	reg. cub.	NM
Ti_2CrIr	0	-0.5353	6.114	6.114	6.114	0.68	reg. cub.	FM
Ti_2FeMn	10	-0.3300	5.917	5.917	5.917	0.43	reg. cub.	FM
Ti_2FeOs	1	-0.5434	6.059	6.059	6.059	0.00	reg. cub.	NM
Ti_2IrMn	0	-0.6845	4.294	4.294	6.073	0.00	reg. tet.	NM
Ti_2IrMo	0	-0.6054	6.239	6.239	6.239	0.00	reg. cub.	NM
Ti_2IrRe	0	-0.7291	4.391	4.391	6.211	0.00	reg. tet.	NM
Ti_2IrTc	0	-0.8194	4.380	4.380	6.197	0.00	reg. tet.	NM
Ti_2MnNi	44	-0.2749	5.945	5.945	5.945	0.00	reg. cub.	NM
Ti_2MnOs	0	-0.4918	6.066	6.066	6.066	0.00	reg. cub.	NM
Ti_2MnRh	51	-0.5662	4.285	4.285	6.059	0.00	reg. tet.	NM
Ti_2MoNi	0	-0.2118	4.351	4.351	6.152	0.00	reg. tet.	NM
Ti_2MoPd	41	-0.3690	4.449	4.449	6.289	0.00	reg. tet.	NM
Ti_2MoPt	0	-0.6247	4.437	4.437	6.279	0.00	reg. tet.	NM
Ti_2MoRh	11	-0.4948	6.241	6.241	6.241	0.00	reg. cub.	NM
Ti_2NiRe	18	-0.3527	6.125	6.125	6.125	0.00	reg. cub.	NM
Ti_2NiTc	19	-0.4095	4.318	4.318	6.107	0.00	reg. tet.	NM
Ti_2OsRu	0	-0.7215	4.360	4.360	6.172	0.00	reg. tet.	NM

Continued on next page

Table A.1 – continued from previous page

Compounds	ΔE_H	ΔE_f	a	b	c	Spin moment	Structure type	Magnetic type
Ti_2OsTc	0	-0.6122	6.186	6.186	6.186	0.00	reg. cub.	NM
Ti_2PdTc	67	-0.5191	4.421	4.421	6.251	0.00	reg. tet.	NM
Ti_2PtTc	48	-0.7223	6.241	6.241	6.241	0.00	reg. cub.	NM
Ti_2ReRh	30	-0.6415	6.209	6.209	6.209	0.00	reg. cub.	NM
Ti_2ReZn	53	-0.2876	4.420	4.420	6.256	0.00	reg. tet.	NM
Ti_2RhTc	8	-0.7198	4.378	4.378	6.199	0.00	reg. tet.	NM
Ti_2RuTc	1	-0.6242	6.175	6.175	6.175	0.00	reg. cub.	NM
Ti_2TcZn	64	-0.3227	4.415	4.415	6.245	0.00	reg. tet.	NM
V_2CrFe	0	-0.1665	4.070	4.070	5.758	0.00	reg. tet.	NM
V_2CrMn	4	-0.1966	4.055	4.055	5.732	0.00	reg. tet.	NM
V_2CrOs	1	-0.2919	4.171	4.171	5.897	0.00	reg. tet.	NM
V_2CrRe	1	-0.2404	4.187	4.187	5.919	0.00	reg. tet.	NM
V_2CrRu	23	-0.2417	4.157	4.157	5.882	0.00	reg. tet.	NM
V_2MoOs	0	-0.2996	4.279	4.279	6.053	0.00	reg. tet.	NM
V_2MoRe	0	-0.2619	4.295	4.295	6.076	0.00	reg. tet.	NM
V_2MoRu	1	-0.2571	4.271	4.271	6.044	0.00	reg. tet.	NM
V_2OsTc	0	-0.3355	4.250	4.250	6.016	0.00	reg. tet.	NM
V_2RuTc	6	-0.3134	4.242	4.242	6.000	0.00	reg. tet.	NM
Y_2AgRu	56	-0.3423	4.972	4.972	6.997	0.00	reg. tet.	NM
Y_2CuRu	9	-0.3149	4.847	4.847	6.854	0.00	reg. tet.	NM
Y_2IrPd	1	-0.8771	4.909	4.909	6.919	0.00	reg. tet.	NM
Y_2IrRh	0	-0.8355	6.865	6.865	6.865	0.00	reg. cub.	NM

Continued on next page

Table A.1 – continued from previous page

Compounds	ΔE_H	ΔE_f	a	b	c	Spin moment	Structure type	Magnetic type
Zn_2AgAu	0	-0.1550	6.361	6.361	6.361	0.00	reg. cub.	NM
Zn_2AuRh	58	-0.3096	4.118	4.118	6.965	0.00	reg. tet.	NM
Zn_2NiRh	3	-0.2943	5.914	5.914	5.914	0.00	reg. cub.	NM
Zn_2PdRh	5	-0.5089	6.070	6.070	6.070	0.00	reg. cub.	NM
Zn_2PtRh	0	-0.5151	6.083	6.083	6.083	0.00	reg. cub.	NM
Zn_2PtSc	0	-0.6660	4.422	4.422	6.386	0.00	reg. tet.	NM
Zr_2CoTc	13	-0.3501	4.584	4.584	6.483	0.00	reg. tet.	AFM
Zr_2CuOs	0	-0.3408	4.633	4.633	6.555	0.00	reg. tet.	NM
Zr_2CuTc	30	-0.2647	4.635	4.635	6.567	0.00	reg. tet.	NM
Zr_2IrTc	0	-0.6866	6.585	6.585	6.585	0.00	reg. cub.	NM
Zr_2OsRu	0	-0.5849	6.558	6.558	6.558	0.00	reg. cub.	NM
Zr_2OsTc	0	-0.4677	6.567	6.567	6.567	0.00	reg. cub.	NM
Zr_2PdTc	57	-0.5140	6.638	6.638	6.638	0.00	reg. cub.	NM
Zr_2RhTc	27	-0.6344	6.583	6.583	6.583	0.00	reg. cub.	NM
Zr_2RuTc	1	-0.5168	6.557	6.557	6.557	0.00	reg. cub.	NM

Table A.2: Summary of 134 thermodynamically stable half Heusler compounds predicted from large-scale *ab-initio* calculations. Listed properties: convex hull distance ΔE_H (meV/atom), formation energy ΔE_f (eV/atom), lattice parameters a (Å), spin moment (μB/f.u.), and magnetic ordering type.

Compounds	ΔE_H	ΔE_f	a	Spin moment	Magnetic type
AgLaIn	114	-0.32873	6.975	0.00	NM
PtNbAl	47	-0.69019	6.063	0.00	NM
PtAlSc	70	-0.91543	6.221	0.00	NM
PtAlTi	140	-0.77387	6.026	0.00	NM
CoAsCr	100	-0.08787	5.480	1.93	FI
CoAsFe	79	-0.12105	5.509	3.86	FM
CoAsMn	0	-0.21050	5.482	2.93	FM
AsNiCo	50	-0.17077	5.381	0.00	NM
AsPdCo	145	-0.13315	5.653	0.00	AFM
CoAsTi	0	-0.82746	5.598	0.00	NM
CoAsV	0	-0.35239	5.508	0.91	FM
CoAsZr	0	-0.85718	5.834	0.00	NM
FeCrAs	7	-0.12834	5.475	0.94	FI
AsNiCr	142	-0.05364	5.586	2.76	FM
NiCrAs	143	-0.05313	5.557	2.87	FM
AsPdCr	90	-0.14879	5.846	2.80	FM
AsRhCr	143	-0.17700	5.751	2.74	FM
FeAsMn	78	-0.13942	5.500	1.95	FI
AsNiFe	131	-0.06903	5.383	0.00	NM
FeAsTi	98	-0.51342	5.643	0.92	FM

Continued on next page

Table A.2 – continued from previous page

Compounds	ΔE_H	ΔE_f	a	Spin moment	Magnetic type
IrAsTi	0	-0.81250	5.935	0.00	NM
AsMnLi	145	-0.16890	5.570	0.00	AFM
NiMnAs	17	-0.23937	5.566	3.87	FM
AsPdMn	107	-0.06424	5.668	0.00	AFM
PdMnAs	95	-0.19513	5.915	3.87	FM
PtMnAs	78	-0.29927	5.971	3.83	FM
AsRhMn	139	-0.22010	5.719	2.91	FM
RhMnAs	109	-0.25553	5.797	2.99	FM
MnAsV	119	-0.23430	5.559	0.93	FI
NiAsTi	75	-0.57809	5.631	0.00	NM
RhAsTi	0	-0.87441	5.887	0.00	NM
RhAsV	99	-0.36617	5.810	0.93	FM
AuYCd	125	-0.52162	6.782	0.00	NM
AuNaK	102	-0.16325	7.604	0.00	NM
AuLiLa	134	-0.42500	6.965	0.00	NM
AuMgLa	76	-0.51123	7.001	0.00	NM
AuScMg	139	-0.44641	6.509	0.00	NM
AuSnMn	75	-0.07582	6.307	3.84	FM
AuTiSn	138	-0.20895	6.357	0.00	NM
AuZrSn	130	-0.36461	6.530	0.00	NM
PdMnBi	121	-0.09275	6.271	3.89	FM
PtMnBi	65	-0.19085	6.353	3.89	FM

Continued on next page

Table A.2 – continued from previous page

Compounds	ΔE_H	ΔE_f	a	Spin moment	Magnetic type
PdBiZr	127	-0.42580	6.553	0.00	NM
TlSrCa	134	-0.21321	7.889	0.00	NM
CoGeCr	116	-0.03180	5.475	0.00	AFM
CoGeFe	116	-0.05219	5.478	3.02	FM
CoSbFe	93	-0.00946	5.712	3.79	FM
CoNbGa	122	-0.20956	5.717	0.41	FM
CoTaGa	146	-0.17488	5.745	0.57	FM
CoMnGe	150	-0.06688	5.486	0.00	AFM
CoMoGe	120	-0.04147	5.641	0.84	FM
GeCoPt	130	-0.18522	5.666	0.00	NM
CoTiGe	104	-0.47322	5.658	0.84	FM
CoZrGe	109	-0.52049	5.900	0.84	FM
SiIrCo	102	-0.37202	5.474	0.44	FM
CoSbMn	10	-0.10836	5.750	2.96	FM
CoTeMn	30	-0.08469	5.782	3.84	FM
CoScSb	0	-0.64692	6.094	0.00	NM
CoVSb	7	-0.17677	5.777	0.90	FI
CoTeSc	0	-0.79030	6.044	0.00	NM
CoTiSn	12	-0.31975	5.934	0.81	FM
NiSbCr	146	-0.01427	5.807	2.89	FM
PtCrSb	132	-0.16724	6.171	2.99	FM
IrGeFe	100	-0.11233	5.814	2.95	FM

Continued on next page

Table A.2 – continued from previous page

Compounds	ΔE_H	ΔE_f	a	Spin moment	Magnetic type
FeNbGe	29	-0.24515	5.748	0.94	FM
FeTaGe	31	-0.20586	5.754	0.93	FM
FeVGe	88	-0.15325	5.557	0.93	FM
IrFeSn	133	-0.05407	6.063	2.99	FM
FeZrSb	37	-0.43820	6.155	1.00	FM
PtGaTi	72	-0.70806	6.016	0.00	NM
PtGaV	86	-0.45604	5.864	0.00	NM
PtGaZr	82	-0.82101	6.237	0.00	NM
IrGeMn	119	-0.14362	5.864	0.00	AFM
NiMnGe	111	-0.16477	5.560	3.04	FM
GePtMn	126	-0.20758	5.854	3.24	FM
PtMnGe	20	-0.31273	5.940	3.27	FM
RhNbGe	0	-0.57097	5.970	0.00	NM
NiGeV	114	-0.20690	5.570	0.93	FM
PtGeV	94	-0.34749	5.913	0.00	AFM
RhGeV	42	-0.41270	5.796	0.00	NM
PtInHf	71	-0.69404	6.404	0.00	NM
PdHfSb	118	-0.52799	6.376	0.00	NM
PtHfSb	132	-0.66612	6.421	0.00	NM
IrInZr	114	-0.45074	6.420	0.00	NM
NiInZr	131	-0.29211	6.166	0.38	FM
PdInSc	113	-0.59060	6.437	0.00	NM

Continued on next page

Table A.2 – continued from previous page

Compounds	ΔE_H	ΔE_f	a	Spin moment	Magnetic type
PdInTi	144	-0.27804	6.251	0.00	NM
PtInTi	84	-0.53232	6.262	0.00	NM
PtInY	24	-0.85872	6.677	0.00	NM
PtInZr	21	-0.71679	6.445	0.00	NM
ZnSrIn	149	-0.21078	7.072	0.00	NM
IrSbMn	78	-0.20804	6.081	2.99	FM
IrSnMn	150	-0.11198	6.123	0.00	AFM
IrSiNb	18	-0.72022	5.941	0.00	NM
IrTiSb	0	-0.78515	6.167	0.00	NM
IrVSb	147	-0.28808	6.077	0.91	FM
IrVSi	0	-0.61331	5.722	0.00	NM
PtPbLa	14	-0.80879	6.937	0.00	NM
PtLaSn	72	-0.95795	6.858	0.00	NM
PtMgZr	150	-0.60744	6.383	0.00	NM
MnSbNb	84	-0.14636	6.045	1.04	FM
NiMnSb	0	-0.19669	5.797	3.87	FM
NiMnSn	92	-0.09041	5.811	3.23	FM
NiMnTe	50	-0.09424	5.880	0.00	AFM
PdMnSb	25	-0.26554	6.135	3.88	FM
PdMnSn	127	-0.20466	6.135	3.61	FM
PdMnTe	33	-0.19331	6.219	0.00	AFM
PtMnSb	0	-0.38178	6.182	3.84	FM

Continued on next page

Table A.2 – continued from previous page

Compounds	ΔE_H	ΔE_f	a	Spin moment	Magnetic type
SiPtMn	128	-0.41424	5.631	2.67	FM
PtMnSn	52	-0.37008	6.173	3.54	FM
PtMnTe	108	-0.20800	6.286	0.00	AFM
RhMnSb	64	-0.28093	6.050	3.28	FM
RhMnTe	25	-0.23632	6.066	3.82	FM
MnTaSb	83	-0.06953	6.018	0.98	FM
MnVSb	131	-0.03427	5.861	0.95	FI
PtNbSn	142	-0.35207	6.295	0.67	FM
RhNbSb	79	-0.34467	6.220	0.00	NM
RhNbSi	72	-0.63909	5.898	0.00	NM
NiTiSb	0	-0.46592	5.890	0.00	NM
TiNiSb	1	-0.00679	6.077	0.00	NM
NiVSb	126	-0.10508	5.839	1.83	FM
NiYSb	0	-0.89311	6.317	0.00	NM
SbNiY	0	-0.31688	6.541	0.00	NM
YNiSb	0	-0.00048	6.686	0.44	FM
NiZrSb	28	-0.60372	6.119	0.00	NM
NiVSn	141	-0.05190	5.818	0.95	FM
PdTiSb	43	-0.47351	6.234	0.00	NM
PdZrSb	70	-0.63361	6.415	0.00	NM
PtTiSb	50	-0.62092	6.252	0.00	NM
PtZrSb	64	-0.73821	6.449	0.00	NM

Continued on next page

Table A.2 – continued from previous page

Compounds	ΔE_H	ΔE_f	a	Spin moment	Magnetic type
PtTiSi	0	-0.93567	5.896	0.00	NM
RhTiSb	0	-0.81867	6.132	0.00	NM
RhVSb	99	-0.31157	6.049	0.00	AFM
RhVSi	135	-0.52026	5.688	0.00	NM

Table A.3: Summary of 776 thermodynamically stable quaternary Heusler compounds. Listed properties: convex hull distance ΔE_{Hull} (eV/atom), formation energy ΔE_f (eV/atom), lattice parameters a (Å), spin moment (μB/f.u.), and magnetic ordering type of quaternary Heusler structure, including ferromagnetic (FM), ferrimagnetic (FI), antiferromagnetic (AFM), and non-magnetic (NM). ⊡: compounds with stable structure of space group #216, □: compounds with stable structure of space group #215, △: compounds with stable structure of space group #129.

Compounds	ΔE_{Hull}	ΔE_f	a	Spin moment	Magnetic type
AgSnLiMn	0.097	-0.1319	6.494	3.48	FM
AuCuAlMn	0.031	-0.1810	6.171	3.59	FM
BeFeAlTi	0.054	-0.3359	5.776	0.12	FM
AlVMnBe	0.072	-0.1971	5.681	0.00	NM
IrCoAlCr	0.088	-0.3885	5.894	2.99	FM
OsCoAlCr ⊡	0.062	-0.2485	5.863	2.02	FM
RuCoAlCr	0.039	-0.2979	5.834	2.02	FM
IrCoAlFe	0.067	-0.4384	5.883	4.84	FM
FeCoAlMn	0.056	-0.2507	5.661	3.04	FI
FeCoAlNb	0.026	-0.3761	5.930	1.09	FM
AlFeNiCo	0.065	-0.3212	5.700	4.52	FM
RuCoAlFe	0.053	-0.3106	5.838	4.20	FM
FeCoAlTa	0.022	-0.4423	5.921	1.07	FM
CoFeAlV	0.027	-0.3970	5.699	1.03	FM
FeCoAlW	0.098	-0.2180	5.867	2.01	FM
IrCoAlHf	0.003	-0.7975	6.199	0.00	AFM
LiCoAlHf ⊡	0.037	-0.3587	6.086	0.25	FM
PdCoAlHf	0.070	-0.6375	6.227	0.25	FM

Continued on next page

Table A.3 – continued from previous page

Compounds	ΔE_{Hull}	ΔE_f	a	Spin moment	Magnetic type
RhCoAlHf	0.024	-0.7833	6.176	0.00	AFM
IrCoAlMn	0.000	-0.4832	5.891	4.03	FM
IrCoAlNb △	0.035	-0.5434	6.153	1.98	FM
IrCoAlTa	0.026	-0.5959	6.143	1.97	FM
IrCoAlTi	0.000	-0.8280	6.002	0.00	AFM
IrCoAlV	0.039	-0.5631	5.931	2.02	FM
IrCoAlZr	0.016	-0.7193	6.244	0.00	AFM
LiCoAlZr ⊡	0.019	-0.3638	6.132	0.43	FM
CoNiAlMn	0.000	-0.3876	5.736	4.93	FM
OsCoAlMn	0.061	-0.2555	5.856	2.99	FM
PdCoAlMn □	0.074	-0.4192	5.952	4.97	FM
PtCoAlMn	0.000	-0.5549	5.973	4.98	FM
RhCoAlMn	0.058	-0.4971	5.874	4.10	FM
RuCoAlMn	0.046	-0.3351	5.841	3.02	FM
TcCoAlMn ⊡	0.061	-0.2767	5.843	2.14	FM
AlTiMnCo □	0.047	-0.4445	5.835	0.96	FM
NiCoAlNb	0.036	-0.3983	5.966	0.90	FM
OsCoAlNb	0.031	-0.4001	6.122	1.06	FM
RuCoAlNb	0.062	-0.4720	6.093	0.00	AFM
CoNiAlTi	0.028	-0.6110	5.838	0.21	FM
CoNiAlV	0.065	-0.3748	5.736	1.16	FM
NiCoAlZr	0.038	-0.5360	6.090	0.28	FM

Continued on next page

Table A.3 – continued from previous page

Compounds	ΔE_{Hull}	ΔE_f	a	Spin moment	Magnetic type
OsCoAlTa	0.033	-0.4792	6.113	1.05	FM
OsCoAlV	0.027	-0.4252	5.897	1.02	FM
PdCoAlSc	0.085	-0.6764	6.197	0.00	AFM
PdCoAlTi	0.078	-0.6254	6.037	0.00	AFM
PdCoAlZr	0.078	-0.5930	6.292	0.00	AFM
PtCoAlSc	0.094	-0.8311	6.208	0.00	AFM
PtCoAlTi	0.040	-0.7774	6.082	1.82	FM
PtCoAlZn	0.047	-0.5442	5.958	0.00	AFM
RhCoAlTi	0.029	-0.7992	5.982	0.00	AFM
RhCoAlZr	0.030	-0.7154	6.225	0.00	AFM
RuCoAlTa	0.067	-0.5410	6.087	0.00	AFM
RuCoAlV	0.040	-0.4843	5.871	1.01	FM
TcCoAlTi	0.068	-0.5029	5.989	0.32	FM
TcCoAlW	0.094	-0.2307	6.043	0.94	FM
AlTiVCo	0.081	-0.3475	6.015	2.65	FM
FeCrAlHf ⊡	0.060	-0.2359	6.139	2.91	FM
OsFeAlCr	0.036	-0.1760	5.844	0.00	AFM
RuFeAlCr	0.096	-0.2355	5.828	0.00	AFM
AlTiCrFe ⊡	0.036	-0.3102	5.950	2.87	FM
CrFeAlV	0.072	-0.2112	5.817	1.94	FI
FeCrAlW	0.074	-0.0921	5.917	1.00	FI
IrCrAlHf ⊡	0.044	-0.5350	6.276	1.87	FM

Continued on next page

Table A.3 – continued from previous page

Compounds	ΔE_{Hull}	ΔE_f	a	Spin moment	Magnetic type
OsCrAlHf ⊡	0.064	-0.3916	6.301	2.83	FM
RuCrAlHf ⊡	0.064	-0.4578	6.290	2.84	FM
IrCrAlMn	0.081	-0.3919	5.998	1.07	FI
IrCrAlTa	0.100	-0.4403	6.168	0.93	FM
IrCrAlTi ⊡	0.045	-0.6139	6.092	1.85	FM
IrCrAlV	0.066	-0.4578	5.976	0.94	FI
MnCrAlMo	0.074	-0.1010	5.949	1.94	FI
MnCrAlNb	0.034	-0.1806	6.067	2.95	FM
OsMnAlCr	0.061	-0.1613	5.848	0.03	FI
MnCrAlRe	0.059	-0.1170	5.876	1.08	FM
MnCrAlTa	0.030	-0.2082	6.056	2.91	FM
TcMnAlCr	0.085	-0.1479	5.861	0.99	FI
AlTiCrMn	0.094	-0.1882	5.986	1.89	FI
MnCrAlV	0.019	-0.2131	5.881	2.88	FI
MnCrAlW	0.047	-0.1104	5.953	1.95	FI
OsCrAlNb ⊡	0.051	-0.2637	6.190	1.89	FM
ReCrAlNb ⊡	0.083	-0.1603	6.248	2.74	FM
TcCrAlNb ⊡	0.030	-0.2580	6.231	2.76	FM
RuNiAlCr ⊡	0.086	-0.2965	5.884	2.72	FM
TcNiAlCr	0.092	-0.2642	5.873	1.98	FM
OsCrAlTa ⊡	0.058	-0.3204	6.181	1.87	FM
OsCrAlTi ⊡	0.019	-0.4497	6.118	2.76	FM

Continued on next page

Table A.3 – continued from previous page

Compounds	ΔE_{Hull}	ΔE_f	a	Spin moment	Magnetic type
OsCrAlV ⊡	0.054	-0.3048	5.997	1.83	FI
OsCrAlW	0.071	-0.1494	6.090	0.94	FI
OsCrAlZr ⊡	0.080	-0.3367	6.341	2.82	FM
ReCrAlTa ⊡	0.085	-0.2035	6.243	2.73	FM
ReCrAlV	0.089	-0.1668	6.050	2.54	FI
ReCrAlW	0.074	-0.0736	6.140	0.00	AFM
RhCrAlTi	0.088	-0.5468	6.084	1.87	FM
RuCrAlTi ⊡	0.016	-0.4992	6.110	2.77	FM
RuCrAlV	0.083	-0.3376	5.985	1.83	FI
RuCrAlZr ⊡	0.063	-0.4154	6.333	2.83	FM
TcCrAlTa ⊡	0.039	-0.2949	6.223	2.74	FM
TcCrAlTi	0.097	-0.2840	6.141	2.17	FM
TcCrAlV	0.031	-0.2478	6.042	2.59	FI
TcCrAlW	0.060	-0.1467	6.122	1.86	FI
FeCuAlHf	0.085	-0.2660	6.117	0.00	AFM
AlMnFeCu □	0.098	-0.0830	5.798	0.00	AFM
CuFeAlTi	0.079	-0.3151	5.902	0.00	AFM
LiCuAlMn	0.093	-0.0905	5.929	3.67	FM
AlMnCuNi	0.075	-0.2596	5.819	3.63	FM
PtCuAlMn ⊡	0.059	-0.4653	6.058	3.63	FM
MnFeAlHf	0.051	-0.2889	6.054	2.03	FM
NiFeAlHf	0.061	-0.4796	6.043	0.00	AFM

Continued on next page

Table A.3 – continued from previous page

Compounds	ΔE_{Hull}	ΔE_f	a	Spin moment	Magnetic type
OsFeAlHf	0.078	-0.4421	6.183	0.90	FM
PdFeAlHf △	0.080	-0.5447	6.241	0.00	AFM
PtFeAlHf	0.075	-0.7117	6.253	0.00	AFM
RuFeAlHf	0.060	-0.5401	6.160	0.86	FM
TcFeAlHf	0.091	-0.3265	6.202	1.76	FM
IrFeAlMn	0.089	-0.3839	5.874	2.95	FM
IrFeAlNb	0.049	-0.5074	6.128	0.00	AFM
IrFeAlSc	0.100	-0.6018	6.145	0.86	FM
IrFeAlTa	0.030	-0.5825	6.122	0.00	AFM
IrFeAlV	0.059	-0.5295	5.912	0.00	AFM
LiFeAlNb ⊡	0.079	-0.1987	5.973	0.72	FM
MnFeAlNb	0.037	-0.2797	5.943	1.03	FM
FeNiAlMn	0.055	-0.2799	5.708	4.07	FM
OsFeAlMn	0.013	-0.2091	5.843	0.00	AFM
PtFeAlMn	0.088	-0.4363	5.935	4.04	FM
MnFeAlRe	0.051	-0.1490	5.810	0.00	AFM
RuFeAlMn	0.058	-0.2733	5.834	0.00	AFM
MnFeAlTa	0.036	-0.3405	5.936	1.01	FM
TcFeAlMn ⊡	0.071	-0.1780	5.863	3.09	FM
AlTiFeMn	0.024	-0.3857	5.835	1.99	FM
MnFeAlV	0.028	-0.3399	5.724	1.02	FI
MnFeAlZr	0.073	-0.2385	6.109	2.06	FM

Continued on next page

Table A.3 – continued from previous page

Compounds	ΔE_{Hull}	ΔE_f	a	Spin moment	Magnetic type
OsFeAlMo	0.064	-0.1642	6.032	0.00	AFM
NiFeAlNb	0.073	-0.3388	5.978	0.00	AFM
TcFeAlNb	0.063	-0.3187	6.110	0.91	FM
RuNiAlFe	0.065	-0.3204	5.864	0.00	AFM
NiFeAlTa	0.084	-0.3826	5.977	0.00	AFM
AlTiFeNi $^{\square}$	0.021	-0.5386	5.832	0.00	AFM
NiFeAlV	0.088	-0.3446	5.734	1.98	FM
NiFeAlZr	0.093	-0.4229	6.091	0.00	AFM
OsFeAlTi	0.018	-0.5294	5.987	0.92	FM
OsFeAlW	0.033	-0.1962	6.039	0.00	AFM
OsFeAlZr	0.089	-0.3586	6.220	0.91	FM
PtFeAlTi	0.004	-0.7455	6.058	0.00	AFM
RhFeAlTa	0.089	-0.5514	6.097	0.00	AFM
RuFeAlTi	0.016	-0.6072	5.965	0.88	FM
RuFeAlW	0.094	-0.2469	6.012	0.00	AFM
RuFeAlZr	0.065	-0.4682	6.194	0.87	FM
TcFeAlTa	0.060	-0.3863	6.102	0.89	FM
TcFeAlTi	0.073	-0.4039	6.024	1.70	FM
TcFeAlV	0.053	-0.3516	5.898	0.95	FI
AlTiFeZn	0.093	-0.2823	5.985	0.00	AFM
IrMnAlHf	0.004	-0.6243	6.209	0.95	FM
OsMnAlHf	0.092	-0.3960	6.231	1.97	FM

Continued on next page

Table A.3 – continued from previous page

Compounds	ΔE_{Hull}	ΔE_f	a	Spin moment	Magnetic type
RuMnAlHf	0.090	-0.4756	6.213	1.97	FM
IrMnAlMg	0.095	-0.3817	6.160	3.29	FM
IrMnAlTi	0.000	-0.7097	6.015	0.96	FM
IrMnAlZr	0.092	-0.5474	6.251	0.97	FM
LiMnAlMo ⊡	0.091	-0.0819	5.910	0.84	FI
LiNiAlMn ⊡	0.087	-0.2479	5.762	3.18	FM
PtMnAlLi	0.099	-0.5274	5.996	3.32	FM
OsMnAlNb	0.012	-0.3359	6.128	1.00	FM
ReMnAlNb	0.079	-0.1889	6.178	1.97	FM
RuMnAlNb	0.055	-0.3977	6.102	0.99	FM
TcMnAlNb	0.021	-0.2972	6.159	1.97	FM
PdNiAlMn	0.056	-0.4598	5.992	4.07	FM
PtNiAlMn	0.000	-0.5673	6.003	4.13	FM
RhNiAlMn	0.053	-0.5324	5.922	4.39	FM
RuNiAlMn ⊡	0.032	-0.3722	5.886	0.00	AFM
TcNiAlMn	0.094	-0.2663	5.891	0.00	AFM
OsMnAlSc	0.097	-0.3011	6.256	3.03	FM
OsMnAlTa	0.010	-0.4151	6.119	0.97	FM
AlTiOsMn ⊡	0.020	-0.4827	6.046	1.92	FM
OsMnAlV	0.003	-0.3913	5.920	0.99	FI
OsMnAlZr	0.092	-0.3269	6.272	1.99	FM
ReMnAlTa	0.096	-0.2448	6.171	1.93	FM

Continued on next page

Table A.3 – continued from previous page

Compounds	ΔE_{Hull}	ΔE_f	a	Spin moment	Magnetic type
ReMnAlTi	0.075	-0.2815	6.123	2.83	FM
ReMnAlV	0.074	-0.2357	5.979	1.89	FI
ReMnAlW	0.060	-0.1423	6.078	0.98	FI
RhMnAlTi	0.046	-0.6535	6.004	0.96	FM
RuMnAlSc	0.054	-0.4090	6.233	2.97	FM
RuMnAlTa	0.059	-0.4654	6.095	0.96	FM
RuMnAlTi	0.027	-0.5447	6.030	1.92	FM
RuMnAlV	0.048	-0.4345	5.901	0.98	FI
RuMnAlZn	0.088	-0.2509	6.017	3.20	FM
RuMnAlZr	0.077	-0.4188	6.257	2.01	FM
TcMnAlTa	0.037	-0.3477	6.150	1.93	FM
TcMnAlTi	0.012	-0.4003	6.107	2.83	FM
TcMnAlV	0.019	-0.3267	5.971	1.89	FI
TcMnAlW	0.035	-0.2268	6.057	0.97	FI
TcMnAlZr ⊡	0.057	-0.2919	6.322	2.95	FM
RuNiAlV	0.086	-0.4512	5.917	1.66	FM
AsMnCoCr	0.092	-0.0712	5.776	2.96	FI
AsMnCoFe ⊡	0.068	-0.1088	5.705	4.95	FM
RuCoAsMn	0.075	-0.0877	5.850	4.86	FM
AsMnFeCr	0.098	-0.0586	5.751	1.98	FI
RuCrAsMn ⊡	0.065	-0.0934	5.939	1.91	FI
TcCrAsMn ⊡	0.077	-0.0609	5.960	1.00	FI

Continued on next page

Table A.3 – continued from previous page

Compounds	ΔE_{Hull}	ΔE_f	a	Spin moment	Magnetic type
RuFeAsMn	0.099	-0.0589	5.880	3.93	FM
LiMnAsPd	0.096	-0.3500	6.138	0.00	AFM
MnZnAuCo △	0.098	-0.0168	6.081	4.95	FM
MnGaAuCu	0.064	-0.0590	6.214	3.67	FM
MnCuAuRh	0.062	-0.0572	6.144	4.17	FM
MnZnAuCu	0.056	-0.0524	6.171	3.70	FM
AuGaLiMn	0.079	-0.2549	6.212	3.40	FM
AuGeLiMn	0.099	-0.2196	6.284	3.49	FM
LiMnSnAu	0.095	-0.2559	6.475	3.49	FM
CoMnGaBe	0.092	-0.1501	5.642	3.11	FM
RuCoGaBe	0.087	-0.2185	5.708	0.55	FM
NiCoGeBe	0.070	-0.2830	5.546	0.68	FM
SiBeMnCo	0.087	-0.3868	5.414	1.26	FM
NiCoSiBe	0.037	-0.5299	5.385	0.53	FM
BeSiTcCo	0.100	-0.3729	5.607	0.43	FM
IrCrGaBe	0.072	-0.2791	5.868	2.83	FM
IrCrSiBe ⊡	0.082	-0.4217	5.739	2.45	FM
RuCrSiBe ⊡	0.097	-0.3460	5.726	2.76	FM
NiFeGeBe	0.086	-0.2134	5.532	0.00	AFM
BeGeRuFe	0.083	-0.1722	5.705	1.07	FM
FeMnSiBe □	0.054	-0.3207	5.446	2.35	FM
OsFeSiBe	0.026	-0.3339	5.605	0.99	FM

Continued on next page

Table A.3 – continued from previous page

Compounds	ΔE_{Hull}	ΔE_f	a	Spin moment	Magnetic type
RuFeSiBe	0.028	-0.4454	5.579	1.00	FM
BeSiTcFe	0.098	-0.2745	5.616	1.61	FM
IrMnGaBe △	0.094	-0.2961	5.855	3.03	FM
RhMnGaBe	0.092	-0.3437	5.846	3.10	FM
RuMnGaBe	0.063	-0.2059	5.818	3.06	FM
IrMnSiBe	0.042	-0.4791	5.646	1.33	FM
OsMnSiBe ⊡	0.057	-0.2859	5.622	0.00	AFM
RhMnSiBe	0.097	-0.4878	5.627	1.39	FM
BeSiRuMn	0.047	-0.3988	5.659	2.32	FM
BeSiTcMn	0.087	-0.2745	5.720	2.75	FM
LiMnInCd	0.096	-0.0524	6.584	3.44	FM
LiMnSnCd	0.098	-0.0919	6.609	0.00	AFM
ScYCdTl	0.010	-0.3313	7.339	0.00	NM
GaCrCoFe	0.097	-0.0700	5.706	1.96	FI
GeCrCoFe	0.083	-0.0749	5.717	2.96	FM
SiCrCoFe	0.075	-0.2932	5.590	2.99	FM
CrGaIrCo	0.016	-0.2022	5.923	2.97	FM
GaMnCoCr □	0.071	-0.0865	5.700	1.14	FI
GaCrCoNi	0.098	-0.1185	5.720	3.87	FM
CrGaOsCo	0.095	-0.0525	5.887	2.01	FM
CrGaPtCo	0.069	-0.2247	6.005	3.92	FM
RuCoGaCr	0.022	-0.1448	5.867	2.00	FM

Continued on next page

Table A.3 – continued from previous page

Compounds	ΔE_{Hull}	ΔE_f	a	Spin moment	Magnetic type
CrGaTcCo	0.079	-0.0646	5.884	1.08	FM
CoCrGaV □	0.083	-0.1284	5.802	0.96	FI
IrCoGeCr △	0.082	-0.1109	5.963	3.89	FM
GeMnCoCr	0.040	-0.1521	5.785	2.01	FI
CrGeRuCo	0.050	-0.1204	5.886	2.95	FM
TcCoGeCr	0.039	-0.0992	5.892	2.02	FM
CrZnIrCo △	0.088	-0.0409	5.876	2.11	FM
SiMnCoCr	0.065	-0.3342	5.635	2.03	FI
CrSiRuCo	0.064	-0.3195	5.787	2.97	FM
TcCoSiCr	0.034	-0.3138	5.791	2.00	FM
GaMnCuCo	0.083	-0.0851	5.828	4.13	FM
GaScCoCu	0.079	-0.3369	6.082	0.32	FM
GeCuNiCo	0.045	-0.1333	5.701	0.00	AFM
CuCoZnHf	0.077	-0.1894	6.094	0.29	FM
InScCoCu □	0.085	-0.2283	6.312	0.00	AFM
CuCoInZr	0.048	-0.2033	6.350	0.00	AFM
CoNiSiCu	0.087	-0.2969	5.576	0.00	AFM
CoNiSnCu	0.099	-0.0588	5.936	0.00	AFM
CuCoZnTi	0.079	-0.1971	5.884	0.26	FM
ZrZnCuCo	0.087	-0.1678	6.145	0.00	AFM
IrCoGaFe	0.000	-0.2491	5.925	4.88	FM
GaFeCoLi ⊡	0.070	-0.1645	5.702	3.08	FM

Continued on next page

Table A.3 – continued from previous page

Compounds	ΔE_{Hull}	ΔE_f	a	Spin moment	Magnetic type
GaMnCoFe	0.050	-0.1318	5.690	3.01	FI
FeCoGaNb	0.026	-0.2654	5.938	0.00	AFM
GaFeNiCo	0.060	-0.2009	5.728	4.59	FM
FeGaPtCo △	0.080	-0.2500	5.984	4.73	FM
RhCoGaFe □	0.063	-0.3147	5.896	4.93	FM
FeGaRuCo	0.024	-0.1713	5.873	4.34	FM
TaGaFeCo	0.022	-0.3158	5.930	0.00	AFM
CoFeGaV	0.027	-0.2748	5.718	0.00	AFM
FeGeIrCo	0.095	-0.0964	5.934	4.82	FM
GeFeCoLi ⊡	0.040	-0.1884	5.721	3.88	FM
GeMnCoFe ⊡	0.013	-0.1795	5.707	3.99	FM
GeFeNiCo	0.083	-0.1306	5.730	3.90	FM
FeGeRuCo	0.029	-0.1491	5.881	4.74	FM
TcCoGeFe ⊡	0.065	-0.0792	5.888	3.99	FM
GeTiFeCo	0.024	-0.4885	5.805	1.05	FM
CoFeGeV	0.049	-0.2543	5.740	2.02	FM
FeCoSnHf	0.023	-0.3327	6.216	0.00	AFM
FeCoInNb	0.094	-0.0166	6.145	0.00	AFM
FeSiIrCo	0.074	-0.3032	5.813	4.69	FM
FeZnIrCo	0.031	-0.0952	5.885	4.61	FM
CoFeSiLi	0.093	-0.2730	5.473	1.30	FM
SbMnCoFe	0.058	-0.0384	5.948	4.99	FM

Continued on next page

Table A.3 – continued from previous page

Compounds	ΔE_{Hull}	ΔE_f	a	Spin moment	Magnetic type
SiMnCoFe	0.007	-0.3898	5.574	4.01	FM
FeCoSnMn	0.076	-0.0077	5.954	4.07	FM
ZnFeNiCo	0.072	-0.0920	5.708	4.84	FM
RhCoZnFe	0.072	-0.1555	5.868	4.65	FM
RuCoSiFe	0.017	-0.3476	5.770	4.65	FM
RuCoSnFe	0.098	-0.0307	6.108	4.89	FM
FeSiTcCo	0.058	-0.2854	5.778	3.83	FM
CoFeSiTi	0.026	-0.6739	5.693	1.05	FM
CoFeSiV	0.008	-0.4685	5.611	2.00	FM
TaSnFeCo	0.074	-0.1677	6.156	2.07	FM
SnTiFeCo	0.022	-0.3444	6.044	0.00	AFM
SnVFeCo	0.084	-0.0743	5.982	2.05	FM
ZrSnFeCo	0.078	-0.3057	6.254	0.00	AFM
CoFeZnTi	0.080	-0.2242	5.793	0.93	FM
HfGaIrCo	0.013	-0.6420	6.218	0.00	AFM
LiCoGaHf	0.079	-0.3458	6.064	0.64	FM
PdCoGaHf $^{\triangle}$	0.094	-0.5417	6.236	0.00	AFM
HfGaPtCo $^{\triangle}$	0.098	-0.6377	6.262	0.00	AFM
RhCoGaHf	0.042	-0.6712	6.184	0.00	AFM
MnGaIrCo	0.000	-0.2995	5.917	4.03	FM
IrCoGaNb $^{\triangle}$	0.036	-0.3787	6.164	1.98	FM
IrCoGaNi	0.088	-0.1438	5.871	2.25	FM

Continued on next page

Table A.3 – continued from previous page

Compounds	ΔE_{Hull}	ΔE_f	a	Spin moment	Magnetic type
TaGaIrCo △	0.037	-0.4201	6.158	1.98	FM
TiGaIrCo	0.010	-0.6575	6.017	0.00	AFM
IrCoGaV	0.032	-0.3736	5.948	2.00	FM
IrCoGaZr	0.050	-0.5775	6.265	0.00	AFM
GaTiLiCo ⊡	0.047	-0.3741	5.867	0.75	FM
LiCoGaZr ⊡	0.056	-0.3637	6.111	0.77	FM
CoNiGaMn	0.018	-0.2524	5.685	4.82	FM
MnGaOsCo	0.094	-0.0777	5.883	2.99	FM
PdCoGaMn □	0.066	-0.2936	5.989	4.94	FM
PtCoGaMn	0.012	-0.3796	6.003	4.94	FM
MnGaRhCo	0.032	-0.3547	5.901	4.09	FM
RuCoGaMn	0.050	-0.1953	5.863	3.02	FM
TcCoGaMn ⊡	0.008	-0.1494	5.877	2.14	FM
CoMnGaTi	0.053	-0.3654	5.843	0.96	FM
CoMnZnGa	0.064	-0.1017	5.878	3.34	FM
NiCoGaNb	0.039	-0.2967	5.965	0.87	FM
NbGaOsCo	0.039	-0.2218	6.138	0.00	AFM
RhCoGaNb △	0.041	-0.3938	6.144	1.96	FM
NbGaRuCo	0.069	-0.3351	6.103	0.00	AFM
GaVCoNi	0.054	-0.2653	5.764	1.12	FM
NiCoGaZr	0.035	-0.4610	6.090	0.28	FM
TaGaOsCo	0.041	-0.2881	6.127	0.00	AFM

Continued on next page

Table A.3 – continued from previous page

Compounds	ΔE_{Hull}	ΔE_f	a	Spin moment	Magnetic type
VGaOsCo	0.034	-0.2288	5.925	1.02	FM
PdCoGaSc	0.061	-0.5989	6.203	0.00	AFM
TiGaPdCo △	0.082	-0.5225	6.057	0.00	AFM
ZrGaPdCo △	0.098	-0.5089	6.287	0.00	AFM
ScGaPtCo	0.055	-0.7066	6.225	0.00	AFM
TiGaPtCo △	0.052	-0.6305	6.092	1.85	FM
PtCoGaZn	0.073	-0.3548	5.998	0.00	AFM
RhCoGaTa △	0.051	-0.4248	6.108	1.80	FM
TiGaRhCo	0.041	-0.6773	5.986	0.00	AFM
VGaRhCo △	0.062	-0.3809	5.933	2.00	FM
ZrGaRhCo	0.040	-0.6171	6.241	0.00	AFM
TaGaRuCo	0.073	-0.3903	6.091	0.00	AFM
VGaRuCo	0.051	-0.3308	5.894	0.00	AFM
ZnGaRuCo	0.074	-0.1247	5.913	0.57	FM
TcCoGaTi	0.045	-0.3848	6.014	0.59	FM
TcCoGaW	0.099	-0.0540	6.064	0.99	FM
IrCoGeMg	0.036	-0.2537	6.007	0.00	AFM
MnGeIrCo	0.007	-0.2387	5.969	4.91	FM
IrCoGeSc	0.089	-0.5495	6.154	0.00	AFM
IrCoGeTi △	0.065	-0.5310	6.049	2.00	FM
ZnGeIrCo	0.075	-0.1537	5.950	0.00	AFM
GeMnCoLi ⊡	0.052	-0.2113	5.716	2.96	FM

Continued on next page

Table A.3 – continued from previous page

Compounds	ΔE_{Hull}	ΔE_f	a	Spin moment	Magnetic type
PtCoGeLi	0.030	-0.4103	5.862	0.00	AFM
LiGeRuCo	0.053	-0.1678	5.778	0.57	FM
CoNiGeMg	0.094	-0.2145	5.876	0.92	FM
GeMnNiCo	0.068	-0.1856	5.674	4.51	FM
MnGeOsCo △	0.097	-0.0614	5.911	3.96	FM
RhCoGeMn ⊡	0.030	-0.3235	5.931	4.94	FM
RuCoGeMn	0.045	-0.2156	5.889	3.99	FM
MnGeTcCo	0.055	-0.1545	5.895	2.98	FM
GeVMnCo	0.078	-0.2405	5.729	0.99	FM
GeZnCoNi	0.070	-0.1734	5.782	0.75	FM
TiGeOsCo	0.093	-0.3882	6.010	0.00	AFM
RhCoGeTi △	0.035	-0.5854	6.017	1.91	FM
RuCoGeTi	0.078	-0.5409	5.963	0.00	AFM
CoRuVGe	0.058	-0.2680	5.913	1.99	FM
VGeTcCo	0.072	-0.2370	5.926	1.00	FM
IrCoInHf	0.026	-0.4827	6.402	0.00	AFM
NiCoInHf	0.028	-0.3377	6.250	0.00	AFM
PdCoInHf	0.066	-0.4380	6.427	0.00	AFM
PtCoInHf	0.085	-0.5288	6.456	0.00	AFM
RhCoInHf	0.038	-0.5089	6.311	0.00	AFM
IrCoSnHf	0.049	-0.5189	6.421	1.95	FM
NiCoZnHf	0.029	-0.3618	6.025	0.00	NM

Continued on next page

Table A.3 – continued from previous page

Compounds	ΔE_{Hull}	ΔE_f	a	Spin moment	Magnetic type
PdCoZnHf △	0.061	-0.4465	6.216	0.00	AFM
PtCoZnHf △	0.021	-0.5956	6.244	0.00	AFM
HfSnRhCo	0.037	-0.5762	6.381	1.50	FM
RuCoSnHf	0.067	-0.4720	6.363	0.00	AFM
IrCoInMn	0.097	-0.0216	6.164	4.31	FM
NbInIrCo	0.095	-0.1918	6.323	1.99	FM
TiInIrCo	0.040	-0.4070	6.243	0.00	AFM
IrCoInZr	0.001	-0.4411	6.446	0.00	AFM
ZrInLiCo	0.084	-0.2519	6.348	0.85	FM
MgInCoNi	0.063	-0.0727	6.140	0.00	AFM
RhCoInMg	0.080	-0.2280	6.251	0.27	FM
CoNiInMn	0.093	-0.0165	5.925	4.96	FM
MnInPtCo	0.084	-0.1912	6.235	5.02	FM
NbInNiCo □	0.095	-0.0990	6.124	0.93	FM
NbInRhCo △	0.081	-0.2256	6.324	1.96	FM
RuCoInNb	0.088	-0.1168	6.293	0.00	AFM
InScNiCo	0.038	-0.3376	6.238	0.00	AFM
InTiCoNi	0.034	-0.2916	6.099	0.00	AFM
ScInPdCo	0.064	-0.5044	6.420	0.00	AFM
ZrInPdCo	0.063	-0.4279	6.484	0.00	AFM
ScInPtCo	0.089	-0.5984	6.438	0.00	AFM
InTiPtCo	0.092	-0.4512	6.290	1.83	FM

Continued on next page

Table A.3 – continued from previous page

Compounds	ΔE_{Hull}	ΔE_f	a	Spin moment	Magnetic type
PtCoInZr	0.058	-0.5185	6.507	0.00	AFM
TiInRhCo	0.031	-0.4497	6.216	0.00	AFM
InZrRhCo	0.023	-0.4877	6.412	0.00	AFM
MgSnIrCo	0.055	-0.2460	6.254	0.00	AFM
MnSiIrCo ⊡	0.004	-0.4366	5.847	4.92	FM
IrCoSnMn	0.009	-0.1759	6.173	4.93	FM
MnZnIrCo	0.052	-0.0915	5.875	3.18	FM
IrCoZnNb	0.011	-0.3012	6.113	0.00	AFM
ScSnIrCo	0.025	-0.5714	6.370	0.00	AFM
IrCoSiTi	0.054	-0.7055	5.955	2.00	FM
ZnSiIrCo	0.085	-0.3499	5.832	0.00	AFM
IrCoSnTi	0.045	-0.4802	6.261	2.00	FM
IrCoSnZr	0.080	-0.4996	6.462	1.99	FM
TaZnIrCo	0.003	-0.3751	6.111	0.00	AFM
VZnIrCo	0.046	-0.2630	5.916	0.00	AFM
SbMnCoLi ⊡	0.100	-0.1793	6.015	3.90	FM
SiMnCoLi	0.067	-0.3001	5.607	3.01	FM
SnMnCoLi	0.082	-0.1453	6.008	2.96	FI
LiSiOsCo	0.096	-0.2324	5.660	0.57	FM
RuCoLiSi	0.011	-0.3745	5.641	0.52	FM
CoNiSnMg	0.049	-0.1952	6.136	0.90	FM
SbMnNiCo	0.090	-0.0728	6.000	4.34	FM

Continued on next page

Table A.3 – continued from previous page

Compounds	ΔE_{Hull}	ΔE_f	a	Spin moment	Magnetic type
SiMnNiCo	0.075	-0.3673	5.636	4.53	FM
SnMnNiCo	0.072	-0.1097	5.900	4.65	FM
CoNiZnMn	0.042	-0.0959	5.712	4.15	FM
MnSiOsCo	0.060	-0.2935	5.801	3.96	FM
MnSnPdCo	0.097	-0.1991	6.233	4.95	FM
PtCoSnMn	0.100	-0.2208	6.260	5.34	FM
PtCoZnMn	0.051	-0.2401	5.956	4.29	FM
RhCoSbMn	0.079	-0.1818	6.180	5.63	FM
MnSiRhCo ⊡	0.036	-0.4839	5.821	4.96	FM
MnSnRhCo ⊡	0.023	-0.2797	6.147	4.96	FM
RhCoZnMn	0.085	-0.1200	5.876	3.29	FM
RuCoSbMn	0.024	-0.0860	6.133	4.93	FM
MnSiRuCo	0.048	-0.4088	5.781	3.98	FM
RuCoSnMn	0.042	-0.0936	6.119	4.08	FM
MnSiTcCo	0.045	-0.3605	5.787	2.98	FM
CoMnSiV □	0.028	-0.4703	5.619	0.97	FM
NiCoZnNb	0.045	-0.1758	5.943	0.00	AFM
PtCoZnNb △	0.076	-0.3026	6.184	1.90	FM
RhCoZnNb	0.051	-0.2979	6.092	0.00	AFM
RuCoSnNb	0.073	-0.2119	6.313	1.98	FM
SnZnCoNi	0.090	-0.1221	6.023	0.70	FM
NiCoZnTa	0.044	-0.2194	5.930	0.28	FM

Continued on next page

Table A.3 – continued from previous page

Compounds	ΔE_{Hull}	ΔE_f	a	Spin moment	Magnetic type
TiZnCoNi	0.025	-0.3721	5.813	0.00	AFM
ZnVCoNi	0.092	-0.1366	5.736	1.70	FM
ZrZnNiCo	0.032	-0.3154	6.070	0.00	AFM
TiSiOsCo	0.082	-0.5980	5.911	0.00	AFM
VSiOsCo	0.060	-0.3824	5.850	1.98	FM
ScSnPdCo	0.070	-0.5976	6.414	0.00	AFM
PdCoSnTi $^{\triangle}$	0.093	-0.4338	6.276	0.00	AFM
PdCoZnTi $^{\triangle}$	0.077	-0.4192	6.024	0.00	AFM
ZrZnPdCo $^{\triangle}$	0.065	-0.4041	6.266	0.00	AFM
TiZnPtCo $^{\triangle}$	0.003	-0.5682	6.049	0.00	AFM
ZrZnPtCo $^{\triangle}$	0.034	-0.5406	6.301	0.00	AFM
RhCoSnSc	0.022	-0.6572	6.346	1.08	FM
RhCoZnSc	0.080	-0.4644	6.133	0.00	NM
TiSiRhCo $^{\triangle}$	0.057	-0.7260	5.926	1.88	FM
RhCoSnTi	0.052	-0.5398	6.240	1.95	FM
ZnSnRhCo	0.064	-0.2598	6.150	0.00	AFM
RhCoSnZr	0.044	-0.5684	6.425	1.86	FM
RhCoZnTa	0.054	-0.3601	6.076	0.00	AFM
VZnRhCo	0.065	-0.2545	5.876	0.00	AFM
RuCoSiTi	0.077	-0.7179	5.879	0.00	AFM
RuCoSiV	0.044	-0.4711	5.815	1.99	FM
TaSnRuCo	0.086	-0.2262	6.319	1.98	FM

Continued on next page

Table A.3 – continued from previous page

Compounds	ΔE_{Hull}	ΔE_f	a	Spin moment	Magnetic type
RuCoSnTi	0.067	-0.4452	6.201	0.00	AFM
RuCoSnZr	0.070	-0.4404	6.403	0.00	AFM
VSiTcCo	0.040	-0.4549	5.813	0.97	FM
PtCrGaCu	0.089	-0.2205	6.066	3.04	FM
CrGaIrFe	0.075	-0.1340	5.920	0.00	AFM
CrGaRuFe	0.075	-0.0833	5.856	0.96	FI
CrGaTcFe	0.090	-0.0037	5.873	0.00	AFM
GaTiCrFe ⊡	0.058	-0.2609	5.943	2.86	FM
VGaCrFe	0.074	-0.1347	5.820	1.94	FI
MnFeGeCr	0.070	-0.0630	5.694	0.95	FI
CrGeRuFe	0.079	-0.0900	5.873	0.00	AFM
CrGeTcFe	0.063	-0.0428	5.878	1.00	FI
VGeCrFe	0.076	-0.1715	5.779	0.99	FI
FeMnSiCr	0.042	-0.3136	5.571	0.00	AFM
OsFeSiCr	0.085	-0.2188	5.791	0.00	AFM
CrSiRuFe	0.076	-0.3005	5.769	0.00	AFM
CrSiTcFe	0.045	-0.2720	5.771	0.00	AFM
SiVCrFe	0.053	-0.3905	5.675	0.98	FI
RuCrGaHf ⊡	0.093	-0.3761	6.288	2.84	FM
IrCrGaMn	0.000	-0.2607	6.019	1.07	FI
IrCrGaTa	0.082	-0.2798	6.179	0.92	FM
IrCrGaTi ⊡	0.039	-0.4857	6.091	1.86	FM

Continued on next page

Table A.3 – continued from previous page

Compounds	ΔE_{Hull}	ΔE_f	a	Spin moment	Magnetic type
VGaIrCr	0.054	-0.3010	5.990	0.94	FI
IrCrGaZn	0.045	-0.2100	6.076	2.92	FM
NbGaMnCr	0.061	-0.1152	6.066	2.95	FM
GaMnNiCr	0.095	-0.1103	5.724	1.96	FI
MnCrGaTa	0.052	-0.1266	6.050	2.90	FM
CrGaTcMn	0.025	-0.0302	5.933	0.96	FI
GaVCrMn	0.037	-0.1548	5.877	2.87	FI
TcCrGaMo	0.074	-0.0162	6.164	1.89	FI
OsCrGaNb ⊡	0.071	-0.1206	6.196	1.91	FM
NbGaTcCr ⊡	0.050	-0.1704	6.228	2.75	FM
PtNiGaCr	0.083	-0.2537	6.037	0.00	AFM
CrGaRuNi	0.079	-0.1490	5.876	2.76	FM
TcNiGaCr	0.083	-0.1246	5.925	1.95	FM
TaGaOsCr ⊡	0.085	-0.1647	6.190	1.88	FM
OsCrGaTi ⊡	0.088	-0.3304	6.123	2.76	FM
VGaOsCr ⊡	0.077	-0.1585	6.007	1.83	FI
RhCrGaZn	0.090	-0.2818	6.067	2.98	FM
RuCrGaTi ⊡	0.038	-0.4223	6.108	2.76	FM
RuCrGaV	0.058	-0.2361	5.996	1.84	FI
RuCrGaZr ⊡	0.084	-0.3457	6.319	2.83	FM
TcCrGaTi	0.099	-0.2146	6.131	1.95	FM
TcCrGaV	0.069	-0.1638	6.042	2.59	FI

Continued on next page

Table A.3 – continued from previous page

Compounds	ΔE_{Hull}	ΔE_f	a	Spin moment	Magnetic type
WGaTcCr	0.080	-0.0115	6.129	1.86	FI
IrCrGeLi ⊡	0.089	-0.2385	5.961	2.86	FM
IrCrGeMn ⊡	0.010	-0.1929	5.988	1.94	FI
LiGePtCr ⊡	0.098	-0.3432	6.039	2.96	FM
OsCrGeMn ⊡	0.054	-0.0397	5.997	1.02	FI
MnGeRuCr	0.032	-0.1637	5.960	1.05	FI
GeVCrMn	0.054	-0.1852	5.828	1.94	FI
OsCrGeV	0.075	-0.1206	5.965	0.90	FI
VGeRuCr	0.043	-0.2320	5.947	0.93	FI
TcCrGeTi ⊡	0.052	-0.3254	6.121	2.72	FM
VGeTcCr	0.071	-0.1784	6.049	1.82	FI
IrCrZnHf ⊡	0.079	-0.3781	6.296	2.85	FM
HfSnTcCr ⊡	0.046	-0.2108	6.500	2.82	FM
MnSiIrCr	0.028	-0.3919	5.866	1.96	FI
TiSiIrCr	0.055	-0.6015	5.973	0.91	FM
TiZnIrCr ⊡	0.049	-0.3962	6.109	2.78	FM
OsCrSiMn	0.047	-0.2546	5.858	1.04	FI
MnSiRhCr	0.063	-0.4070	5.862	1.97	FI
MnSiRuCr	0.075	-0.3314	5.861	1.05	FI
CrSiTcMn	0.098	-0.2574	5.779	0.02	FI
SiVCrMn	0.067	-0.3903	5.723	1.92	FI
OsCrZnNb ⊡	0.090	-0.0233	6.205	2.77	FM

Continued on next page

Table A.3 – continued from previous page

Compounds	ΔE_{Hull}	ΔE_f	a	Spin moment	Magnetic type
RuCrZnNb ⊡	0.074	-0.0934	6.185	2.79	FM
RhNiZnCr △	0.088	-0.1107	5.909	2.91	FM
OsCrZnTa ⊡	0.083	-0.0719	6.198	2.76	FM
RhCrZnTi ⊡	0.100	-0.3649	6.100	2.84	FM
ScSnRuCr ⊡	0.089	-0.3351	6.464	2.78	FM
RuCrSiV	0.047	-0.4347	5.855	0.89	FI
RuCrZnTa ⊡	0.095	-0.1281	6.174	2.78	FM
TiSiTcCr ⊡	0.066	-0.4702	6.034	2.71	FM
VSiTcCr	0.086	-0.3729	5.900	0.00	AFM
TiSnTcCr ⊡	0.057	-0.2166	6.349	2.75	FM
TcCrSnZr ⊡	0.083	-0.2065	6.534	2.82	FM
FeGaIrCu ⊡	0.063	-0.1413	5.979	2.98	FM
GaTiCuFe	0.087	-0.2348	5.907	0.00	AFM
HfSnFeCu	0.096	-0.1619	6.343	0.00	AFM
IrCuZnFe	0.073	-0.0306	5.948	3.24	FM
SnTiCuFe □	0.095	-0.1721	6.180	0.00	AFM
MnGaIrCu	0.039	-0.1934	6.031	0.00	AFM
LiMnGaCu	0.086	-0.0996	5.922	3.14	FM
GaCuMgMn	0.089	-0.0380	6.183	3.40	FM
CuNiGaMn	0.066	-0.1393	5.748	3.54	FM
MnGaPdCu	0.089	-0.2406	6.088	3.72	FM
PtCuGaMn ⊡	0.031	-0.3128	6.109	3.65	FM

Continued on next page

Table A.3 – continued from previous page

Compounds	ΔE_{Hull}	ΔE_f	a	Spin moment	Magnetic type
MnGaRhCu	0.089	-0.2562	6.018	0.00	AFM
GaZnCuMn	0.070	-0.0280	6.007	3.16	FM
ScTiGaCu	0.079	-0.3399	6.423	0.00	NM
PtCuGeMn	0.091	-0.1613	6.140	3.83	FM
CuNiInMn	0.089	-0.0134	6.088	3.75	FM
PdCuInMn	0.097	-0.1576	6.316	3.82	FM
PtCuInMn	0.070	-0.2022	6.324	3.79	FM
MnInRhCu	0.099	-0.1170	6.255	0.00	AFM
MnSnIrCu ⊡	0.099	-0.0862	6.269	3.50	FM
MnZnIrCu	0.062	-0.0840	5.992	0.00	AFM
RhCuMnLi	0.035	-0.0692	5.898	0.00	AFM
YZnLiCu	0.084	-0.1610	6.510	0.00	NM
SnMnNiCu	0.066	-0.0837	6.096	3.73	FM
NiCuZnMn	0.070	-0.0613	5.814	3.77	FM
PdCuSnMn	0.096	-0.1931	6.326	3.78	FM
MnSnPtCu ⊡	0.097	-0.2169	6.336	3.75	FM
MnZnPtCu	0.033	-0.2517	6.069	0.00	AFM
RhCuSnMn	0.082	-0.1903	6.250	3.69	FM
RhCuZnMn	0.063	-0.1516	5.998	0.00	AFM
TiScZnCu	0.092	-0.1794	6.395	1.06	FM
NiFeGaHf	0.095	-0.3899	6.055	0.00	AFM
HfGaRuFe	0.090	-0.4216	6.164	0.89	FM

Continued on next page

Table A.3 – continued from previous page

Compounds	ΔE_{Hull}	ΔE_f	a	Spin moment	Magnetic type
MnGaIrFe	0.053	-0.1885	5.903	0.00	AFM
IrFeGaNb △	0.049	-0.3378	6.150	0.00	AFM
TaGaIrFe	0.040	-0.4009	6.137	0.00	AFM
VGaIrFe	0.056	-0.3364	5.936	0.00	AFM
NbGaLiFe ⊡	0.080	-0.1856	5.972	0.94	FM
MnFeGaNb	0.043	-0.1768	5.958	0.00	AFM
FeNiGaMn	0.049	-0.1662	5.783	4.03	FM
MnGaOsFe	0.070	-0.0413	5.877	0.00	AFM
MnGaPtFe ⊡	0.078	-0.2656	5.973	4.07	FM
MnGaRuFe	0.045	-0.1446	5.866	0.00	AFM
TaGaMnFe	0.047	-0.2221	5.947	0.98	FM
TcFeGaMn	0.029	-0.0650	5.900	3.22	FM
GaTiFeMn	0.022	-0.3187	5.868	1.98	FM
GaVFeMn	0.026	-0.2354	5.730	0.99	FI
ZnGaFeMn △	0.094	-0.0076	5.853	3.60	FM
RuFeGaMo	0.099	-0.0590	6.020	0.00	AFM
NiFeGaNb	0.067	-0.2408	5.975	0.00	AFM
RhFeGaNb △	0.049	-0.3599	6.110	0.00	AFM
NbGaTcFe	0.071	-0.1918	6.121	0.95	FM
FeGaPtNi	0.060	-0.2825	5.989	3.23	FM
FeGaRhNi	0.083	-0.2966	5.912	3.57	FM
FeGaRuNi	0.035	-0.1807	5.902	4.07	FM

Continued on next page

Table A.3 – continued from previous page

Compounds	ΔE_{Hull}	ΔE_f	a	Spin moment	Magnetic type
NiFeGaTa	0.074	-0.2683	5.976	0.00	AFM
GaTiFeNi	0.025	-0.4486	5.845	0.00	AFM
GaVFeNi	0.069	-0.2378	5.754	0.00	AFM
OsFeGaTi	0.091	-0.3709	6.007	0.91	FM
TiGaPdFe △	0.085	-0.4702	6.062	0.00	AFM
PtFeGaTi △	0.033	-0.5950	6.078	0.00	AFM
RhFeGaTa △	0.037	-0.4139	6.109	0.00	AFM
RhFeGaV	0.077	-0.3499	5.910	0.00	AFM
RuFeGaTi	0.018	-0.4902	5.975	0.90	FM
RuFeGaW	0.092	-0.0667	6.032	0.00	AFM
RuFeGaZr	0.087	-0.3614	6.202	0.92	FM
TcFeGaTa	0.097	-0.2472	6.115	0.92	FM
TcFeGaTi	0.055	-0.3047	6.038	1.76	FM
TcFeGaV	0.052	-0.2247	5.931	0.95	FI
MnGeIrFe	0.026	-0.1684	5.918	3.99	FM
IrFeGeTi	0.055	-0.5111	6.023	0.00	AFM
GeMnFeLi ⊡	0.084	-0.1211	5.716	1.97	FI
GeMnNiFe □	0.042	-0.1565	5.701	4.84	FM
OsFeGeMn	0.081	-0.0213	5.889	2.95	FM
MnGePtFe	0.083	-0.1876	6.009	4.92	FM
RhFeGeMn	0.046	-0.2436	5.898	4.01	FM
RuFeGeMn	0.042	-0.1545	5.864	2.94	FM

Continued on next page

Table A.3 – continued from previous page

Compounds	ΔE_{Hull}	ΔE_f	a	Spin moment	Magnetic type
MnGeTcFe	0.021	-0.1233	5.879	0.00	AFM
GeTiFeMn	0.037	-0.4038	5.817	0.97	FM
NbGeRuFe	0.088	-0.2174	6.097	0.00	AFM
RuNiGeFe □	0.098	-0.1047	5.898	3.43	FM
TaGeOsFe	0.081	-0.1179	6.124	0.00	AFM
RhFeGeTi	0.037	-0.5733	5.992	0.00	AFM
TaGeRuFe	0.066	-0.2569	6.093	0.00	AFM
RuFeGeV	0.055	-0.2557	5.884	0.00	AFM
TcFeGeTi	0.048	-0.4031	5.994	0.89	FM
IrFeSnHf	0.091	-0.4658	6.403	0.00	AFM
HfSnRhFe	0.043	-0.5304	6.381	0.00	AFM
TcFeSnHf	0.041	-0.2364	6.383	0.94	FM
LiSiIrFe	0.090	-0.4274	5.688	1.32	FM
IrZnMgFe	0.098	-0.1187	6.111	3.05	FM
IrFeSiMn	0.016	-0.3873	5.812	3.96	FM
IrMnZnFe △	0.089	-0.0543	5.998	6.62	FM
IrFeSiTi	0.042	-0.7042	5.926	0.00	AFM
IrFeSnTi	0.044	-0.4367	6.244	0.00	AFM
TiZnIrFe	0.056	-0.4176	6.001	0.98	FM
NiLiZnFe	0.090	-0.0580	5.726	0.00	AFM
RuFeSiLi	0.069	-0.2744	5.703	2.04	FM
LiFeSnZr ⊡	0.082	-0.3355	6.347	1.03	FM

Continued on next page

Table A.3 – continued from previous page

Compounds	ΔE_{Hull}	ΔE_f	a	Spin moment	Magnetic type
SiMnNiFe □	0.056	-0.3367	5.633	4.82	FM
SnMnFeNi	0.085	-0.0646	5.988	4.95	FM
OsFeSiMn	0.036	-0.2729	5.778	2.95	FM
ReFeSiMn	0.076	-0.2325	5.784	0.00	AFM
RhFeSiMn	0.045	-0.4225	5.789	4.00	FM
MnSiRuFe	0.040	-0.3643	5.758	2.95	FM
MnSiTcFe	0.014	-0.3392	5.767	0.00	AFM
TiSiFeMn	0.028	-0.6005	5.716	0.98	FM
SnTiFeMn	0.056	-0.2168	6.059	1.00	FM
NiFeZnNb	0.095	-0.0988	5.949	0.00	AFM
OsFeZnNb	0.096	-0.0185	6.114	0.95	FM
NbSnRuFe	0.079	-0.1644	6.297	0.00	AFM
NbZnRuFe	0.067	-0.1191	6.076	0.89	FM
FeZnRhNi	0.063	-0.1719	5.818	4.04	FM
SnTiFeNi □	0.093	-0.3426	6.073	0.00	AFM
NiFeZnTa	0.088	-0.1432	5.939	0.00	AFM
TaSiOsFe	0.090	-0.3127	6.042	0.00	AFM
VSiOsFe	0.026	-0.3897	5.813	0.00	AFM
OsFeSnTa	0.094	-0.0653	6.315	0.00	AFM
TaZnOsFe	0.054	-0.0983	6.103	0.91	FM
OsFeZnV	0.091	-0.0391	5.901	0.97	FI
TiSiRhFe	0.066	-0.7317	5.900	0.00	AFM

Continued on next page

Table A.3 – continued from previous page

Compounds	ΔE_{Hull}	ΔE_f	a	Spin moment	Magnetic type
RhFeSnTi	0.039	-0.5018	6.220	0.00	AFM
ScSnRuFe	0.094	-0.3311	6.330	0.92	FM
RuFeSiTa	0.072	-0.4242	6.008	0.00	AFM
VSiRuFe	0.045	-0.4817	5.786	0.00	AFM
RuFeSnTa	0.083	-0.2017	6.297	0.00	AFM
RuFeZnTa	0.069	-0.1874	6.067	0.85	FM
VZnRuFe	0.064	-0.1196	5.876	0.98	FI
TcFeSiTi	0.054	-0.5892	5.899	0.87	FM
TcFeSnTi	0.039	-0.2617	6.230	0.95	FM
ZrSnTcFe	0.088	-0.2020	6.422	0.99	FM
IrMnGaHf	0.074	-0.4761	6.221	0.93	FM
RuMnGaHf	0.100	-0.3750	6.214	1.97	FM
IrMnGaLi △	0.084	-0.2730	5.957	3.27	FM
IrLiTiGa ⊡	0.000	-0.6590	6.093	0.00	NM
IrMnGaMg	0.072	-0.2605	6.177	3.33	FM
MnIrGaTi	0.030	-0.5587	6.034	0.94	FM
IrMnGaZn	0.029	-0.2385	6.071	3.30	FM
MnLiGaMg	0.095	-0.0808	6.276	3.31	FM
LiNiGaMn ⊡	0.035	-0.2305	5.790	3.15	FM
PdMnGaLi ⊡	0.097	-0.3506	6.047	3.36	FM
PtMnGaLi	0.069	-0.4424	6.034	3.38	FM
RhMnGaLi	0.081	-0.3379	5.961	3.30	FM

Continued on next page

Table A.3 – continued from previous page

Compounds	ΔE_{Hull}	ΔE_f	a	Spin moment	Magnetic type
GaZnLiMn	0.070	-0.1165	5.897	2.96	FM
RhLiZrGa ⊡	0.012	-0.6144	6.302	0.00	NM
RhMnGaMg	0.083	-0.3280	6.169	3.30	FM
RuMnGaMg	0.070	-0.1178	6.147	3.28	FM
OsMnGaNb	0.027	-0.1710	6.140	0.99	FM
RuMnGaNb	0.061	-0.2746	6.112	0.99	FM
TcMnGaNb	0.028	-0.1898	6.167	1.97	FM
PdNiGaMn	0.053	-0.3384	6.029	4.06	FM
PtNiGaMn	0.025	-0.3995	6.027	4.07	FM
RhNiGaMn	0.025	-0.3942	5.946	4.38	FM
RuNiGaMn	0.059	-0.2195	5.837	0.00	AFM
TcNiGaMn	0.063	-0.1446	5.918	0.00	AFM
GaZnMnNi	0.081	-0.1585	5.924	3.29	FM
OsMnGaTa	0.028	-0.2392	6.138	0.95	FM
OsMnGaTi	0.073	-0.3427	6.063	1.91	FM
OsMnGaV	0.016	-0.2181	5.942	0.97	FI
PdMnGaZn	0.078	-0.2752	6.123	3.38	FM
PtMnGaZn	0.078	-0.3129	6.157	0.00	AFM
RhMnGaTi	0.043	-0.5528	6.017	0.98	FM
RhMnGaZn	0.046	-0.3256	6.056	3.29	FM
RuMnGaSc ⊡	0.079	-0.3422	6.233	2.94	FM
RuMnGaTa	0.068	-0.3297	6.106	0.95	FM

Continued on next page

Table A.3 – continued from previous page

Compounds	ΔE_{Hull}	ΔE_f	a	Spin moment	Magnetic type
RuMnGaTi	0.016	-0.4486	6.037	1.93	FM
RuMnGaV	0.038	-0.3070	5.923	0.98	FI
RuMnGaZn	0.042	-0.1572	6.031	3.19	FM
RuMnGaZr	0.098	-0.3318	6.263	2.03	FM
MnScGaZn	0.096	-0.2481	6.212	2.80	FM
TcMnGaTa	0.072	-0.2266	6.150	1.92	FM
TcMnGaTi	0.000	-0.3213	6.107	2.82	FM
TcMnGaV	0.013	-0.2201	5.994	1.90	FI
TcMnGaW	0.031	-0.0687	6.072	0.95	FI
TcMnGaZn △	0.074	-0.0010	6.091	3.45	FM
RhNiGaV △	0.088	-0.3674	5.944	1.21	FM
RuNiGaV	0.092	-0.3034	5.927	1.70	FM
IrMnGeLi	0.062	-0.2626	5.960	3.19	FM
GeMnNiLi ⊡	0.063	-0.2273	5.688	3.88	FM
PdMnGeLi	0.099	-0.3321	6.091	3.77	FM
PtMnGeLi	0.090	-0.3649	6.085	0.00	AFM
RhMnGeLi	0.075	-0.3579	5.957	3.18	FM
RuMnGeLi	0.091	-0.1759	5.921	3.12	FM
TcMnGeNb	0.083	-0.1892	6.129	0.98	FM
PtNiGeMn	0.094	-0.2488	6.056	3.86	FM
RhNiGeMn	0.052	-0.2978	5.964	4.12	FM
RuNiGeMn □	0.067	-0.1902	5.937	0.00	AFM

Continued on next page

Table A.3 – continued from previous page

Compounds	ΔE_{Hull}	ΔE_f	a	Spin moment	Magnetic type
TcNiGeMn □	0.096	-0.1159	5.940	0.00	AFM
OsMnGeTi	0.059	-0.3571	6.014	0.93	FM
RuMnGeTi	0.056	-0.4920	5.985	0.93	FM
TcMnGeTa	0.065	-0.2252	6.134	0.93	FM
TcMnGeTi	0.029	-0.3652	6.051	1.89	FM
TcMnGeV	0.035	-0.2532	5.928	0.95	FI
HfZnIrMn △	0.090	-0.3762	6.302	3.17	FM
ScYHgIn	0.066	-0.3955	7.578	0.00	NM
InMnNiLi ⊡	0.083	-0.1064	6.088	3.56	FM
PdNiInMn	0.073	-0.2188	6.243	4.18	FM
PtNiInMn	0.055	-0.2544	6.260	4.21	FM
RhNiInMn □	0.045	-0.2082	6.174	4.51	FM
LiSiIrMn	0.075	-0.4418	5.777	2.63	FM
MgMnZnIr	0.084	-0.1603	6.179	0.00	AFM
IrMnZnNb	0.091	-0.2013	6.133	0.00	AFM
IrMnZnTa	0.082	-0.2696	6.123	0.96	FM
IrMnZnTi ⊡	0.083	-0.4033	6.058	2.01	FM
VZnIrMn	0.072	-0.2295	5.936	1.00	FI
SnMnNiLi ⊡	0.025	-0.2504	6.081	3.88	FM
LiNiZnMn	0.094	-0.0542	5.818	0.00	AFM
LiSiOsMn ⊡	0.074	-0.1953	5.790	2.95	FM
LiSiRhMn	0.095	-0.4812	5.786	2.88	FM

Continued on next page

Table A.3 – continued from previous page

Compounds	ΔE_{Hull}	ΔE_f	a	Spin moment	Magnetic type
LiSiRuMn ⊡	0.047	-0.3278	5.787	3.02	FM
SnZnLiMn	0.092	-0.1064	6.331	0.00	AFM
LiSiTcNi	0.097	-0.3016	5.712	0.00	NM
MgMnZnPt	0.095	-0.3614	6.254	3.65	FM
RuMnSnMg ⊡	0.092	-0.0631	6.388	3.24	FM
RuMnZnNb	0.085	-0.1090	6.129	2.05	FM
NbSnTcMn	0.092	-0.0961	6.330	1.03	FM
PdNiSbMn	0.086	-0.1858	6.286	4.13	FM
MnSnPdNi	0.044	-0.2827	6.250	3.96	FM
MnZnPdNi	0.081	-0.2415	5.994	4.32	FM
MnSnPtNi	0.060	-0.2929	6.268	3.95	FM
MnZnPtNi	0.001	-0.3203	6.002	4.31	FM
RhNiSbMn	0.081	-0.2099	6.187	3.90	FM
MnSiRhNi	0.078	-0.4344	5.860	4.06	FM
MnSnRhNi	0.043	-0.2977	6.180	4.24	FM
RhNiZnMn	0.014	-0.2326	5.844	4.04	FM
RuNiSiMn	0.095	-0.3551	5.828	0.00	AFM
RuNiSnMn □	0.050	-0.1253	6.150	0.00	AFM
MnZnRuNi	0.092	-0.0398	5.870	3.02	FM
TiSiOsMn	0.032	-0.5742	5.916	0.91	FM
OsMnZnTa	0.071	-0.0833	6.143	1.96	FM
TiZnPtMn	0.087	-0.4304	6.138	0.00	AFM

Continued on next page

Table A.3 – continued from previous page

Compounds	ΔE_{Hull}	ΔE_f	a	Spin moment	Magnetic type
TiSiRuMn	0.049	-0.6742	5.891	0.93	FM
RuMnSnTi	0.066	-0.3568	6.215	0.98	FM
VZnRuMn	0.083	-0.1250	5.942	1.95	FI
TiSbTcMn	0.048	-0.2687	6.221	0.96	FM
TcMnSiTa	0.084	-0.3989	6.039	0.91	FM
TiSiTcMn	0.029	-0.5356	5.952	1.86	FM
VSiTcMn	0.040	-0.4740	5.831	0.89	FI
TcMnSnTi	0.048	-0.2348	6.276	1.95	FM
RhNiZnV $^{\triangle}$	0.081	-0.2586	5.916	1.67	FM
VZnRuNi	0.076	-0.1737	5.896	0.68	FM

Appendix B

Code Availability

Necessary codes or scripts for this thesis can be found on Github:
https://github.com/b00249667/HT-Heusler.

Bibliography

[1] B. Dieny and M. Chshiev, *Perpendicular Magnetic Anisotropy at Transition Metal/Oxide Interfaces and Applications*, Rev. Mod. Phys. **89**, 025008 (2017).

[2] F. Hellman, A. Hoffmann, Y. Tserkovnyak, G. S. Beach, E. E. Fullerton, C. Leighton, A. H. MacDonald, D. C. Ralph, D. A. Arena, H. A. Dürr, P. Fischer, J. Grollier, J. P. Heremans, T. Jungwirth, A. V. Kimel, B. Koopmans, I. N. Krivorotov, S. J. May, A. K. Petford-Long, J. M. Rondinelli, N. Samarth, I. K. Schuller, A. N. Slavin, M. D. Stiles, O. Tchernyshyov, A. Thiaville, and B. L. Zink, *Interface-Induced Phenomena in Magnetism*, Rev. Modern Phys. **89**, 025006 (2017).

[3] A. Brataas, A. D. Kent, and H. Ohno, *Current-Induced Torques in Magnetic Materials*, Nat. Mater. **11**, 372–381 (2012).

[4] A. D. Kent and D. C. Worledge, *A New Spin on Magnetic Memories*, Nat. Nanotechnol. **10**, 187–191 (2015).

[5] M. Wang, W. Cai, D. Zhu, Z. Wang, J. Kan, Z. Zhao, K. Cao, Z. Wang, Y. Zhang, T. Zhang, C. Park, J.-P. Wang, A. Fert, and W. Zhao, *Field-Free Switching of a Perpendicular Magnetic Tunnel Junction Through the Interplay of Spin-Orbit and Spin-Transfer Torques*, Nat. Electron. **1**, 582–588 (2018).

[6] D. Apalkov, B. Dieny, and J. Slaughter, *Magnetoresistive Random Access Memory*, Proc. IEEE **104**, 1796–1830 (2016).

[7] D. Worledge, G. Hu, D. W. Abraham, J. Sun, P. Trouilloud, J. Nowak, S. Brown, M. Gaidis, E. O'sullivan, and R. Robertazzi, *Spin Torque Switching of Perpendicular Ta | CoFeB | MgO-Based Magnetic Tunnel Junctions*, Appl. Phys. Lett. **98**, 022501 (2011).

[8] S. Peng, W. Kang, M. Wang, K. Cao, X. Zhao, L. Wang, Y. Zhang, Y. Zhang, Y. Zhou, K. L. Wang, and W. Zhao, *Interfacial Perpendicular Magnetic Anisotropy in Sub-20 Nm Tunnel Junctions for Large-Capacity Spin-Transfer Torque Magnetic Random-Access Memory*, IEEE Magn. Lett. **8**, 1–5 (2017).

[9] S. Ikeda, K. Miura, H. Yamamoto, K. Mizunuma, H. D. Gan, M. Endo, S. Kanai, J. Hayakawa, F. Matsukura, and H. Ohno, *A Perpendicular-Anisotropy CoFeB-MgO Magnetic Tunnel Junction*, Nat. Mater. **9**, 721–724 (2010).

[10] K. Nakamura, T. Akiyama, T. Ito, M. Weinert, and A. J. Freeman, *Role of an Interfacial FeO Layer in the Electric-Field-Driven Switching of Magnetocrystalline Anisotropy at the Fe/MgO Interface*, Phys. Rev. B **81**, 220409 (2010).

[11] J. W. Koo, S. Mitani, T. T. Sasaki, H. Sukegawa, Z. C. Wen, T. Ohkubo, T. Niizeki, K. Inomata, and K. Hono, *Large Perpendicular Magnetic Anisotropy at Fe/MgO Interface*, Appl. Phys. Lett. **103**, 192401 (2013).

[12] T. Nozaki, A. Kozioł-Rachwał, W. Skowroński, V. Zayets, Y. Shiota, S. Tamaru, H. Kubota, A. Fukushima, S. Yuasa, and Y. Suzuki, *Large Voltage-Induced Changes in the Perpendicular Magnetic Anisotropy of an MgO-based Tunnel Junction with an Ultrathin Fe Layer*, Phys. Rev. A **5**, 044006 (2016).

[13] S. Nazir, S. Jiang, J. Cheng, and K. Yang, *Enhanced Interfacial Perpendicular Magnetic Anisotropy in Fe/MgO Heterostructure via Interfacial Engineering*, Appl. Phys. Lett. **114**, 072407 (2019).

[14] A. Conca, A. Niesen, G. Reiss, and B. Hillebrands, *Evolution of the Interfacial Perpendicular Magnetic Anisotropy Constant of the Co_2FeAl/MgO Interface Upon Annealing*, J. Phys. D: Appl. Phys. **51**, 165303 (2018).

[15] M. Belmeguenai, M. Gabor, T. Petrisor Jr, F. Zighem, S. Chérif, and C. Tiusan, *Capping Layer-Tailored Interface Magnetic Anisotropy in Ultrathin Co_2FeAl Films*, J. Appl. Phys. **117**, 023906 (2015).

[16] R. Vadapoo, A. Hallal, H. Yang, and M. Chshiev, *First-Principles Investigation of Magnetocrystalline Anisotropy at the $L2_1$ Full Heusler | MgO Interfaces and Tunnel Junctions*, Phys. Rev. B **94**, 104418 (2016).

[17] K. Elphick, W. Frost, M. Samiepour, T. Kubota, K. Takanashi, S. Hiroaki, S. Mitani, and A. Hirohata, *Heusler Alloys for Spintronic Devices: Review on Recent Development and Future Perspectives*, Sci. Technol. Adv. Mater. **22**, 235–271 (2020).

[18] A. Hirohata, W. Frost, M. Samiepour, and J. young Kim, *Perpendicular Magnetic Anisotropy in Heusler Alloy Films and Their Magnetoresistive Junctions*, Materials **11**, 105 (2018).

[19] A. Kumar, F. Pan, S. Husain, S. Akansel, R. Brucas, L. Bergqvist, S. Chaudhary, and P. Svedlindh, *Temperature-Dependent Gilbert Damping of Co_2FeAl Thin Films with Different Degree of Atomic Order*, Phys. Rev. B **96**, 224425 (2017).

[20] S. Mizukami, D. Watanabe, M. Oogane, Y. Ando, Y. Miura, M. Shirai, and T. Miyazaki, *Low Damping Constant for Co_2FeAl Heusler Alloy Films and Its Correlation with Density of States*, J. Appl. Phys. **105**, 07D306 (2009).

[21] Y. Miura, H. Uchida, Y. Oba, K. Abe, and M. Shirai, *Half-Metallic Interface and Coherent Tunneling in $Co_2YZ/MgO/Co_2YZ$(YZ=MnSi,CrAl) Magnetic Tunnel Junctions: A First-Principles Study*, Phys. Rev. B **78**, 064416 (2008).

[22] T. Ishikawa, S. Hakamata, K. ichi Matsuda, T. Uemura, and M. Yamamoto, *Fabrication of Fully Epitaxial $Co_2MnSi/MgO/Co_2MnSi$ Magnetic Tunnel Junctions*, J. Appl. Phys. **103**, 07A919 (2008).

[23] N. Tezuka, N. Ikeda, S. Sugimoto, and K. Inomata, *175% Tunnel Magnetoresistance at Room Temperature and High Thermal Stability Using $Co_2FeAl_{0.5}Si_{0.5}$ Full-Heusler Alloy Electrodes*, Appl. Phys. Lett. **89**, 252508 (2006).

[24] R. A. de Groot, F. M. Mueller, P. G. van Engen, and K. H. J. Buschow, *New Class of Materials: Half-Metallic Ferromagnets*, Phys. Rev. Lett. **50**, 2024–2027 (1983).

[25] F. Heusler, W. Starck, and E. Haupt, *Magnetisch-Chemische Studien*, Verh. Dtsch. Phys. Ges. **5**, 219–232 (1903).

[26] F. Heusler, *Über Magnetische Manganlegierungen*, Verh. Dtsch. Phys. Ges. **5**, 219 (1903).

[27] H. C. Kandpal, G. H. Fecher, and C. Felser, *Calculated Electronic and Magnetic Properties of the Half-Metallic, Transition Metal Based Heusler Compounds*, J. Phys. D: Appl. Phys. **40**, 1507–1523 (2007).

[28] I. Galanakis, P. Mavropoulos, and P. H. Dederichs, *Electronic Structure and Slater–Pauling Behaviour in Half-Metallic Heusler Alloys Calculated from First Principles*, J. Phys. D: Appl. Phys. **39**, 765–775 (2006).

[29] M. Ram, A. Saxena, A. E. Aly, and A. Shankar, *Half-Metallicity in New Heusler Alloys Mn_2ScZ (Z = Si, Ge, Sn)*, RSC Advances **10**, 7661–7670 (2020).

[30] J. Kübler, A. William, and C. Sommers, *Formation and Coupling of Magnetic Moments in Heusler Alloys*, Phys. Rev. B **28**, 1745 (1983).

[31] K. Endo, H. Matsuda, K. Ooiwa, and K. Itoh, *Antiferromagnetism in a Heusler Alloy Fe_2VSi*, J. Phys. Soc. Jpn. **64**, 2329–2332 (1995).

[32] S. Wurmehl, H. C. Kandpal, G. H. Fecher, and C. Felser, *Valence Electron Rules for Prediction of Half-Metallic Compensated-Ferrimagnetic Behaviour of Heusler Compounds with Complete Spin Polarization*, J. Phys.: Condens. Matter **18**, 6171–6181 (2006).

[33] J. Noky, Y. Zhang, J. Gooth, C. Felser, and Y. Sun, *Giant Anomalous Hall and Nernst Effect in Magnetic Cubic Heusler Compounds*, npj Comput. Mater. **6**, 1–8 (2020).

[34] J. Wernick, G. Hull, T. Geballe, J. Bernardini, and J. Waszczak, *Superconductivity in Ternary Heusler Intermetallic Compounds*, Mater. Lett. **2**, 90–92 (1983).

[35] T. Klimczuk, C. H. Wang, K. Gofryk, F. Ronning, J. Winterlik, G. H. Fecher, J.-C. Griveau, E. Colineau, C. Felser, J. D. Thompson, D. J. Safarik, and R. J. Cava, *Superconductivity in the Heusler Family of Intermetallics*, Phys. Rev. B **85**, 174505 (2012).

[36] T. Graf, C. Felser, and S. S. Parkin, *Simple Rules for the Understanding of Heusler Compounds*, Prog. Solid State Chem. **39**, 1–50 (2011).

[37] X.-Z. Li, W.-Y. Zhang, S. Valloppilly, and D. J. Sellmyer, *New Heusler Compounds in Ni-Mn-In and Ni-Mn-Sn Alloys*, Sci. Rep. **9**, 7762 (2019).

[38] C. Fu, S. Bai, Y. Liu, Y. Tang, L. Chen, X. Zhao, and T. Zhu, *Realizing High Figure of Merit in Heavy-Band P-Type Half-Heusler Thermoelectric Materials*, Nat. Commun. **6**, 1–7 (2015).

[39] S. Chen and Z. Ren, *Recent Progress of Half-Heusler for Moderate Temperature Thermoelectric Applications*, Mater. Today **16**, 387–395 (2013).

[40] T. Zhu, C. Fu, H. Xie, Y. Liu, and X. Zhao, *High Efficiency Half-Heusler Thermoelectric Materials for Energy Harvesting*, Adv. Electron. Mater. **5**, 1500588 (2015).

[41] W. G. Zeier, J. Schmitt, G. Hautier, U. Aydemir, Z. M. Gibbs, C. Felser, and G. J. Snyder, *Engineering Half-Heusler Thermoelectric Materials Using Zintl Chemistry*, Nat. Rev. Mater. **1**, 1–10 (2016).

[42] J. Carrete, W. Li, N. Mingo, S. Wang, and S. Curtarolo, *Finding Unprecedentedly Low-Thermal-Conductivity Half-Heusler Semiconductors Via High-Throughput Materials Modeling*, Phys. Rev. X **4**, 011019 (2014).

[43] S. Chadov, X. Qi, J. Kübler, G. H. Fecher, C. Felser, and S. C. Zhang, *Tunable Multifunctional Topological Insulators in Ternary Heusler Compounds*, Nat. Mater. **9**, 541–545 (2010).

[44] H. Lin, L. A. Wray, Y. Xia, S. Xu, S. Jia, R. J. Cava, A. Bansil, and M. Z. Hasan, *Half-Heusler Ternary Compounds as New Multifunctional Experimental Platforms for Topological Quantum Phenomena*, Nat. Mater. **9**, 546–549 (2010).

[45] L. Wollmann, A. K. Nayak, S. S. Parkin, and C. Felser, *Heusler 4.0: Tunable Materials*, Annu. Rev. Mater. Res. **47**, 247–270 (2017).

[46] S. Chadov, S. W. D'Souza, L. Wollmann, J. Kiss, G. H. Fecher, and C. Felser, *Chemical Disorder as an Engineering Tool for Spin Polarization in Mn_3Ga-based Heusler Systems*, Phys. Rev. B **91**, 094203 (2015).

[47] L. Wollmann, G. H. Fecher, S. Chadov, and C. Felser, *A Scheme for Spin-Selective Electron Localization in Mn_3Ga Heusler Material*, J. Phys. D: Appl. Phys. **48**, 164004 (2015).

[48] X. Zhao, J. Lu, S. Mao, Z. Yu, D. Wei, and J. Zhao, *Spin-Orbit Torque Induced Magnetization Switching in Ferrimagnetic Heusler Alloy $D0_{22}$-Mn_3Ga with Large Perpendicular Magnetic Anisotropy*, Appl. Phys. Lett. **115**, 142405 (2019).

[49] V. Alijani, J. Winterlik, G. H. Fecher, S. S. Naghavi, and C. Felser, *Quaternary Half-Metallic Heusler Ferromagnets for Spintronics Applications*, Phys. Rev. B **83**, 184428 (2011).

[50] R. Gautier, X. Zhang, L. Hu, L. Yu, Y. Lin, T. O. L. Sunde, D. Chon, K. R. Poeppelmeier, and A. Zunger, *Prediction and Accelerated Laboratory Discovery of Previously Unknown 18-Electron ABX Compounds*, Nat. Chem. **7**, 308–316 (2015).

[51] F. Yan, X. Zhang, Y. G. Yu, L. Yu, A. Nagaraja, T. O. Mason, and A. Zunger, *Design and Discovery of a Novel Half-Heusler Transparent Hole Conductor Made of All-Metallic Heavy Elements*, Nat. Commun. **6**, 1–8 (2015).

[52] L. Petti, N. Münzenrieder, C. Vogt, H. Faber, L. Büthe, G. Cantarella, F. Bottacchi, T. D. Anthopoulos, and G. Tröster, *Metal Oxide Semiconductor Thin-Film Transistors for Flexible Electronics*, Appl. Phys. Rev. **3**, 021303 (2016).

[53] Q. Gao, I. Opahle, and H. Zhang, *High-Throughput Screening for Spin-Gapless Semiconductors in Quaternary Heusler Compounds*, Phys. Rev. Mater. **3**, 024410 (2019).

[54] K. Kim, L. Ward, J. He, A. Krishna, A. Agrawal, and C. Wolverton, *Machine-Learning-Accelerated High-Throughput Materials Screening: Discovery of Novel Quaternary Heusler Compounds*, Phys. Rev. Mater. **2**, 123801 (2018).

[55] Y. Wang, X. Zhang, B. Ding, Z. Hou, E. Liu, Z. Liu, X. Xi, H. Zhang, G. Wu, and W. Wang, *Magnetic Semiconductors Based on Quaternary Heusler Compounds*, Comput. Mater. Sci. **150**, 321–324 (2018).

[56] S. V. Faleev, Y. Ferrante, J. Jeong, M. G. Samant, B. Jones, and S. S. Parkin, *Origin of the Tetragonal Ground State of Heusler Compounds*, Phys. Rev. Appl. **7**, 034022 (2017).

[57] A. Anelli, E. A. Engel, C. J. Pickard, and M. Ceriotti, *Generalized Convex Hull Construction for Materials Discovery*, Phys. Rev. Mater. **2**, 103804 (2018).

[58] C. Oses, E. Gossett, D. Hicks, F. Rose, M. J. Mehl, E. Perim, I. Takeuchi, S. Sanvito, M. Scheffler, Y. Lederer, C. Toher, and S. Curtarolo, *AFLOW-CHULL: Cloud-Oriented Platform for Autonomous Phase Stability Analysis*, J. Chem. Inf. Model. **58**, 2477–2490 (2018).

[59] J. Ma, V. I. Hegde, K. Munira, Y. Xie, S. Keshavarz, D. T. Mildebrath, C. Wolverton, A. W. Ghosh, and W. Butler, *Computational Investigation of Half-Heusler Compounds for Spintronics Applications*, Phys. Rev. B **95**, 024411 (2017).

[60] J. Balluff, K. Diekmann, G. Reiss, and M. Meinert, *High-Throughput Screening for Antiferromagnetic Heusler Compounds Using Density Functional Theory*, Phys. Rev. Mater. **1**, 034404 (2017).

[61] G. Hautier, A. Jain, S. P. Ong, B. Kang, C. Moore, R. Doe, and G. Ceder, *Phosphates as Lithium-Ion Battery Cathodes: An Evaluation Based on High-Throughput Ab Initio Calculations*, Chem. Mater. **23**, 3495–3508 (2011).

[62] S. Sanvito, C. Oses, J. Xue, A. Tiwari, M. Zic, T. Archer, P. Tozman, M. Venkatesan, M. Coey, and S. Curtarolo, *Accelerated Discovery of New Magnets in the Heusler Alloy Family*, Sci. Adv. **3**, e1602241 (2017).

[63] A. Togo and I. Tanaka, *First Principles Phonon Calculations in Materials Science*, Scr. Mater. **108**, 1–5 (2015).

[64] Vikram, B. Sahni, C. Barman, and A. Alam, *Accelerated Discovery of New 8-Electron Half-Heusler Compounds as Promising Energy and Topological Quantum Materials*, J. Phys. Chem. C **123**, 7074–7080 (2019).

[65] Vikram, B. Sahni, C. K. Barman, and A. Alam, *Reply to "Comment on 'Accelerated Discovery of New 8-Electron Half-Heusler Compounds as Promising Energy and Topological Quantum Materials'"*, J. Phys. Chem. C **124**, 2245–2246 (2020).

[66] S. A. Khandy, I. Islam, D. C. Gupta, R. Khenata, and A. Laref, *Lattice Dynamics, Mechanical Stability and Electronic Structure of Fe-Based Heusler Semiconductors*, Sci. Rep. **9**, 1475 (2019).

[67] I. Galanakis, P. Dederichs, and N. Papanikolaou, *Slater-Pauling Behavior and Origin of the Half-Metallicity of the full-Heusler Alloys*, Phys. Rev. B **66**, 174429 (2002).

[68] J. Kübler, *First Principle Theory of Metallic Magnetism*, Physica B+C **127**, 257–263 (1984).

[69] J. C. Slater, *The Ferromagnetism of Nickel. II. Temperature Effects*, Phys. Rev. **49**, 931 (1936).

[70] L. Pauling, *The Nature of the Interatomic Forces in Metals*, Phys. Rev. **54**, 899 (1938).

[71] G. Ceder, *Opportunities and Challenges for First-Principles Materials Design and Applications to Li Battery Materials*, MRS Bull. **35**, 693–701 (2010).

[72] K. Yang, W. Setyawan, S. Wang, M. B. Nardelli, and S. Curtarolo, *A Search Model for Topological Insulators with High-Throughput Robustness Descriptors*, Nat. Mater. **11**, 614–619 (2012).

[73] S. Curtarolo, G. L. W. Hart, M. B. Nardelli, N. Mingo, S. Sanvito, and O. Levy, *The High-Throughput Highway to Computational Materials Design*, Nat. Mater. **12**, 191–201 (2013).

[74] A. Jain, G. Hautier, C. J. Moore, S. P. Ong, C. C. Fischer, T. Mueller, K. A. Persson, and G. Ceder, *A High-Throughput Infrastructure for Density Functional Theory Calculations*, Comput. Mater. Sci. **50**, 2295–2310 (2011).

[75] J. Winterlik, S. Chadov, A. Gupta, V. Alijani, T. Gasi, K. Filsinger, B. Balke, G. H. Fecher, C. A. Jenkins, F. Casper, et al., *Design Scheme of New Tetragonal Heusler Compounds for Spin-Transfer Torque Applications and Its Experimental Realization*, Adv. Mater. **24**, 6283–6287 (2012).

[76] S. V. Faleev, Y. Ferrante, J. Jeong, M. G. Samant, B. Jones, and S. S. P. Parkin, *Heusler Compounds with Perpendicular Magnetic Anisotropy and Large Tunneling Magnetoresistance*, Phys. Rev. Mater. **1**, 024402 (2017).

[77] J. Ma, J. He, D. Mazumdar, K. Munira, S. Keshavarz, T. Lovorn, C. Wolverton, A. W. Ghosh, and W. H. Butler, *Computational Investigation of Inverse Heusler Compounds for Spintronics Applications*, Phys. Rev. B **98**, 094410 (2018).

[78] D. Do, M.-S. Lee, and S. D. Mahanti, *Effect of Onsite Coulomb Repulsion on Thermoelectric Properties of full-Heusler Compounds with Pseudogaps*, Phys. Rev. B **84**, 125104 (2011).

[79] S. Sharma and S. K. Pandey, *Investigation of the Electronic and Thermoelectric Properties of Fe_2ScX (X= P, As and Sb) Full Heusler Alloys by Using First Principles Calculations*, J. Phys. D: Appl. Phys. **47**, 445303 (2014).

[80] Y. Shimanuki, K. Kudo, T. Ishibe, A. Masago, S. Yamada, Y. Nakamura, and K. Hamaya, *Thermoelectric Properties of Single-Phase Full-Heusler Alloy Fe_2TiSi Films with $D0_3$-Type Disordering*, J. Appl. Phys. **127**, 055106 (2020).

[81] J. He, M. Amsler, Y. Xia, S. S. Naghavi, V. I. Hegde, S. Hao, S. Goedecker, V. Ozoliņš, and C. Wolverton, *Ultralow Thermal Conductivity in Full Heusler Semiconductors*, Phys. Rev. Lett. **117**, 046602 (2016).

[82] A. O. Oliynyk, E. Antono, T. D. Sparks, L. Ghadbeigi, M. W. Gaultois, B. Meredig, and A. Mar, *High-Throughput Machine-Learning-Driven Synthesis of full-Heusler Compounds*, Chem. Mater. **28**, 7324–7331 (2016).

[83] S. Guo, T. Jia, and Y. Zhang, *Electrical Property Dominated Promising Half-Heusler Thermoelectrics Through High-Throughput Material Computations*, J. Phys. Chem. C **123**, 18824–18833 (2019).

[84] J. He, S. S. Naghavi, V. I. Hegde, M. Amsler, and C. Wolverton, *Designing and Discovering a New Family of Semiconducting Quaternary Heusler Compounds Based on the 18-Electron Rule*, Chem. Mater. **30**, 4978–4985 (2018).

[85] W. A. Borders, A. Z. Pervaiz, S. Fukami, K. Y. Camsari, H. Ohno, and S. Datta, *Integer Factorization Using Stochastic Magnetic Tunnel Junctions*, Nature **573**, 390–393 (2019).

[86] K. Y. Camsari, S. Chowdhury, and S. Datta, *Scalable Emulation of Sign-Problem–Free Hamiltonians with Room-Temperature P -Bits*, Phys. Rev. Applied **12**, 034061 (2019).

[87] S. Mangin, D. Ravelosona, J. A. Katine, M. J. Carey, B. D. Terris, and E. E. Fullerton, *Current-Induced Magnetization Reversal in Nanopillars with Perpendicular Anisotropy*, Nat. Mater. **5**, 210–215 (2006).

[88] C. Chappert, A. Fert, and F. N. V. Dau, *The Emergence of Spin Electronics in Data Storage*, Nat. Mater. **6**, 813–823 (2007).

[89] S. Tsunegi, H. Kubota, S. Tamaru, K. Yakushiji, M. Konoto, A. Fukushima, T. Taniguchi, H. Arai, H. Imamura, and S. Yuasa, *Damping Parameter and Interfacial Perpendicular Magnetic Anisotropy of FeB Nanopillar Sandwiched Between MgO Barrier and Cap Layers in Magnetic Tunnel Junctions*, Appl. Phys. Express **7**, 033004 (2014).

[90] Q. Xiang, R. Mandal, H. Sukegawa, Y. K. Takahashi, and S. Mitani, *Large Perpendicular Magnetic Anisotropy in Epitaxial Fe/$MgAl_2O_4$(001) Heterostructures*, Appl. Phys. Express **11**, 063008 (2018).

[91] Q. Sun, S. Kwon, M. Stamenova, S. Sanvito, and N. Kioussis, *Electric Field Modulation of Magnetism in Ferrimagnetic Heusler Heterostructures*, Phys. Rev. B **101**, 134419 (2020).

[92] L. Néel, *Anisotropie magnétique Superficielle Et Surstructures d'orientation*, J. Phys. Radium **15**, 225–239 (1954).

[93] F. J. A. den Broeder, D. Kuiper, A. P. van de Mosselaer, and W. Hoving, *Perpendicular Magnetic Anisotropy of Co-Au Multilayers Induced by Interface Sharpening*, Phys. Rev. Lett. **60**, 2769–2772 (1988).

[94] V. W. Guo, B. Lu, X. Wu, G. Ju, B. Valcu, and D. Weller, *A Survey of Anisotropy Measurement Techniques and Study of Thickness Effect on Interfacial and Volume Anisotropies in Co/Pt Multilayer Media*, J. Appl. Phys. **99**, 08E918 (2006).

[95] T. Bertelli, T. Bueno, A. Krohling, B. Silva, R. Rodríguez-Suárez, V. Nascimento, R. Paniago, K. Krambrock, C. Larica, and E. Passamani, *Magnetic Anisotropy of Co Thin Films: Playing with the Shadowing Effect, Magnetic Field and Substrate Spinning*, J. Magn. Magn. Mater. **426**, 636–640 (2017).

[96] L. E. Nistor, B. Rodmacq, S. Auffret, and B. Dieny, *Pt/Co/Oxide and Oxide/Co/Pt Electrodes for Perpendicular Magnetic Tunnel Junctions*, Appl. Phys. Lett. **94**, 012512 (2009).

[97] S. Monso, B. Rodmacq, S. Auffret, G. Casali, F. Fettar, B. Gilles, B. Dieny, and P. Boyer, *Crossover from In-Plane to Perpendicular Anisotropy in Pt/CoFe/AlO_x Sandwiches as a Function of Al Oxidation: A Very Accurate Control of the Oxidation of Tunnel Barriers*, Appl. Phys. Lett. **80**, 4157–4159 (2002).

[98] A. Manchon, C. Ducruet, L. Lombard, S. Auffret, B. Rodmacq, B. Dieny, S. Pizzini, J. Vogel, V. Uhlíř, M. Hochstrasser, and G. Panaccione, *Analysis of Oxygen Induced Anisotropy Crossover in Pt/Co/MO_x Trilayers*, J. Appl. Phys. **104**, 043914 (2008).

[99] B. Rodmacq, S. Auffret, B. Dieny, S. Monso, and P. Boyer, *Crossovers from In-Plane to Perpendicular Anisotropy in Magnetic Tunnel Junctions as a Function of the Barrier Degree of Oxidation*, J. Appl. Phys. **93**, 7513–7515 (2003).

[100] L. Vojáček, F. Ibrahim, A. Hallal, B. Dieny, and M. Chshiev, *Giant Perpendicular Magnetic Anisotropy Enhancement in MgO-Based Magnetic Tunnel Junction by Using Co/Fe Composite Layer*, Phys. Rev. Applied **15**, 024017 (2021).

[101] S. Jiang, S. Nazir, and K. Yang, *Origin of the Large Interfacial Perpendicular Magnetic Anisotropy in MgO/Co_2FeAl*, Phys. Rev. B **101**, 134405 (2020).

[102] Z. Wen, H. Sukegawa, S. Mitani, and K. Inomata, *Perpendicular Magnetization of Co_2FeAl Full-Heusler Alloy Films Induced by MgO Interface*, Appl. Phys. Lett. **98**, 242507 (2011).

[103] K. Masuda, H. Itoh, Y. Sonobe, H. Sukegawa, S. Mitani, and Y. Miura, *Interfacial Giant Tunnel Magnetoresistance and Bulk-Induced Large Perpendicular Magnetic Anisotropy in (111)-Oriented Junctions with fcc Ferromagnetic Alloys: A First-Principles Study*, Phys. Rev. B **103**, 064427 (2021).

[104] K. Masuda, H. Itoh, and Y. Miura, *Interface-Driven Giant Tunnel Magnetoresistance in (111)-Oriented Junctions*, Phys. Rev. B **101**, 144404 (2020).

[105] R. Mandal, Q. Xiang, K. Masuda, Y. Miura, H. Sukegawa, S. Mitani, and Y. K. Takahashi, *Spin-Resolved Contribution to Perpendicular Magnetic Anisotropy and Gilbert Damping in Interface-Engineered Fe/$MgAl_2O_4$ Heterostructures*, Phys. Rev. Applied **14**, 064027 (2020).

[106] F. Li, B. Yang, J. Zhang, X. Han, and Y. Yan, *Interface-Induced Perpendicular Magnetic Anisotropy in Co_2FeAl/$NiFe_2O_4$ Superlattice: First-Principles Study*, Phys. Chem. Chem. Phys. **22**, 716–723 (2020).

[107] K. Masuda, S. Kasai, Y. Miura, and K. Hono, *Giant Interfacial Perpendicular Magnetic Anisotropy in Fe/$CuIn_{1-x}Ga_xSe_2$ Beyond Fe/MgO*, Phys. Rev. B **96**, 174401 (2017).

[108] Y. He, G. H. Fecher, C. Fu, Y. Pan, K. Manna, J. Kroder, A. Jha, X. Wang, Z. Hu, S. Agrestini, J. Herrero-Martín, M. Valvidares, Y. Skourski, W. Schnelle, P. Stamenov, H. Borrmann, L. H. Tjeng, R. Schaefer, S. S. P. Parkin, J. M. D. Coey, and C. Felser, *A New Highly Anisotropic Rh-Based Heusler Compound for Magnetic Recording*, Adv. Mater. **32**, 2004331 (2020).

[109] S. Jiang and K. Yang, *Review of High-Throughput Computational Design of Heusler Alloys*, J. Alloys Compound. **867**, 158854 (2021).

[110] X. Wang, C. Xiao, C. Yang, M. Chen, S. A. Yang, J. Hu, Z. Ren, H. Pan, W. Zhu, Z.-A. Xu, and Y. Lu, *Ferroelectric Control of Single-Molecule Magnetism in 2D Limit*, Sci. Bull. **65**, 1252–1259 (2020).

[111] C. Hua, H. Bai, Y. Zheng, Z.-A. Xu, S. A. Yang, Y. Lu, and S.-H. Wei, *Strong Coupled Magnetic and Electric Ordering in Monolayer of Metal Thio(seleno)phosphates*, Chinese Phys. Lett. **38**, 077501 (2021).

[112] H. Bai, X. Wang, W. Wu, P. He, Z. Xu, S. A. Yang, and Y. Lu, *Nonvolatile Ferroelectric Control of Topological States in Two-Dimensional Heterostructures*, Phys. Rev. B **102**, 235403 (2020).

[113] S. Curtarolo, W. Setyawan, G. L. W. Hart, M. Jahnatek, R. V. Chepulskii, R. H. Taylor, S. Wang, J. Xue, K. Yang, O. Levy, M. Mehl, H. T. Stokes, D. O. Demchenko, and D. Morgan, *AFLOW: An Automatic Framework for High-Throughput Materials Discovery*, Comput. Mater. Sci. **58**, 218–226 (2012).

[114] G. Kresse and D. Joubert, *From Ultrasoft Pseudopotentials to the Projector Augmented-Wave Method*, Phys. Rev. B **59**, 1758–1775 (1999).

[115] J. P. Perdew, K. Burke, and M. Ernzerhof, *Generalized Gradient Approximation Made Simple*, Phys. Rev. Lett. **77**, 3865 (1996).

[116] M. Boiocchi, F. Caucia, M. Merli, D. Prella, and L. Ungaretti, *Crystal-Chemical Reasons for the Immiscibility of Periclase and Wustite Under Lithospheric P, T Conditions*, Eur. J. Mineral. **13**, 871–881 (2001).

[117] S. Curtarolo, W. Setyawan, S. Wang, J. Xue, K. Yang, R. H. Taylor, L. J. Nelson, G. L. W. Hart, S. Sanvito, M. B. Nardelli, N. Mingo, and O. Levy, *AFLOWLIB.ORG: A Distributed Materials Properties Repository from High-Throughput Ab Initio Calculations*, Comput. Mater. Sci. **58**, 227–235 (2012).

[118] F. Rose, C. Toher, E. Gossett, C. Oses, M. B. Nardelli, M. Fornari, and S. Curtarolo, *AFLUX: The LUX Materials Search API for the AFLOW Data Repositories*, Comput. Mater. Sci. **137**, 362–370 (2017).

[119] R. H. Taylor, F. Rose, C. Toher, O. Levy, K. Yang, M. B. Nardelli, and S. Curtarolo, *A RESTful API for Exchanging Materials Data in the AFLOWLIB. Org Consortium*, Comput. Mater. Sci. **93**, 178–192 (2014).

[120] R. Dunlap, S. Jha, H. Seyoum, G. Julian, R. Pappas, and J. Blue, *Hyperfine fields at sp sites in Cl_b Heusler alloys*, Hyperfine Interact. **16**, 689–692 (1983).

[121] K. Buschow and D. De Mooij, *Crystal structure and magnetic properties of PtMnGa and PtMnAl*, J. Less-Common Met. **99**, 125–130 (1984).

[122] K. Yang, S. Nazir, M. Behtash, and J. Cheng, *High-Throughput Design of Two-Dimensional Electron Gas Systems Based on Polar/Nonpolar Perovskite Oxide Heterostructures*, Sci. Rep. **6**, 1–9 (2016).

[123] K. Buschow and P. Van Engen, *Magnetic and Magneto-Optical Properties of Heusler Alloys Based on Aluminium and Gallium*, J. Magn. Magn. Mater. **25**, 90–96 (1981).

[124] K. v. Buschow, P. Van Engen, and R. Jongebreur, *Magneto-Optical Properties of Metallic Ferromagnetic Materials*, J. Magn. Magn. Mater. **38**, 1–22 (1983).

[125] H. Masumoto, K. Watanabe, and S. Ohnuma, *Cl_b-Type Intermetallic Compound in the Ir–Mn–Sb System and Its Magnetic Properties*, Trans. Jpn. Inst. Met. **19**, 63–68 (1978).

[126] J. M. D. Coey and S. Sanvito, *Magnetic Semiconductors and Half-Metals*, J. Phys. D: Appl. Phys. **37**, 988–993 (2004).

[127] M. Julliere, *Tunneling Between Ferromagnetic Films*, Phys. Lett. A **54**, 225–226 (1975).

[128] Y. Takamura, T. Suzuki, Y. Fujino, and S. Nakagawa, *Full-Heusler Co_2FeSi Alloy Thin Films with Perpendicular Magnetic Anisotropy Induced by MgO-Interfaces*, J. Appl. Phys. **115**, 17C732 (2014).

[129] Y. Takamura, Y. Stutler, E. Matsushita, K. Shinohara, T. Suzuki, and S. Nakagawa, *Perpendicular Magnetic Anisotropy in Full-Heusler Co_2FeSi Alloy and MgO Bilayers*, J. Magn. Soc. Jpn. **43**, 120–124 (2019).

[130] K. H. J. Buschow, J. H. N. van Vucht, P. G. van Engen, D. B. de Mooij, and A. M. van der Kraan, *Structure, Magnetic and Magneto-Optical Properties, and ^{57}Fe Mössbauer Effect in a New Variety of Heusler Alloy: PtFeSb*, Phys. Stat. Sol. (a) **75**, 617–623 (1983).

[131] J. Ma, Y. Xie, K. Munira, A. W. Ghosh, and W. H. Butler, *Computational Investigation of Half-Heusler/MgO Magnetic Tunnel Junctions with (001) Orientation*, J. Appl. Phys. **129**, 223907 (2021).

[132] Y. Huai, *Spin-Transfer Torque MRAM (STT-MRAM): Challenges and Prospects*, AAPPS bulletin **18**, 33–40 (2008).

[133] A. Khvalkovskiy, D. Apalkov, S. Watts, R. Chepulskii, R. Beach, A. Ong, X. Tang, A. Driskill-Smith, W. Butler, P. Visscher, et al., *Basic Principles of STT-MRAM Cell Operation in Memory Arrays*, J. Phys. D: Appl. Phys. **46**, 074001 (2013).

[134] A. Moser, K. Takano, D. T. Margulies, M. Albrecht, Y. Sonobe, Y. Ikeda, S. Sun, and E. E. Fullerton, *Magnetic Recording: Advancing Into the Future*, J. Phys. D: Appl. Phys. **35**, R157 (2002).

[135] S. Yuasa, T. Nagahama, A. Fukushima, Y. Suzuki, and K. Ando, *Giant Room-Temperature Magnetoresistance in Single-Crystal Fe/MgO/Fe Magnetic Tunnel Junctions*, Nat. Mater. **3**, 868 (2004).

[136] S. Peng, D. Zhu, J. Zhou, B. Zhang, A. Cao, M. Wang, W. Cai, K. Cao, and W. Zhao, *Modulation of Heavy Metal/Ferromagnetic Metal Interface for High-Performance Spintronic Devices*, Adv. Electron. Mater. p. 1900134 (2019).

[137] M. Gabor, T. Petrisor Jr, C. Tiusan, M. Hehn, and T. Petrisor, *Magnetic and Structural Anisotropies of Co_2FeAl Heusler Alloy Epitaxial Thin Films*, Phys. Rev. B **84**, 134413 (2011).

[138] W. Wang, E. Liu, M. Kodzuka, H. Sukegawa, M. Wojcik, E. Jedryka, G. Wu, K. Inomata, S. Mitani, and K. Hono, *Coherent Tunneling and Giant Tunneling Magnetoresistance in $Co_2FeAl/MgO/CoFe$ Magnetic Tunneling Junctions*, Phys. Rev. B **81**, 140402 (2010).

[139] X. Li, S. Yin, Y. Liu, D. Zhang, X. Xu, J. Miao, and Y. Jiang, *Perpendicular Magnetic Anisotropy of Full-Heusler Films in Pt/Co_2FeAl/MgO Trilayers*, Appl. Phys. Express **4**, 043006 (2011).

[140] M. Belmeguenai, H. Tuzcuoglu, M. S. Gabor, T. Petrisor, C. Tiusan, D. Berling, F. Zighem, T. Chauveau, S. M. Chérif, and P. Moch, *Co_2FeAl Thin Films Grown on MgO Substrates: Correlation Between Static, Dynamic, and Structural Properties*, Phys. Rev. B **87**, 184431 (2013).

[141] J. Okabayashi, H. Sukegawa, Z. Wen, K. Inomata, and S. Mitani, *Large Anisotropic Fe Orbital Moments in Perpendicularly Magnetized Co_2FeAl Heusler Alloy Thin Films Revealed by Angular-Dependent X-Ray Magnetic Circular Dichroism*, Appl. Phys. Lett. **103**, 102402 (2013).

[142] Z. Wen, J. P. Hadorn, J. Okabayashi, H. Sukegawa, T. Ohkubo, K. Inomata, S. Mitani, and K. Hono, *Interdiffusion in Epitaxial Ultrathin Co_2FeAl/MgO Heterostructures with Interface-Induced Perpendicular Magnetic Anisotropy*, Appl. Phys. Express **10**, 013003 (2017).

[143] Z. Bai, L. Shen, Y. Cai, Q. Wu, M. Zeng, G. Han, and Y. P. Feng, *Magnetocrystalline Anisotropy and Its Electric-Field-Assisted Switching of Heusler-Compound-Based Perpendicular Magnetic Tunnel Junctions*, New J. Phys. **16**, 103033 (2014).

[144] M. S. Gabor, T. Petrisor, C. Tiusan, and T. Petrisor, *Perpendicular Magnetic Anisotropy in Ta/Co_2FeAl/MgO Multilayers*, J. Appl. Phys. **114**, 063905 (2013).

[145] G. Kresse and J. Furthmüller, *Efficiency of Ab-Initio Total Energy Calculations for Metals and Semiconductors Using a Plane-Wave Basis Set*, Comput. Mater. Sci. **6**, 15–50 (1996).

[146] G. Kresse and J. Furthmüller, *Efficient Iterative Schemes for Ab Initio Total-Energy Calculations Using a Plane-Wave Basis Set*, Phys. Rev. B **54**, 11169–11186 (1996).

[147] J. P. Perdew, K. Burke, and M. Ernzerhof, *Generalized Gradient Approximation Made Simple*, Phys. Rev. Lett. **77**, 3865–3868 (1996).

[148] P. E. Blöchl, O. Jepsen, and O. K. Andersen, *Improved Tetrahedron Method for Brillouin-Zone Integrations*, Phys. Rev. B **49**, 16223 (1994).

[149] S. Steiner, S. Khmelevskyi, M. Marsmann, and G. Kresse, *Calculation of the Magnetic Anisotropy with Projected-Augmented-Wave Methodology and the Case Study of Disordered $Fe_{1-x}Co_x$ Alloys*, Phys. Rev. B **93**, 224425 (2016).

[150] K. Masuda and Y. Miura, *Perpendicular Magnetic Anisotropy at the $Fe/MgAl_2O_4$ Interface: Comparative First-Principles Study with Fe/MgO*, Phys. Rev. B **98**, 224421 (2018).

[151] S. Kwon, Q. Sun, F. Mahfouzi, K. L. Wang, P. K. Amiri, and N. Kioussis, *Voltage-Controlled Magnetic Anisotropy in Heterostructures with Atomically Thin Heavy Metals*, Phys. Rev. A **12**, 044075 (2019).

[152] S. Lakshmanan, M. R. Muthuvel, P. Delhibabu, and H. Annal Therese, *Robust Perpendicular Magnetic Anisotropy in $MgO/Co_2FeAl/MgO$ Stacks Induced by MgO Over Layer and Annealing Temperature*, Phys. Status Solidi A **215**, 1800316 (2018).

[153] H. Sukegawa, Z. Wen, S. Kasai, K. Inomata, and S. Mitani, *Spin Transfer Torque Switching and Perpendicular Magnetic Anisotropy in Full Heusler Alloy Co_2FeAl-Based Tunnel Junctions*, Spin **4**, 1440023 (2014).

[154] D.-s. Wang, R. Wu, and A. J. Freeman, *First-Principles Theory of Surface Magnetocrystalline Anisotropy and the Diatomic-Pair Model*, Phys. Rev. B **47**, 14932 (1993).

[155] K. Nakamura, T. Akiyama, T. Ito, M. Weinert, and A. J. Freeman, *Role of an Interfacial FeO Layer in the Electric-Field-Driven Switching of Magnetocrystalline Anisotropy at the Fe/MgO Interface*, Phys. Rev. B **81**, 220409 (2010).

[156] S. Kwon, P.-V. Ong, Q. Sun, F. Mahfouzi, X. Li, K. L. Wang, Y. Kato, H. Yoda, P. K. Amiri, and N. Kioussis, *Colossal Electric Field Control of Magnetic Anisotropy at Ferromagnetic Interfaces Induced by Iridium Overlayer*, Phys. Rev. B **99**, 064434 (2019).

[157] K. Masuda, S. Kasai, Y. Miura, and K. Hono, *Giant Interfacial Perpendicular Magnetic Anisotropy in $Fe/CuIn_{1-x}Ga_xSe_2$ Beyond Fe/MgO*, Phys. Rev. B **96**, 174401 (2017).

[158] X. Chen, S. Zhang, B. Liu, F. Hu, B. Shen, and J. Sun, *Theoretical Investigation of Magnetic Anisotropy at the $La_{0.5}Sr_{0.5}MnO_3/LaCoO_{2.5}$ Interface*, Phys. Rev. B **100**, 144413 (2019).

[159] G. Daalderop, P. Kelly, and M. Schuurmans, *First-Principles Calculation of the Magnetocrystalline Anisotropy Energy of Iron, Cobalt, and Nickel*, Phys. Rev. B **41**, 11919 (1990).

[160] S. Nazir, M. Behtash, and K. Yang, *Towards Enhancing Two-Dimensional Electron Gas Quantum Confinement Effects in Perovskite Oxide Heterostructures*, J. Appl. Phys. **117**, 115305 (2015).

[161] W. Tang, E. Sanville, and G. Henkelman, *A Grid-Based Bader Analysis Algorithm Without Lattice Bias*, J. Phys.: Condens. Matter **21**, 084204 (2009).

[162] Y. Iida, Q. Xiang, J. Okabayashi, T. Scheike, H. Sukegawa, and S. Mitani, *Effect of Tungsten Doping on Perpendicular Magnetic Anisotropy and Its Voltage Effect in Single Crystal Fe/MgO (001) Interfaces*, J. Phys. D: Appl. Phys. **53**, 124001 (2019).

[163] J.-H. Kim, J.-B. Lee, G.-G. An, S.-M. Yang, W.-S. Chung, H.-S. Park, and J.-P. Hong, *Ultrathin W Space Layer-Enabled Thermal Stability Enhancement in A Perpendicular MgO/CoFeB/W/CoFeB/MgO Recording Frame*, Sci. Rep. **5**, 16903 (2015).

[164] K. Y. Camsari, B. M. Sutton, and S. Datta, *P-Bits for Probabilistic Spin Logic*, Appl. Phys. Rev. **6**, 011305 (2019).

[165] P. F. Carcia, A. D. Meinhaldt, and A. Suna, *Perpendicular Magnetic Anisotropy in Pd/Co Thin Film Layered Structures*, Appl. Phys. Lett. **47**, 178–180 (1985).

[166] K. Hyomi, A. Murayama, J. Eickmann, and C. M. Falco, *Perpendicular Magnetic Anisotropy in Au/Co/Au(111) Films: Interface Anisotropy and Effect of Strain*, J. Magn. Magn. Mater. **198-199**, 378–380 (1999).

[167] Y. C. Won and S. H. Lim, *Perpendicular magnetic anisotropy of a Ta/NiFeB/MgO system and its magnetic coupling with [Pt/Co] multilayers*, J. Alloys Compound. **858**, 157678 (2021).

[168] H. Zhang, *High-Throughput Design of Magnetic Materials*, Electron. Struct. (2020).

[169] K. Özdoğan, E. Şaşıoğlu, and I. Galanakis, *Slater-Pauling Behavior in LiMgPdSn-type Multifunctional Quaternary Heusler Materials: Half-Metallicity, Spin-Gapless and Magnetic Semiconductors*, J. Appl. Phys. **113**, 193903 (2013).

[170] J. E. Saal, S. Kirklin, M. Aykol, B. Meredig, and C. Wolverton, *Materials Design and Discovery with High-Throughput Density Functional Theory: The Open Quantum Materials Database (OQMD)*, JOM **65**, 1501–1509 (2013).

[171] J. Cheng and K. Yang, *Design of two-dimensional electron gas systems via polarization discontinuity from large-scale first-principles calculations*, Journal of Materials Chemistry C **6**, 6680–6690 (2018).

[172] V. Alijani, S. Ouardi, G. H. Fecher, J. Winterlik, S. S. Naghavi, X. Kozina, G. Stryganyuk, C. Felser, E. Ikenaga, Y. Yamashita, et al., *Electronic, structural, and magnetic properties of the half-metallic ferromagnetic quaternary Heusler compounds CoFeMn Z (Z= Al, Ga, Si, Ge)*, Phys. Rev. B **84**, 224416 (2011).

[173] L. Bainsla and K. Suresh, *Equiatomic quaternary Heusler alloys: A material perspective for spintronic applications*, Appl. Phys. Rev. **3**, 031101 (2016).

[174] D. Rani, K. Suresh, A. Yadav, S. Jha, D. Bhattacharyya, M. R. Varma, A. Alam, et al., *Structural, electronic, magnetic, and transport properties of the equiatomic quaternary Heusler alloy CoRhMnGe: Theory and experiment*, Phys. Rev. B **96**, 184404 (2017).

[175] Y. Venkateswara, S. Gupta, M. R. Varma, P. Singh, K. Suresh, A. Alam, et al., *Electronic structure, magnetism, and antisite disorder in CoFeCrGe and CoMnCrAl quaternary Heusler alloys*, Phys. Rev. B **92**, 224413 (2015).

[176] F. F. Abdi, L. Han, A. H. M. Smets, M. Zeman, B. Dam, and R. van de Krol, *Efficient Solar Water Splitting by Enhanced Charge Separation in a Bismuth Vanadate-Silicon Tandem Photoelectrode*, Nat. Commun. **4:2195** (2013).

[177] T. Odaira, X. Xu, A. Miyake, T. Omori, M. Tokunaga, and R. Kainuma, *Thermal, magnetic field-and stress-induced transformation in Heusler-type Co-Cr-Al-Si shape memory alloys*, Scripta Mater. **153**, 35–39 (2018).

[178] G.-H. Yu, Y.-L. Xu, Z.-H. Liu, H.-M. Qiu, Z.-Y. Zhu, X.-P. Huang, and L.-Q. Pan, *Recent progress in Heusler-type magnetic shape memory alloys*, Rare Met. **34**, 527–539 (2015).

[179] Y. Han, M. Wu, Y. Feng, Z. Cheng, T. Lin, T. Yang, R. Khenata, and X. Wang, *Competition between cubic and tetragonal phases in all-d-metal Heusler alloys, X2- xMn1+ xV (X= Pd, Ni, Pt, Ag, Au, Ir, Co; x= 1, 0): a new potential direction of the Heusler family*, IUCrJ **6**, 465–472 (2019).

[180] D. Johnson, K. Suresh, A. Alam, et al., *Half-metallic Co-based quaternary Heusler alloys for spintronics: Defect-and pressure-induced transitions and properties*, Phys. Rev. B **94**, 184102 (2016).

[181] P. Klaer, B. Balke, V. Alijani, J. Winterlik, G. Fecher, C. Felser, and H. Elmers, *Element-specific magnetic moments and spin-resolved density of states in CoFeMn Z (Z= Al, Ga; Si, Ge)*, Phys. Rev. B **84**, 144413 (2011).

[182] B. Balke, S. Wurmehl, G. H. Fecher, C. Felser, and J. Kübler, *Rational design of new materials for spintronics: Co2FeZ (Z= Al, Ga, Si, Ge)*, Sci. Technol. Adv. Mater. (2008).

[183] J. Nehra, V. D. Sudheesh, N. Lakshmi, and K. Venugopalan, *Structural, Electronic and Magnetic Properties of Quaternary Half-Metallic Heusler Alloy CoFeCrAl*, Phys. Status Solidi RRL **7**, 289–292 (2013).

[184] L. Bainsla, A. Mallick, A. Coelho, A. Nigam, B. C. S. Varaprasad, Y. Takahashi, A. Alam, K. Suresh, and K. Hono, *High spin polarization and spin splitting in equiatomic quaternary CoFeCrAl Heusler alloy*, J. Mater. Chem. C **394**, 82–86 (2015).

[185] M. Halder, M. Mukadam, K. Suresh, and S. Yusuf, *Electronic, structural, and magnetic properties of the quaternary Heusler alloy NiCoMnZ (Z= Al, Ge, and Sn)*, J. Magn. Magn. Mater. **377**, 220–225 (2015).

[186] L. Bainsla, A. I. Mallick, M. M. Raja, A. A. Coelho, A. K. Nigam, D. D. Johnson, A. Alam, and K. G. Suresh, *Origin of Spin Gapless Semiconductor Behavior in CoFeCrGa: Theory and Experiment*, Phys. Rev. B **92**, 045201 (2015).

[187] L. Bainsla, K. Suresh, A. Nigam, M. Manivel Raja, B. C. S. Varaprasad, Y. Takahashi, and K. Hono, *High spin polarization in CoFeMnGe equiatomic quaternary Heusler alloy*, J. Appl. Phys. **116**, 203902 (2014).

[188] L. Bainsla, A. I. Mallick, M. M. Raja, A. K. Nigam, B. S. D. C. S. Varaprasad, Y. K. Takahashi, A. Alam, K. G. Suresh, and K. Hono, *Spin Gapless Semiconducting Behavior in Equiatomic Quaternary CoFeMnSi Heusler Alloy*, Phys. Rev. B **91**, 104408 (2015).

[189] S. P. Ong, W. D. Richards, A. Jain, G. Hautier, M. Kocher, S. Cholia, D. Gunter, V. L. Chevrier, K. A. Persson, and G. Ceder, *Python Materials Genomics (pymatgen): A Robust, Open-Source Python Library for Materials Analysis*, Comput. Mater. Sci. **68**, 314–319 (2013).

[190] W. Wang, H. Sukegawa, R. Shan, S. Mitani, and K. Inomata, *Giant Tunneling Magnetoresistance up to 330% at Room Temperature in Sputter Deposited Co_2FeAl/MgO/CoFe Magnetic Tunnel Junctions*, Appl. Phys. Lett. **95**, 182502 (2009).

[191] S. Yuasa, T. Nagahama, A. Fukushima, Y. Suzuki, and K. Ando, *Giant Room-Temperature Magnetoresistance in Single-Crystal Fe/MgO/Fe Magnetic Tunnel Junctions*, Nat. Mater. **3**, 868–871 (2004).

[192] J. Pan, J. Ni, and B. Yang, *Surface Structures of $Co_2FeAl_{0.5}Si_{0.5}$ (001) Heusler Alloys: A First-Principles Study*, Phys. B (Amsterdam, Neth.) **405**, 1580–1585 (2010).

[193] I. Galanakis, *Effect of Surfaces and Interfaces on the Electronic, Magnetic and Gap-Related Properties of the Half-Metal Co_2MnSn*, J. Comput. Theor. Nanosci. **7**, 474–478 (2010).

[194] I. Galanakis, *Surface Properties of the Half-and full-Heusler Alloys*, J. Phys.: Condens. Matter **14**, 6329 (2002).

[195] S. J. Hashemifar, P. Kratzer, and M. Scheffler, *Preserving the Half-Metallicity at the Heusler Alloy Co_2MnSi(001) Surface: A Density Functional Theory Study*, Phys. Rev. Lett. **94**, 096402 (2005).

[196] E. P. George, D. Raabe, and R. O. Ritchie, *High-Entropy Alloys*, Nat. Rev. Mater. **4**, 515–534 (2019).

[197] C. Oses, C. Toher, and S. Curtarolo, *High-Entropy Ceramics*, Nat. Rev. Mater. pp. 1–15 (2020).

[198] A. Karati, M. Nagini, S. Ghosh, R. Shabadi, K. Pradeep, R. C. Mallik, B. Murty, and U. Varadaraju, *Ti_2NiCoSnSb-A New Half-Heusler Type High-Entropy Alloy Showing Simultaneous Increase in Seebeck Coefficient and Electrical Conductivity for Thermoelectric Applications*, Sci. Rep. **9**, 1–12 (2019).

[199] S. Anand, M. Wood, Y. Xia, C. Wolverton, and G. J. Snyder, *Double Half-Heuslers*, Joule **3**, 1226–1238 (2019).